



# **Upgrading and characterization of a magnetically-coupled piston pump for ultra-clean noble gas applications**

Master thesis

Denny Schulte

Westfälische Wilhelms- Universität Münster

Institut für Kernphysik

AG Prof. Dr. C. Weinheimer

2018

Referent: Prof. Dr. C. Weinheimer

Korreferent: Prof. Dr. A. Khoukaz



# Declaration of Academic Integrity

I hereby confirm that this thesis on  
**Upgrading and characterization of a magnetically-coupled piston pump for  
ultra-clean noble gas applications**

is solely my own work and that I have used no sources or aids other than the ones  
stated. All passages in my thesis for which other sources, including electronic media,  
have been used, be it direct quotes or content references, have been acknowledged as  
such and the sources cited.

I agree to have my thesis checked in order to rule out potential similarities with other  
works and to have my thesis stored in a database for this purpose.

---

*date*

*signature*



# Contents

<b>1. Noble gases</b>	<b>3</b>
1.1. Properties . . . . .	3
1.2. Principle of a time projection chamber and applications . . . . .	16
<b>2. Purification of noble gases and required special pumps</b>	<b>23</b>
2.1. Signal attenuation by impurities . . . . .	23
2.2. Purification methods . . . . .	26
2.3. Pumps for ultra-clean noble gas experiments . . . . .	27
2.4. Pumps of the XENON1T experiment . . . . .	28
2.5. The EXO-200 pump . . . . .	30
<b>3. The Muenster magnetically-coupled piston pump</b>	<b>33</b>
3.1. General layout . . . . .	33
3.2. Increasing force by upgrading of the external magnetic ring . . . . .	38
3.3. Flapper valves . . . . .	44
3.4. Piston gaskets . . . . .	47
3.5. Cooling system . . . . .	55
3.6. Linear drive . . . . .	57
3.7. Thermodynamic model . . . . .	63
<b>4. Performance and long-term stability</b>	<b>69</b>
4.1. Highest coupling pressure . . . . .	72
4.2. Thermodynamic characterization . . . . .	73
4.3. Heat evolution measurement . . . . .	78
4.4. Drive profile . . . . .	80
4.5. Performance . . . . .	85
4.6. Long-term stability . . . . .	87
4.7. Radon emanation . . . . .	88
<b>5. Installation at XENON1T</b>	<b>91</b>
<b>6. Conclusion</b>	<b>95</b>

<b>7. Outlook</b>	<b>99</b>
<b>A. Appendix</b>	<b>103</b>
<b>B. Bibliography</b>	<b>109</b>

## Introduction

In order to get wise of today's most intriguing questions of physics, radiation detectors with extremely pure noble gases as detection medium are a promising technology. Noble gases feature unique properties in terms of inertness and the response to an interaction with incident particles.

Often, the detectors based on noble gas targets are filled with a liquid phase or with a liquid and gaseous phase of the noble gas to make use of the ionization and scintillation character of the detector medium. A usual realization is a Time Projection Chamber (TPC).

The extensive field of application of this technology ranges from dark matter search, neutrino physics and scintillation calorimeters to Compton telescopes and medical imaging, since the interaction of incident particles and the inert creates charges, light and heat.

However, in order to prevent losses of the produced charge and light yields, the target material has to be ultra-clean. Electronegative impurities capture the electrons of the ionization and absorb the scintillation light. Therefore, these impurities have to be removed from the noble gas.

For this purpose, the inert gas has to be continuously recirculated through a purification system by pumps. Commercially available diaphragm and bellows pumps cannot fulfill essential requirements in terms of absolute containment of the gas in case of a failure and extremely cleanliness of all hermetically sealed components, which are often required to be completely oil-free and radio-pure.

Therefore, a new pump based on a magnetically-coupled piston design has been developed in Muenster in cooperation with the nEXO group at Stanford University and the nEXO/XENON group at Rensselaer Polytechnic Institute.

The magnetically-coupled piston ensures a complete isolation of the gas, since the drive mechanism is outside of the hermetically sealed pump. Moreover, only ultra-clean components, such as stainless steel, copper, aluminum and advanced polymers guarantee no oil-based lubrication as well as high radio-purity. An enhanced magnetic gradient by a sophisticated magnet arrangement additionally results in a coupling strength of the piston of  $(3468 \pm 25) \text{ N}$ .

The high coupling forces thereby leads to high performances of the pump in the form of flow and compression.

For a long time, it seems to be impossible to manage the heat evolution and achieve a long stable and high performance. This thesis shows the progress of the last year, which results in a stable operation and an improvement of the performance.

Initially, the first chapter presents the unique characteristics of noble gases, which provide the use as detector target material. Additionally, a handful of applications with a detection medium based on a noble gas is given, followed by the required purification.

Chapter two gives a brief presentation of pumps for ultra-clean noble gas applications. An example for currently used pumps and the EXO-200 pump, the trailblazer of this pump, is shown. The third chapter introduces the magnetically-coupled piston pump of this thesis. This main chapter focuses on the redesign of several parts to achieve a stable and high performance.

Afterwards, the performance and stability at the Muenster pump test station is shown followed by the important radon emanation measurement, which provides the required absolute cleanliness in terms of radio-purity.

The end of this thesis is devoted to an implementation to a running system, which zooms in on the XENON1T purification system.

Finally, a conclusion will sum up and an outlook presents further usage of a modified pump based on this pump.



# 1. Noble gases

Even Sir William Ramsay, discoverer of the noble gases<sup>1</sup>, recognized the great capability of his pioneering serendipity at the end of the 19th century. The unique properties of these inert gases provided the basis to the understanding of the electronic structure and the binding character in atoms. Furthermore, due to their special characteristics noble gases are used in a wide range of research as well as industry. The research field varies from neutrino physics, calorimeters and Compton telescopes to nuclear medicine, dark matter search and more. A few typical industry applications of noble gases are the usage as protective gases, cryogenic refrigerants, balloon gases and gas-discharge lamps. In the following, noble gases are referred to as helium, neon, argon, krypton, xenon and radon and not to the synthetic transactinides organesson.

This chapter presents the properties of the different noble gases followed by a fistful of associated applications. In the end of this chapter, the essential purification of the noble gases for utilizing as detector media will be shown.

## 1.1. Properties

The six colorless and odorless gases helium, neon, argon, krypton, xenon and radon are at the 18. group of the periodic table. Each of the gases of this group is monoatomic and non-toxic and distinguishes itself by a low chemical reactivity. This low chemical reactivity occurs from their outer electronic shell, which is totally occupied. In contrast to elements with non-fully occupied electronic shells, noble gases will not catch electrons by itself as well as feature the highest ionization energies of all elements in the periodic table, which is shown in figure 1.1.

Helium possesses the largest ionization potential with 24.6 eV [CRC03] followed by neon, argon and the larger noble gases. Usually, the atomic radius increases within a group of the periodic table such as from helium to radon. Since a higher atomic radius corresponds to a larger distance between the electron in the outermost shell and the attractive coulomb potential of the nucleus, the ionization potential is decreased. Another important effect is that the electrons between nucleus and outermost shell lead to a shielding of the nucleus potential. Therefore, the higher the number of electrons

---

<sup>1</sup>Actually Sir William Ramsay discovered only helium, neon, argon krypton and xenon.

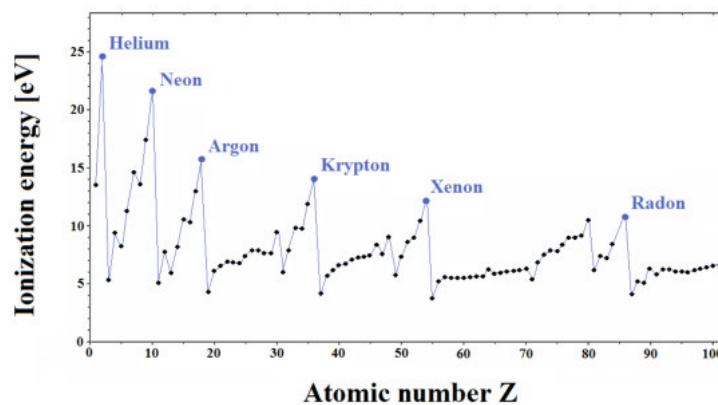


Figure 1.1.: Ionization potential versus atomic number  $Z$  of the elements from the periodic table. The inert gases feature the highest ionization energy for each period. Data points from [Mar96].

in between, the lower the ionization energy, which explains exactly what is presented in figure 1.1. The high ionization potentials of the noble gases are responsible for a unique inertness.

Intermolecular forces are extremely weak. Only London dispersion forces, a weak attraction between nonpolar atoms and molecules, exist, which arise from spontaneous polarization of particles creating quantum-induced multipoles. This results in low boiling points. Since the dispersion forces depend on the size of the particle, helium contains the lowest boiling point followed by neon, argon and so on. Table 1.1 shows the boiling points and the melting points at standard conditions as well as the related natural abundance of the inert gases in air.

Gas	Boiling point [K]	Melting point [K]	Abundance in air [%]
Helium	4.2	—	0.00052
Neon	27.2	24.6	0.0018
Argon	87.2	83.8	0.93
Krypton	121.2	115.8	0.0001
Xenon	165.2	161.4	0.000008
Radon	211.3	202.0	$6 \cdot 10^{-18}$
Nitrogen	77.2	63.1	78.09
Oxygen	90.2	54.8	20.95
Carbondioxide	194.7	—	0.03
Hydrogen	20.3	14.0	0.000005

Table 1.1.: Boiling points, melting points and abundance of gases in the air at standard conditions [Pay17, CRC03].

Noble gases contain an extreme short range between boiling and melting point compared to other elements, which results in a small range of the liquid phase.

All noble gases can be found in the air. The dominant abundant gases in air are nitrogen with 78.09 % and oxygen with 20.95 %. Argon contains with 0.93 % the biggest part of noble gases in the air. The other inert gases are distinctly less abundant, which results in a costly fabrication.

The noble gases are mostly obtained from the air by cryogenic distillation, which is based on the *Linde-Verfahren* [Lin17a]. The *Linde-Verfahren* uses the Joule Thomson effect to liquefy air. This effect describes the cool down of a real gas at adiabatic, isenthalpic expansion. The temperature decrease is created by a reduction of the kinetic energy to overcome the intramolecular attraction forces.

Figure 1.2 presents the basic principle of the *Linde-Verfahren*.

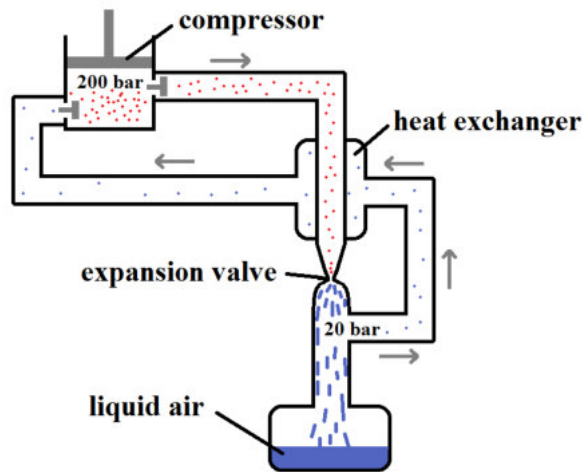


Figure 1.2.: *Linde-Verfahren*: The Joule Thomson effect is used to decrease the temperature by expansion. Countercurrent heat exchange results in required low temperatures to liquefy air.

In order to liquefy air, the gas will be compressed to 200 bar and will be expanded through an expansion valve to for example 20 bar, which results in a temperature decrease. Countercurrent heat exchange is used to reach stepwise lower temperatures: The expanded gas is extracted again for precooling of the compressed gas. The successive temperature decrease leads to the liquefaction of the air at about 80 K [Czi91].

For the separation of the gases within the liquid air the difference in boiling points is used (table 1.1). This way, fractional separation of the constituents is possible.

In industrial realizations the fractional separation is done by rectification in large distillation columns with several condensation floors (fig. 1.3).

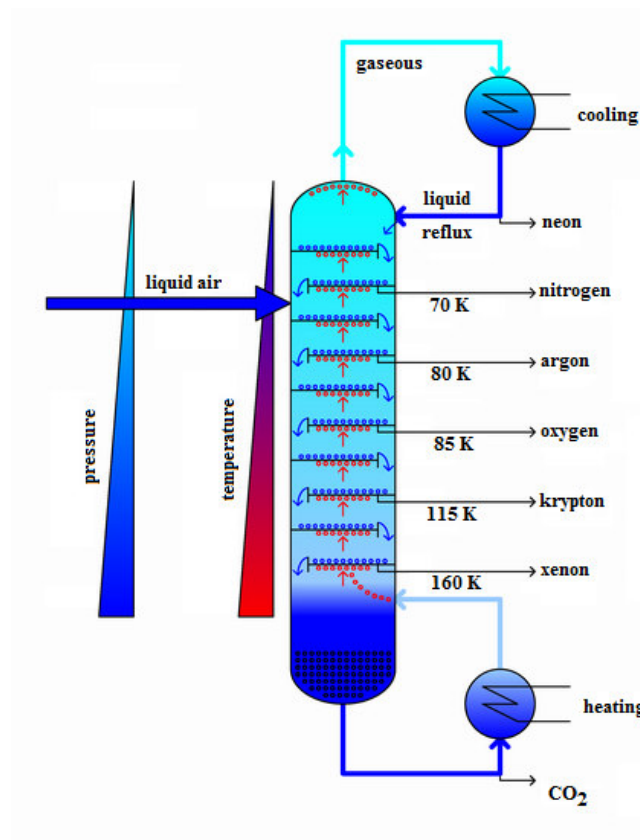


Figure 1.3.: Simplified principle of air separation by fractional distillation. The difference in boiling points is used to achieve higher concentrations of certain gases at certain points inside the column. Basic structure from [Doc08].

Basically, such construction consists of a reboiler at the bottom, a condenser at the top and in between a long column with several stages. By heating at the reboiler and cooling at the condenser a temperature and pressure gradient is created, which results in enriched concentrations of certain gases at certain stages. For example at the top, an enriched neon mixture can be extracted. Of course, this mixture also contains helium, hydrogen and less concentration of the other gases, but they can be further separated in following columns and adsorption mechanisms. That way, the gases can piecemeal be separated up to adequate gas purity for industry applications. However, for a few years helium is usually extracted from natural gas due to its higher abundance. Since each noble gas has its own amenity, the related attributes will be described separately in the following. All specifications about boiling-/ melting points and densities have been used from [CRC03]. For data of isotopes [Lie01] has been used.

## Helium

Helium has a proton number of two, so it is the lightest noble gas. Boiling point and melting point are extremely deep. Helium is the only element which will not solidify at absolute zero for normal pressure. The boiling point is at 4.2 K and the melting point with 25 bar at 0.95 K. At such low temperatures, helium has superfluid properties. Figure 1.4 shows the phase diagram of helium.

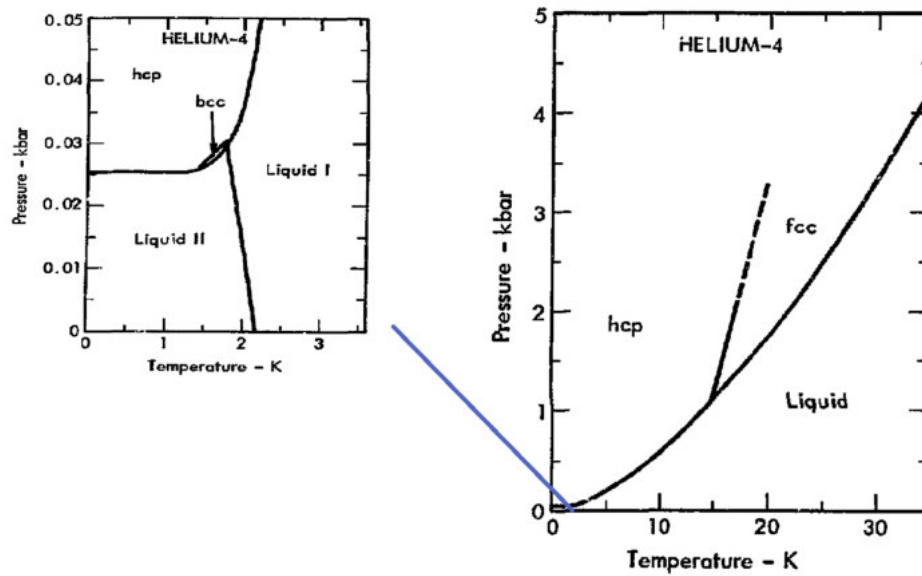


Figure 1.4.: Phase diagram of helium [Tou75].

The normal liquid (Liquid I) has a phase transition to the superfluid liquid (Liquid II). Superfluids feature an infinitesimal viscosity. They therefore approximately flow without kinetic energy losses. Helium solidifies both hexagonal close-packed (hcp), body-centered cubic (bcc) and face-centered cubic (fcc) dependent on temperature and pressure. However, the bcc range is very small.

Gaseous helium shows exceeding high specific capacity as well as the highest thermal conductivity after hydrogen. Moreover after hydrogen, helium is the second most abundant element in the universe. Eight isotopes of helium have been discovered, whereof only the  $^3\text{He}$  and  $^4\text{He}$  are stable.

Helium is mainly used as cooling gas, balloon gas and welding gas to keep oxygen away. Furthermore, it is used as leak-detection gas for vacuum systems and supports the excitation and relaxation at lasers such as at the helium-neon laser.

## Neon

Neon is after helium the lightest inert with an atomic number of 10. The following figure presents its phase diagram.

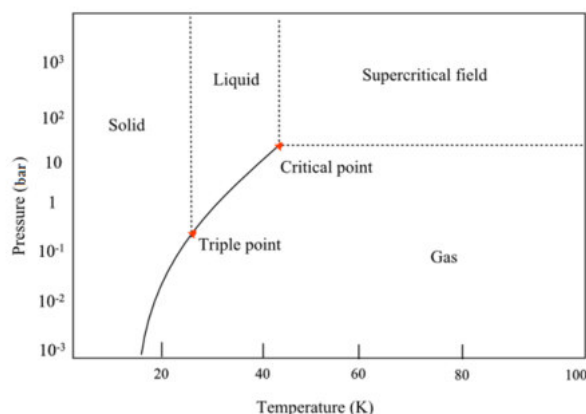


Figure 1.5.: Phase diagram of neon [Niv15].

Neon's boiling point is 27.2 K, and it melts at 24.6 K at normal pressure. Therefore, the temperature range of the liquid phase is the shortest of the elements in the periodic table. The density of the liquid at boiling point and normal pressure is  $1207 \text{ kg/m}^3$ . The density of gaseous neon is comparatively small with  $0.9 \text{ kg/m}^3$  at standard conditions compared to other noble gases except for helium. The triple point is at a temperature of 24.6 K at 0.43 bar. At temperatures of more than 44.5 K with pressures higher than 27.7 bar (critical point) neon is a supercritical fluid. Neon solidifies by fcc symmetry.

According to current calculations of the dissociation enthalpy, neon seems to be the least chemical reactive element of all [Lew08].

The number of known isotopes is 18 including three stable isotopes,  $^{20}\text{Ne}$ ,  $^{21}\text{Ne}$  and  $^{22}\text{Ne}$ . The isotope  $^{20}\text{Ne}$  is the most frequent isotope with more than 90 %. It is one of the most abundant elements in the universe since it is a common product of carbon fusion. However, on earth neon is very rare and mostly exists in the atmosphere, because it is lighter than nitrogen as well as lighter than oxygen. Due to the rareness on earth, the fabrication is expensive compared to the similar argon. The most prevalent use is the laser industry and the lightening engineering, since neon has the most intense light discharge of all noble gases. Furthermore, neon is interesting for research in particle- and astrophysics, due to the fact that it can be easily purified, which will be explained in detail in section 1.2. Additionally, no long-life radioactive isotopes exist, which makes neon attractive as detector medium for low background physics.

## Argon

Argon has an atomic number of 18. Figure 1.6 presents the phase diagram: The boiling point is with 87.2 K much higher than the boiling point of neon, similar to the solidifying at a temperature of 84.1 K (standard pressure). It solidifies in a fcc structure. The triple point (T) is at a pressure of 0.69 bar and a temperature of 83.7 K. The critical point of argon is at a pressure of 48.9 bar with a temperature of 150.8 K.

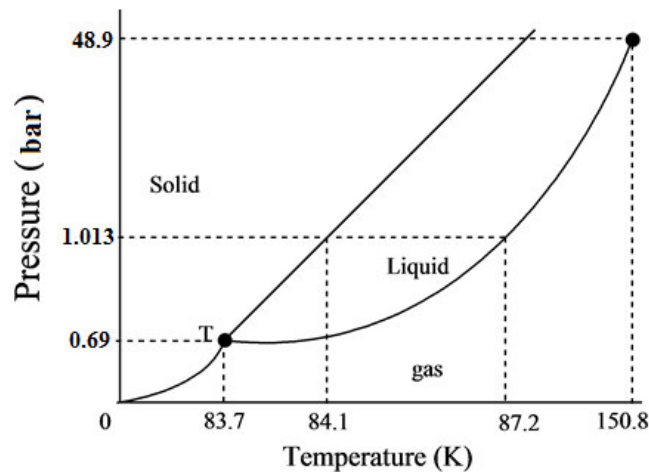


Figure 1.6.: Phase diagram of argon [Niv15].

Moreover, the gas has a density of  $1.784 \text{ kg/m}^3$ . The liquid at boiling point has a density of  $1393 \text{ kg/m}^3$ . Thus, it is more dense than neon which results in an inherent high stopping power for ionizing particle.

Argon is the third most common element in the universe. Today, 23 isotopes are discovered, whereof three isotopes are stable. The earth is rife with  $^{40}\text{Ar}$ . 99.6 % of the Argon on earth is  $^{40}\text{Ar}$ . Except for  $^{39}\text{Ar}$  and  $^{42}\text{Ar}$ , all radioactive isotopes feature negligible half-lives.

Low production costs and a high amount of this unique element makes it interesting for many applications such as protective gas for welding and steelmaking, fire extinguishing media or lightening gas. Furthermore, argons inertness combined with high availability and its high stopping power makes it very attractive as target material for calorimeters and scintillation detectors in particle physics and astroparticle physics.

## Krypton

Krypton is with an atomic number of 36 one of the heavier noble gases. Figure 1.7 shows the phase diagram, where one pound-force per square inch (psi) is around 0.069 bar. At standard conditions, it is gaseous similar to all other inert gases. At standard pressure the gas condenses at a temperature of 121.2 K and freezes at 115.8 K. The crystal structure as well is cubic face-centered.

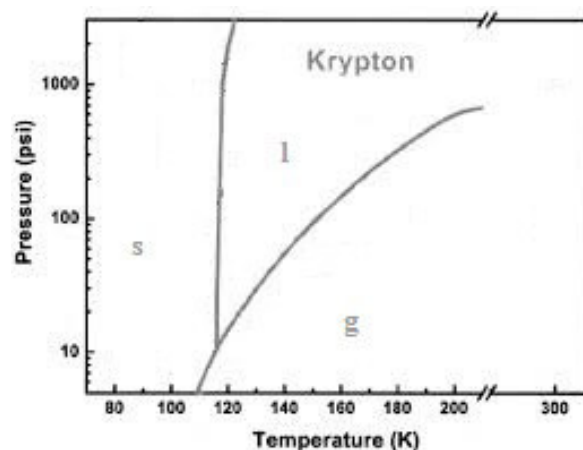


Figure 1.7.: Phase diagram of krypton [Key18].

Furthermore, krypton gas has a density of  $3.75 \text{ kg/m}^3$ . The liquid features a density of  $2413 \text{ kg/m}^3$ . Therefore it features, similar to argon, a high stopping power for penetration radiation.

Krypton is one of the most rare elements on earth. The biggest part can be found in the atmosphere with a concentration of  $1.14 \text{ ppm}^2$  [Wil16].

The existence of 31 isomers and 10 nuclear isomers is known. Five of them are stable,  $^{80}\text{Kr}$ ,  $^{82}\text{Kr}$ ,  $^{83}\text{Kr}$ ,  $^{84}\text{Kr}$  and  $^{86}\text{Kr}$ . The biggest part of the isotopic krypton mixture in the air is represented with 57 % by  $^{84}\text{Kr}$  following by  $^{86}\text{Kr}$  with more than 17 % and  $^{83}\text{Kr}$  and  $^{82}\text{Kr}$  with both more than 11 %. Additionally, several long-lived unstable isotopes can be found naturally in air. Beside  $^{78}\text{Kr}$  and  $^{81}\text{Kr}$ , the radioactive isotope  $^{85}\text{Kr}$  with a half-life of 10.756 years is measurable. It is created by nuclear fission of uranium and plutonium. Therefore, nuclear bombs and reconditioning of nuclear fuel rods released the krypton in the air. The application area of krypton varies from laser technology and lightening engineering to scintillation and Geiger counters. Moreover, krypton is used in particle physics as detection material for calorimeters, which will be shown in section 1.2.

<sup>2</sup>Parts per million,  $1 \text{ ppm} = 1 \cdot 10^{-6} \text{ mol/mol}$



## Xenon

Xenon has a proton number of 54. Thus, it is the heaviest stable noble gas. Figure 1.8 presents the related phase diagram. Xenon's boiling point with 165.2 K at standard pressure is, just as the melting point at 161.4 K, even higher than of Krypton. The triple point (t.p.) is at a temperature of 161.45 with a pressure of 0.82 bar. The critical point (c.p.) at 289.7 K and 58.4 bar.

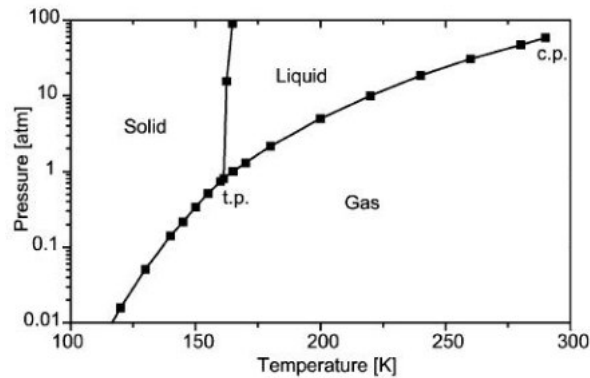


Figure 1.8.: Phase diagram of xenon [Che03].

In addition, gaseous xenon with a density of  $5.90 \text{ kg/m}^3$  and liquid xenon with a density of  $2942 \text{ kg/m}^3$  are considerably more dense than all stable noble gases, which leads to the highest stopping power of incoming particles.

However, the electronic shells are fully occupied such as at all noble gases, xenon is next to radon the most reactive noble gas, due to a low ionization energy of the valence electrons of 12.13 eV for the first electron (cp. figure 1.1).

Xenon is the rarest stable element on earth. It consists of 37 isotopes and 12 nuclear isomers. Seven isotopes are stable. Additionally, two unstable long-life isotopes contribute to the natural abundant xenon. Industrially available xenon is composed of 26.9 %  $^{132}\text{Xe}$ , 26.4 %  $^{129}\text{Xe}$ , 21.2 %  $^{131}\text{Xe}$ , 10.4 %  $^{134}\text{Xe}$  and 8.9 % *unstable*<sup>3</sup>  $^{136}\text{Xe}$ .

Due to xenon's rareness on earth, it is very expensive. Primarily, it is used in the lightening engineering, since the discharge emits light similar to daylight. Furthermore, xenon's scintillation light yields are comparable to those of NaI(Tl), but the shorter decay time of xenon leads to a higher energy resolution. For this reason, scintillation applications with xenon as detection medium are promising. Therefore usages in medical sector, particle- and astrophysics are widely spread.

<sup>3</sup>The isotope  $^{136}\text{Xe}$  features a half-life of  $2.11 \cdot 10^{21}$  years

## Radon

Radon features an atomic number of 86 and is radioactive. The boiling point with  $211.3^{\circ}\text{C}$  and the melting point with  $202.0^{\circ}\text{C}$  are high compared to other noble gases. Radon possesses a high density of  $9.73\text{ kg/m}^3$ .

Its low ionization potential of  $10.7\text{ eV}$  in contrast to other noble gases results in several chemical compounds, primarily with fluorine.

Radon is originated by the decay chains of actinium, radium and thorium. The abundance in air (cp. table 1.1) is created by the equilibrium between continuous emanation from rocks and soil and the half-lives of radon's isotopes. Only three natural isotopes,  $^{222}\text{Rn}$ ,  $^{220}\text{Rn}$  and  $^{219}\text{Rn}$ , are relevant. The isotope  $^{222}\text{Rn}$  is with 90 % of the radon most abundant and contains the longest half-life of 3.8 days, which is long enough to diffuse in the air and groundwater. The half-lives of the other isotopes are comparatively small (4 s and 56 s). Figure 1.9 shows a simplified decay chain of the  $^{222}\text{Rn}$ .

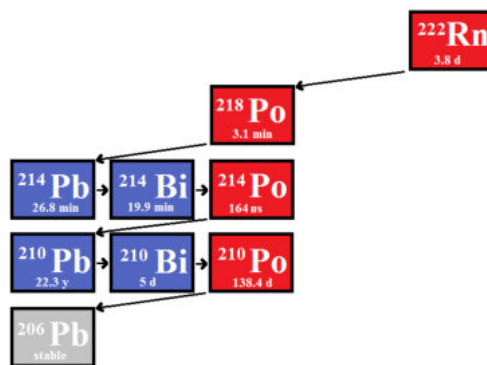


Figure 1.9.: Decay chain of  $^{220}\text{Rn}$ . Subdominant decays have been omitted. The half-life times have been taken from [Lie01].

The decay chain contains  $\alpha$ -emitters (red) and  $\beta$ -emitters (blue) and ends in the stable  $^{206}\text{Pb}$  (grey). The half-lives of the daughters ranges from  $164\mu\text{s}$  for  $^{214}\text{Po}$  to  $22.3\text{ y}$  for the isotope  $^{210}\text{Pb}$ .

Formerly, radon was useful in cancer therapy due to the polonium daughters with its alpha particles. The alpha-radiation has a high energy of more than  $5\text{ MeV}$ . Because of their large mass and charge  $\alpha$ -particles are easily absorbed by matter. Moreover for low background experiments, radon is used as a calibration source, since the half-life of 3.8 days is long enough to distribute homogenously over large-scaled detectors. Due to its natural radioactivity radon cannot be used as target material. The usage of the other noble gases as detection medium is presented in the next section.

## Noble gases as detector material

As mentioned above, noble gases such as helium, neon, argon, krypton and xenon are promising as detector material in research, for example at particle physics, space exploration and medical imaging. This arises from their special properties such as the unique inertness. Besides, another key feature is their characteristic excitation and ionization process in response to incident radiation, which creates scintillation photons, charge carriers as well as heat [Mei08].

If an incoming particle  $\chi$  interacts inside a detector filled with the noble gas  $Ng$  (He, Ne, Ar, Kr, Xe), the inert will be excited and ionized. At the excitation, the excited inert forms an excited dimer with other atoms of the detector material (eq. 1.2). Afterwards, the excited dimer relaxes and produces a direct vuv scintillation light  $h\nu$  (eq. 1.3) [Bec02]:



Additionally, the ionization process also creates next to electrons excited dimers to a certain extent due to recombination (eq. 1.4, 1.5), which produce direct scintillation light  $h\nu$  at relaxation (eq. 1.9). In addition, this process produces heat as well (eq. 1.7) [Bec02]:



This way, three channels to detect energy deposit of the interaction is approachable. The energy deposit of an elastic scatter is specific for the incident particle sort.

Furthermore, particle discrimination can be done by the kind of interaction. At mid and high atomic mass nuclei, radiation such as  $\beta$  and  $\gamma$  as rather scatter due to their low mass with the electronic shell than with the nucleus by photoelectric absorption,

Compton scattering and pair production, which is called electronic recoil (ER). Neutrons and  $\alpha$ -particles interact by a nuclear recoil (NR), where a higher recombination of the electrons results in less charges.

Often, the energy deposit of penetrating particles is low (keV or a few MeV) which makes it difficult to measure the heat. Since the temperature increase  $\Delta T$ , which will be generated by an energy deposit  $\Delta E$  in an absorber, is basically calculated by

$$\Delta T = \frac{\Delta E}{C}, \quad (1.10)$$

with the heat capacity  $C$  of the absorber. In order to measure such temperature increase,  $C$  has to be as low as possible. In dielectric absorbers collective phonon modes are dominating, which results for low temperatures according to Debye in

$$C \propto \left( \frac{T}{\Theta_D} \right)^3, \quad (1.11)$$

where  $\Theta_D$  is the Debye temperature. However in metals, a linear relationship occurs due to the conduction electrons. Therefore, temperatures in the range of mK are suitable to make use of this effect and gain a measurable temperature increase for superconducting thermometers.

However, it is possible to reach such low temperatures in crystals, we will focus on the detection observables light and charges in the following, since the applications with noble gases as detection medium are widely-spread. Compared to crystals, noble gas targets are large-scaleable, which is suitable for low background experiments, since boundary effects can be neglected.

Usually, in order to measure the response of incident radiation in terms of the scintillation light, the noble gas based target material is liquid, since the liquid density is higher than the gaseous. Intuitively, the interaction probability depends on the density of the target material. Moreover, a high density results in a larger collision rate of the excimers with further atoms to create the excited dimers before relaxation occurs (eq. 1.2 and eq. 1.8). Therefore, high scintillation yields between 19000 (LHe) and 42000 photons/MeV (LXe) are possible in contrast to organic scintillators with yields up to 10000 photons/MeV [Apr06]. Concerning detection of this scintillation lights, noble gas detectors are usually equipped with photomultiplier tubes (PMTs). Figure 1.10 presents scintillation spectra of the noble gases helium, neon, argon, krypton and xenon.

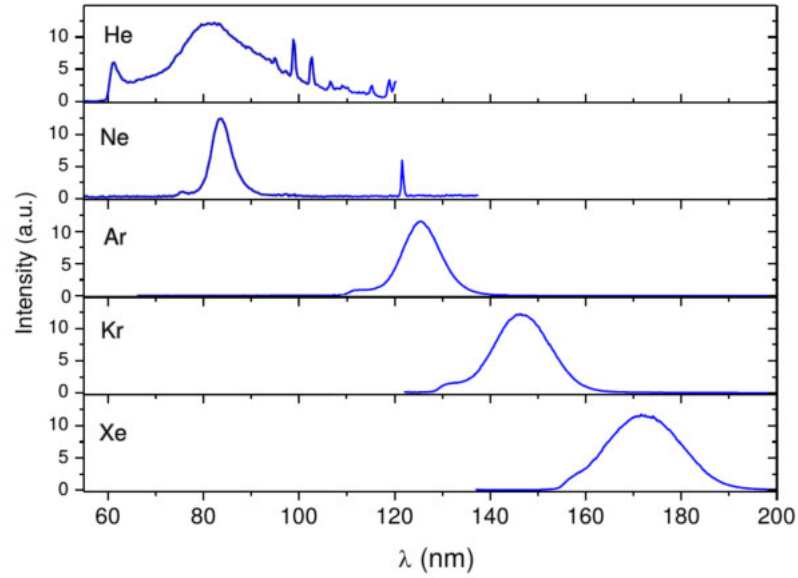


Figure 1.10.: Scintillation spectra for He, Ne, Ar, Kr and Xe [Neu15]. The lighter noble gases helium and neon emit mostly scintillation light below 90 nm. Therefore, wavelength shifters are required to detect the light with PMTs. The 121 nm peak in the neon spectrum is the Lyman-alpha line of the residual impurity hydrogen.

The spectra show, noble gases emit scintillation light in the vacuum ultraviolet region ( $< 200$  nm). Therefore, primarily for the lighter gases wavelength shifters are required, because no transparent window materials for PMTs is available to detect light below 90 nm [Neu15].

Commonly, in order to measure the charges of the ionization created in the liquid at an interaction, a small gaseous phase of the noble gas is used. The charges will be drifted and extracted into the gaseous phase to deposit energy, which is proportional to the produced charges of the initial interaction.

The next section will give a realization of such detector in the form of a dual-phase time projection chamber, which makes use of the unique noble gas properties by detection of charges and light in case of an interaction within the noble gas target.

## 1.2. Principle of a time projection chamber and applications

A promising technique to make use of the excitation and ionization character of a noble gas as detector material is a dual-phase Time Projection Chamber (TPC) (Fig. 1.11). In the following, a dual-phase TPC will be presented in detail using the example of the XENON1T experiment, since this promising experiment will be considered a few times in this thesis.

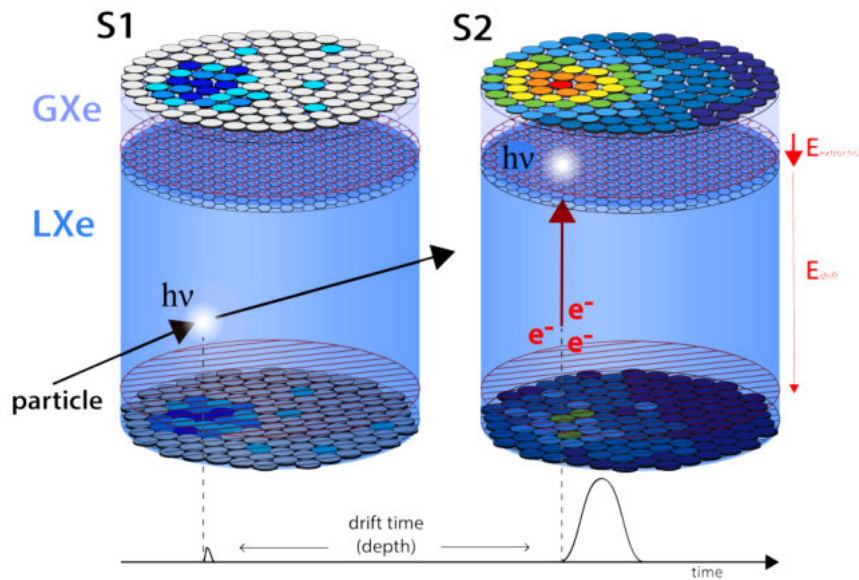


Figure 1.11.: Dual-phase Time Projection Chamber. Figure by Lutz Althueser.

The usual cylindrical detector volume consists of a liquid phase of the noble gas, in this case xenon, combined with a small gaseous phase above. In order to achieve maximum reflection inside the detector for highest scintillation light collection, the inner volume is surrounded by polytetrafluorethylen (PTFE). PTFE is not only highly suitable due to the good efficiency to reflect scintillation light, but also because it can be fabricated with high purity in terms of radioactive emanation.

Additionally, in order to keep the xenon liquid, the detector is cooled all the time to temperatures around 170 K at about 2 bar and therefore housed in a vacuum chamber, the cryostat, to avoid thermal losses.

The direct scintillation light called S1, which results from the excitation by the scattering process of incident radiation with xenon nuclei, can be detected by PMT arrays at the top and bottom of the detector.

Additionally, the electrons of the ionization (eq.1.4) will be accelerated by a predefined, homogeneous electro-magnetic field  $E_{drift}$  to the grounded gate mesh at the top

of the liquid phase and will be extracted into the gaseous phase by another electric field  $E_{\text{extraction}}$ . The interaction with xenon atoms in the gaseous phase leads to an energy deposit and thus another scintillation light, the S2. Furthermore, the time between these two signals can be used to determine the z-position of interaction due to the predefined drift field. Additionally, the photomultiplier tube array at the top can determine the x- and y-position of the interaction, due to the small gaseous phase. In such a way, a three dimensional position reconstruction of the interaction point inside the detector can be accomplished.

This position reconstruction of the interaction events is of crucial importance for separation of background events, since only events in a predefined center volume are shielded from background by the noble gas. Moreover, the existence of both signals, the S1 and the S2, provides discrimination between NR and ER at the interaction. The ratio of S1 and S2 is different for ER and NR such that its an indication for the particle sort.

Thus, the dual-phase TPC can make use of the unique characteristics of the inert gases. In the following, the dark matter search with the XENON experiment will be explained, which uses such dual-phase TPC.

### The XENON experiment

Decades of research were required to reach the present-day scientific findings about the composition of the universe.

For example, besides the ordinary baryonic matter, which only accounts for about 4% of the whole universe energy-density, a non-baryonic matter, the dark matter, and the widely unknown dark energy form the universe. Albeit the knowledge about dark energy is restricted, the progress of the dark matter research is promising.

One budding particle candidate for this dark matter is the Weakly Interacting Massive Particle (WIMP), since it satisfies all attributes such as being stable, non-electromagnetic, massive as well as non-relativistic, non-baryonic and at last having a cross-section on the scale of the weak interaction. As an example, the XENON Dark Matter Project located at the Laboratori Nazionali del Gran Sasso (LNGS) in Italy at a depth of about 3600m water equivalence is geared to search for such WIMPs by direct detection. For this purpose, a dual-phase TPC shown in figure 1.11 of pure xenon is used to detect interactions of WIMPs with xenon atoms.



Figure 1.12.: The XENON1T Experiment underground. *Left*: the water tank with a poster showing the inside. *Right*: the three-story service building [XEN18].

Xenon features a further advantage by its large atomic mass  $A$ , since for spin independent WIMP-nucleus scattering the cross-section  $\sigma_{SI}$  can be expressed by

$$\sigma_{SI} \propto A^2 \quad (1.12)$$

The current detector generation XENON1T uses 3.3 tons of extremely pure xenon and obtains with  $7.7 \cdot 10^{-47} \text{cm}^2$  the most stringent exclusion limit for a spin-independent scattering of a  $35 \text{ GeV}/c^2$  WIMP with a xenon nucleus in the world [Apr17b]. The key feature to achieve such high sensitivity is the purification of the noble gas.

Another important low background experiment, which uses a TPC, is the Enriched Xenon Observatory (EXO) experiment. EXO presented in the following searches for the neutrinoless double beta decay, to ascertain the properties of the neutrino.

## The EXO experiment

One of the biggest breakthroughs of last decades was the evidence of the neutrino. Many characteristics of the neutrino are still open.

The observation of a neutrinoless double beta decay ( $0\nu\beta\beta$ ) would evidence the majorana fermion, which means that the neutrino is its own antiparticle. This also would violate the conservation of the lepton number and allows measuring the neutrino-mass by the half-life of the decay.

Double-beta decays ( $2\nu\beta\beta$ ) (fig. 1.13) occur when a single-beta decay is energetically or due to the Pauli-principle forbidden. Then, two neutrons in the unstable nucleus become



to protons by emission of two electrons and two antineutrinos. Meanwhile, the special decay has been observed for many isotopes featuring a long half-life of about  $10^{20}$  years. A neutrinoless decay, where only electrons are emitted, is theoretically predicted for the majorana neutrino with non-zero mass, which is already proven by neutrino oscillation.

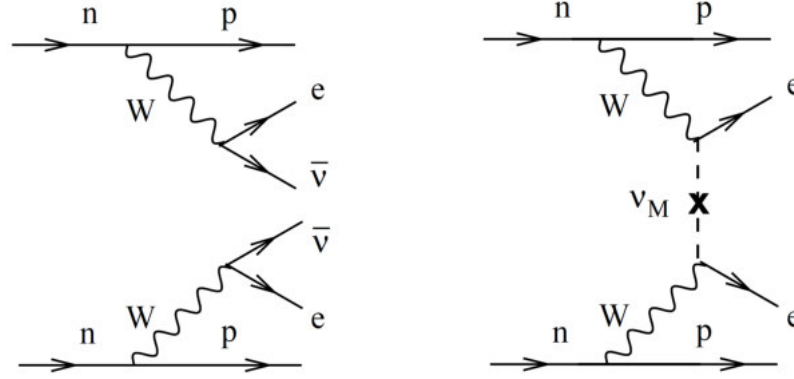


Figure 1.13.: Feynman diagram for the  $2\nu\beta\beta$  (left) and the  $0\nu\beta\beta$  decay (right) [Avi07].

The EXO experiment located at Waste Isolation Pilot Plant (WIPP) in the United States uses a single-phase liquid xenon TPC with 200 kg target material (fig. 1.14). At a single-phase TPC the charges can be collected by wires instead of PMTs. The xenon is highly enriched with the unstable isotope  $^{136}\text{Xe}$ . The Q-value of the isotope  $^{136}\text{Xe}$  for the interaction is  $(2457.83 \pm 0.37)$  keV and thus higher than most of the background especially the gamma lines from the uranium chain [Bar12].

With this detector, the most stringent limit on the rate of the  $0\nu\beta\beta$  has been achieved. The key feature of this experiment is also the reduction of background by primarily a high purity of the target material.

Further experiments based on different noble gases as detection medium, which require an extremely high purity of their target material will be shortly presented in the following.

### Further applications using gas purification of noble gases

Another neutrino physics and dark matter application is the MiniCLEAN/CLEAN experiment (Cryogenic Low Energy Astrophysics with Noble gases) using a single-phase TPC filled with pure liquid argon or neon interchangeable. Thereby, examination of background and the  $A^2$  dependence of potential dark matter signals (see eq. 1.12) will be investigated [Rie15]. Moreover, compared to water detectors a high coherent cross-section and flavor blindness allow large yields for elastic neutrino nucleus scattering from supernovae [Coa03].

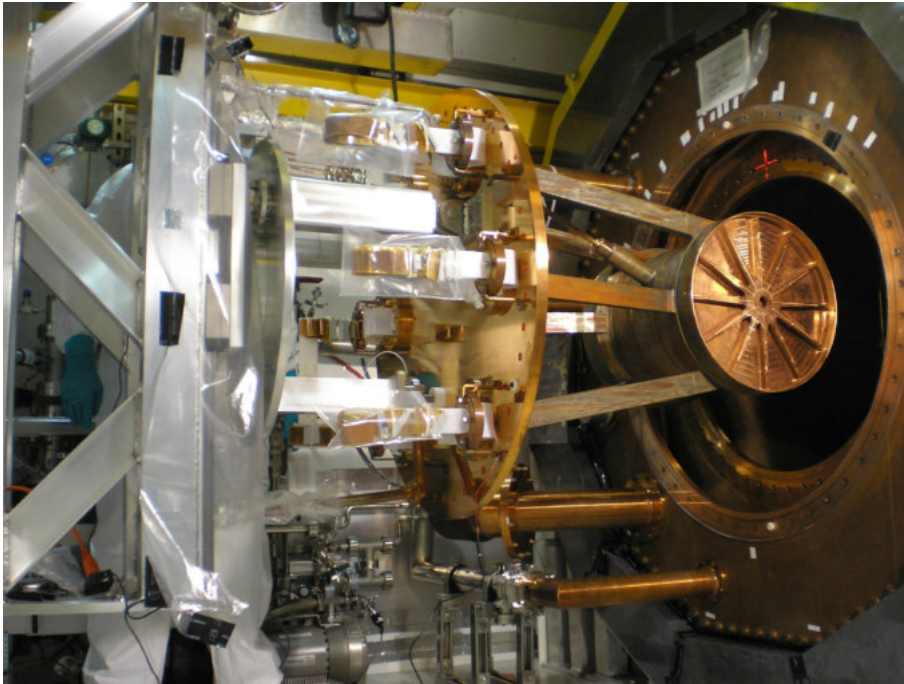


Figure 1.14.: The EXO-200 TPC being inserted into the cryostat [Aug12].

The MEG-experiment located at the Paul Scherrer Institut (PSI) in Switzerland searches for the charged decay of a muon,

$$\mu^+ \rightarrow e^+ + \gamma, \quad (1.13)$$

which violates the lepton flavor number.

In order to evidence this decay, the background has to be minimized. Therefore, a calorimeter filled with extremely pure xenon is used for  $\gamma$ -ray detection, which needs a high time, energy as well as position resolution to reduce background. For this purpose, the experiment uses gas as well as liquid xenon purification.

The experiment thereby achieved the most stringent limit on the existence of this decay with an upper limit of  $4.2 \cdot 10^{-13}$  [Iwa12].

A further interesting project is the NA62 experiment at the European nuclear research center CERN, which continues the NA48 experiment of the early 90's. It aims for measuring the direct CP violation by the rare decay of a kaon into a pion and two neutrinos

$$K^+ \rightarrow \pi^+ \nu \bar{\nu} \quad (1.14)$$

with high precision. The detector filled with nine liters of ultra-clean liquid krypton is used as a calorimeter. Nonetheless, also a gas purification is required, which is shown

in A.1. For more information, see [Mor09].

Furthermore, many applications in neurology, cardiology, oncology and pharmacology make use of the Positron Emission Tomography (PET) with the use of a pure xenon single-phase TPC [Che97, Xin08]. Gamma-ray telescopes also use noble gases in single-phase TPC's [Fro15]. Moreover, Pressurized pure helium-based targets are utilized in neutron detectors [Cha12, Bol03].

All these experiments make use of a gaseous purification system since the purity of the noble gases is not sufficient for the related application. Therefore, the next chapter will discuss the essential purification of noble gases in such experiments and the inevitable pumps required for the recirculation through a purification system.



## 2. Purification of noble gases and required special pumps

As mentioned in the last chapter, noble gases are used in many experiments as target medium to create charges and lights. In order to detect desired interactions and discriminate background, especially at experiments with rare expected events, the noble gas based detector material has to be extremely clean from electronegative impurities such as  $H_2$ ,  $O_2$ ,  $N_2$ ,  $CO/CO_2$ ,  $H_2O$  and hydrocarbons. In order to recirculate the noble gas through convenient purification systems, special pumps are required with a peculiar focus on the cleanliness of built-in components.

This chapter introduces attenuation effects of desired signals by impurities at the interaction of incident radiation with noble gas nuclei. Afterwards a detailed view to the purity of typical available noble gases from industry is given, which shows the abundance of key-impurities. The second section will present different purification methods and the last part of this chapter will focus on pumps required for the recirculation through such purification systems. At first, the claim for cleanliness of the built-in components will be motivated followed by examples of currently used pumps such as from the XENON1T experiment and from the EXO-200 experiment.

### 2.1. Signal attenuation by impurities

As shown for the dual-phase TPC (section 1.2), the capability for the position reconstruction as well as the signal discrimination depends on drifting the charges along the  $z$ -dimension of the detector and on detecting scintillation photons propagating through the liquid. Therefore, the attenuation of both, charges and light, is a contributing factor and will be explained in the following in detail.

#### Charge attenuation

As we have seen in section 1.1, recombination avoids for a fraction of charges to be captured from the electric drift field. Electrons, which escaped from recombination, drift with a characteristic mobility dependent on the noble gas through the target, where heavier noble gases feature higher electron mobility. This high mobility can be drastically

lowered by electronegative impurities such as  $\text{H}_2\text{O}$  and  $\text{O}_2$ , which can capture the free charges and form slow negative ions. The time free electrons can move before they are captured is called electron life time  $\tau_e$  and is inversely proportional to the impurity concentration [Fro15]:

$$\tau_e = \frac{1}{c_I \cdot a}, \quad (2.1)$$

where  $a$  is the attachment cross section, which depends on the electric field as well as the impurity sort. Therefore, the number of free electrons  $N(t)$  in a medium at a time  $t$ , which follows an exponential behaviour [Bak76], is given by

$$N(t) = N_0 \cdot e^{-t/\tau_e} = N_0 \cdot e^{-t \cdot a \cdot c_I},$$

with  $N_0$ , the number of free electrons at the time  $t = 0$ . Accordingly, the impurity concentration has to be lowered to a ppb level to reach sufficient charge yields [Che13].

### Light attenuation

In order to detect the photons of the scintillation process with the PMTs, a high reflectivity inside the detector is essential. Moreover, beside elastic Rayleigh scattering of photons, the absorption of photons has to be contributed. Since the noble gases are self-transparent for its own scintillation light, the absorption is mostly done by electronegative impurities. Figure 2.1 shows the photon absorption coefficient of  $\text{H}_2\text{O}$  and  $\text{O}_2$  in liquid xenon as an example and the xenon scintillation spectrum.

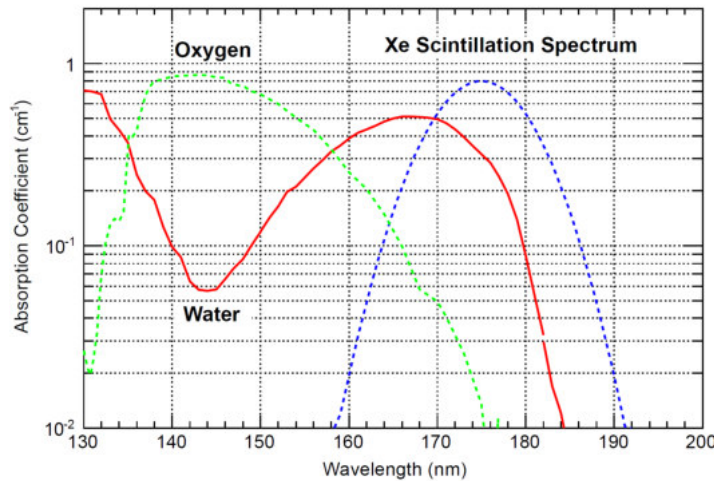


Figure 2.1.: Absorption coefficients for a impurity concentration of 1 ppm  $\text{H}_2\text{O}$  and  $\text{O}_2$  in liquid xenon [Che13].

Within a few centimeters, 1 ppm H<sub>2</sub>O in liquid xenon will absorb almost the whole scintillation light of the xenon.

Thus, in order to achieve high charges and light yields after interaction of a penetrated radiation particle with the noble gas, the noble gas has to be extremely pure from electronegative impurities.

## Impurities

Due to the fact that noble gases obtained from the air by cryogenic fractional distillation (section 1.1), they cannot be industrially fabricated with absolute purity. Usual purities of available bottled gases are 99.999 %. However, such purities still contain a few ppm of impurities.

Table 2.1 presents typical available bottled noble gases from industry with their constituents of impurities.

Table 2.1.: Bottled inerts from the industry [Lin17b].

	Helium	Neon	Argon	Krypton	Xenon
Purity [%]	99.999	99.999	99.999	99.999	99.999
Imp.[ppm]	8.2	10.1	10.7	10	10
He	-	5	-	-	-
Ne	-	-	-	-	-
Ar	-	-	-	1	1
Kr	-	-	-	-	1
Xe	-	-	-	1	-
H <sub>2</sub>	-	-	-	1	1
O <sub>2</sub>	2	1	2	0.5	0.5
N <sub>2</sub>	3	2	5	2	1
CO/CO <sub>2</sub>	-	-	0.5	1	1
H <sub>2</sub> O	3	2	3	2	2
CF <sub>4</sub> /C <sub>2</sub> F <sub>6</sub>	-	-	-	1	2
C <sub>n</sub> H <sub>n</sub>	0.2	0.1	0.2	0.5	0.5

The table shows that each noble gas contains electronegative impurities such as H<sub>2</sub>, O<sub>2</sub>, N<sub>2</sub>, CO/CO<sub>2</sub>, H<sub>2</sub>O and hydrocarbons with a ppm concentration. As mentioned above, an impurity concentration in ppb range is required for convenient charge yields produced by the ionization process of a noble gas. Additionally, according to figure 2.1, impurity concentrations in the range of ppm prevent for example in liquid xenon to achieve high light yields.

Therefore, purification of the noble gas is of crucial importance. In the following, several purification methods will be presented.

## 2.2. Purification methods

The purification of the gas can be done by two processes, physical adsorption or physisorption and chemical adsorption called chemisorption. At physisorption only weak van-der-Waals forces are used to adsorb atoms and molecules reversible, while chemisorption uses chemically bonds for adsorption. Therefore it is not reversible. Common purification techniques are molecular sieves, silica gels, hot metal getters, induced electron capture by electrical currents and spark purifiers.

### Molecular sieves

Molecular sieve materials such as zeolite are characterized by a high porosity and an open crystal lattice structure, which results in a large surface area of  $800 \text{ m}^2/\text{g}$  [Sma12]. With fixed cavity sizes between 200 pm and 2000 pm a selectivity for different adsorbers occurs [Sma12]. Since no compound formation takes place by physisorption on the surface of the porous absorber, the impurities can be reversibly outgassed at moderate temperatures in high vacuum.

As an example, a Hydrosorb uses a  $5 \text{ \AA}$  molecular sieve to physisorb  $\text{H}_2\text{O}$  and  $\text{CO}_2$  from smaller atoms and molecules to a maximum moisture concentration of 20 ppb [Mes17].

### Silica gels

Silica gels feature an amorphous structure and consist of similar porosity and surface area as molecular sieves. Their pore sizes are not fixed and range from 500 pm to 30 000 pm. A mean pore size of 2000 pm or 11 000 pm can be synthesized depending on the manufacturing process. [Gra10]

An application, which makes use of such silica gel, is the Oxisorb. The silica gel removes  $\text{H}_2\text{O}$  via physisorption to 30 ppb [Mes17]. Additionally, a supplement of chromium oxide chemically bounds and therefore abidingly removes oxygen to a final concentration of 5 ppb maximum [Mes17]. At this process, irreversible surface compounds are formed by chemical binding.

One problem of these cartridges for experiments with rare expected events is the high contamination by  $^{238}\text{U}$  creating the radioactive  $^{222}\text{Rn}$ , which results in a high background due to its daughters beta decays. Thus for low background experiments, an exceeding low level of radioactive impurities is of high importance, since the sensitivity is limited by the detector volume, which sets the rate of signals, and the background.



An alternative for such applications is the purification by hot metal getters.

### Hot metal getters

Certain hot metals getters can be used to collect gas impurities by adsorption and absorption. The binding process bases on both chemisorbtion as well as physisorbition. Depending on the carrier gas, the impurity sort, the impurity concentration and operation temperature, different metals or metal mixtures are convenient. [Sch15]

Popular elements are zirconium and barium. Barium is used with parts of other metals as a flash getter, where it is evaporated and bonds penetrating impurities. However, zirconium is used as a bulk getter. In contrast to other bulk getter materials such as tantalum, it contains moderate operation temperatures of 400 °C to 800 °C [Esp01].

SAES hot zirconium getters, for example, achieve impurity concentrations  $< 1$  ppb for  $O_2$ ,  $H_2O$ ,  $CO$ ,  $CO_2$ ,  $H_2$ ,  $N_2$  and  $CH_4$  [Sch15].

Moreover, another promising purification method is the spark discharge.

### Spark discharge

Spark purification uses titanium electrodes disintegrated by spark discharge. This way, much metal dust with large surface area is produced and absorbs electronegative impurities similar to a hot metal getter. Measurements in liquid xenon result in an electron lifetime increase by a factor of more than 500 [Esp01].

Usually, a combination of such purifiers is used to achieve a highest purification of the most dominant impurities shown in table 2.1.

For continuous recirculation of the noble gas through such purification system, pumps with extreme purity requirements such as oil-freeness, components cleanliness and low radioactive emanation are necessary. Additionally, due to larger and larger scaling of such experiments to achieve higher sensitivities, the pumps have to have a high performance.

## 2.3. Pumps for ultra-clean noble gas experiments

Today's low background experiments based on noble gas targets use pumps for a continuous recirculation through a purification system. Due to ever-expanding detector volumina, performance requirements are steadily rising. Furthermore, used pumps have to satisfy beside absence of oil-based lubrication special properties because of continuous warranty of absolute gas purity. Commercial bellows and diaphragms pumps cannot ensure this high performance as well as containment in the case of failure or a full control of all built-in components in terms of radio-purity.

### Cleanliness of the build-in components

For low background experiments with rare expected events, a careful material selection is essential to minimize background contributions. For instance, a contributing factor is radon, which permanently emanates from the used components into the noble gas.

As shown in chapter 1.1, the isotope  $^{220}\text{Rn}$  features a half-life of 56 s, which is not long enough for a homogenous distribution within the detector. Whereas, the half-life of the isotope  $^{222}\text{Rn}$  (3.8 days) is long enough to distribute all-over the detector medium.

Usually, the  $\alpha$ -emitters from the decay chain visualized in figure 1.9 are less annoying, since they can be identified easily by their comparatively high energies of more than 5 MeV. However, the  $\beta$ -emitters result in a high low-energy background. Furthermore, the  $\beta$ -decays produce positrons. These positrons can annihilate with drift electrons or locally change the potential for the drift electrons in the detector, which distort the detected signals.

In order to achieve high yields of the scintillation as well as ionization light of the noble gas in case of an interaction with an incident particle, this radon emanation has to be low for all components, which are directly in contact with the noble gas.

Therefore, pumps used for a recirculation of the detector material through a purification system have to be built of only clean and radio-pure components to feature a low radon emanation. In the following, as an example of currently used pumps, the QDrive pumps of the XENON1T experiment produced by the company Chart Inc will be presented. Subsequently, a detailed view to the EXO-200 pump is given.

## 2.4. Pumps of the XENON1T experiment

Currently used pumps operate not only close to their limit to fulfill present requirements in terms of performance, but also can not ensure the essential radio-purity.

For example at the XENON1T experiment, presented in section 1.2, several QDrive pumps (fig. 2.2) are needed to achieve a total gas flow of 50 slpm through the XENON1T purification system at an inlet pressure of 1.5 bar. A xenon flow of 50 slpm corresponds to a flux of 18 kg/hour. With a detector material inventory of about 3.3 tons xenon, a complete purification with 50 slpm would take eight days. Particularly with regard to future experiments, this can not be feasible.

The QDrive pumps are using a ferromagnetic piston inside a compression volume. The compression volume is again in another sealed volume, to ensure absolute gas containment. The piston is linearly moved by magnetic coils such that no lubricants are in contact with the pure gas. Therefore, the pumps are convenient for applications where cleanliness of the displaced gas is essential. The compression volume contains two reed

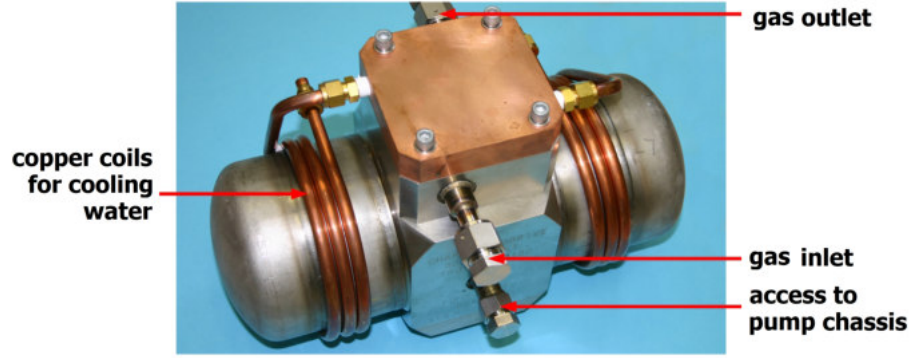


Figure 2.2.: QDrive pump of the company CHART. The piston pump uses magnetic resonance to compress gas without any oil lubrication. Picture from [Ros16].

valves, one for the inlet and one for the outlet, to achieve a positive gas displacement. Additionally, a total radon emanation for all three QDrive pumps of  $(10.9 \pm 1.7)$  mBq has been measured shown in figure 2.3, which amounts to 30.8 % of the total radon emanation of the detector and therefore limits the sensitivity of the project by the corresponding high background.

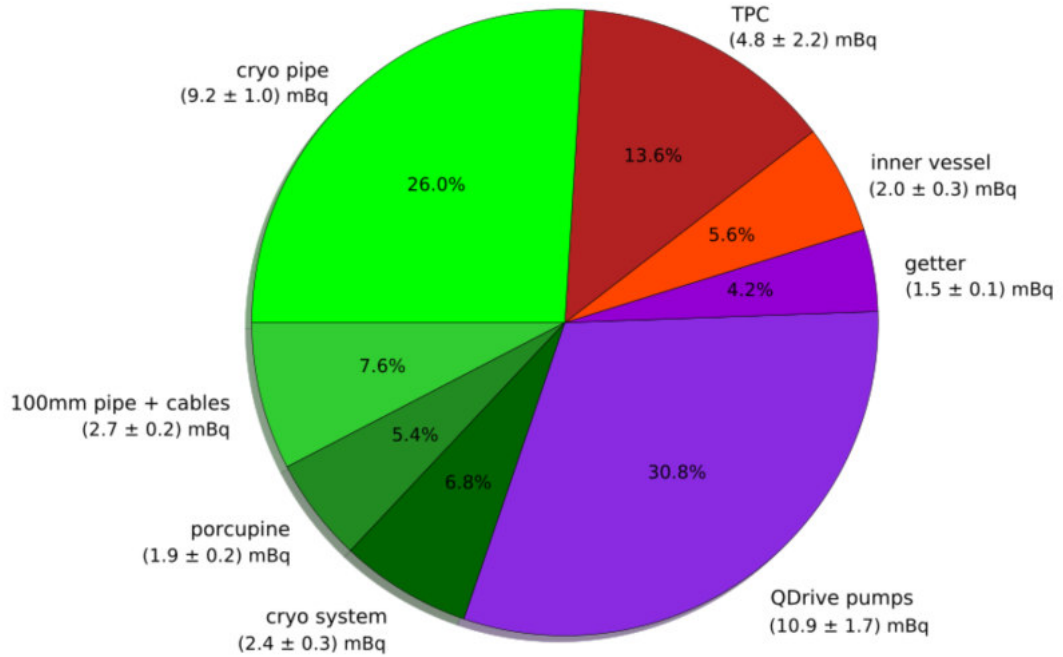


Figure 2.3.: Radon emanation of the XENON1T detector system [Bre17].

Thus, new pumps with similar gas containment attributes, similar drive mechanism

which is isolated from the gas, but with higher performance and lower radon emanation, are required. For example, the future stage of the XENON experiment, XENONnT, contains a xenon inventory of about eight tons of xenon. Therefore, flows of 200 slpm are desired. Additionally, since the radon emanation is the dominant background for this experiment [Apr16], it has to be lowered.

Further low-background experiments based on noble gases claim for similar specifications. Therefore, a new pump based on the EXO-200 pump, which can fulfill these requirements, has been developed in cooperation with the nEXO group Stanford and the nEXO/XENON group at Rensselaer Polytechnic Institute for ultra-clean noble gas applications. In the following, the EXO-200 pump will be presented.

## 2.5. The EXO-200 pump

The design of the EXO-200 pump is based on a horizontal tube with a hermetically sealed, magnetic piston inside (fig. 2.4). The piston is magnetically-coupled to an outer magnetic ring such that a movement of the outer permanent magnet by a motor drive leads to a movement of the coupled piston inside. This way, gas can be displaced in combination with a complete isolation of the drive mechanism from the gas.

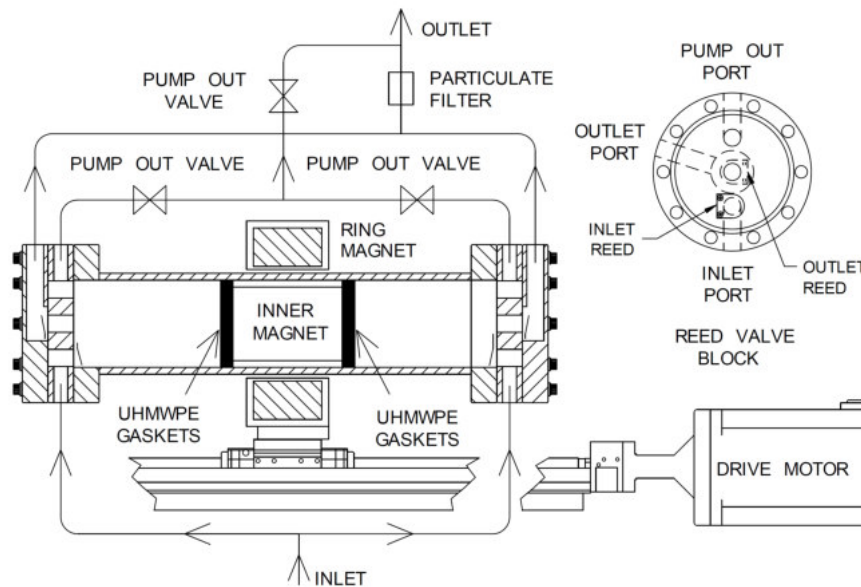


Figure 2.4.: EXO-200 pump - Due to the magnetically coupling of the piston to a magnetic ring completely outside the pump body, the drive mechanism is totally isolated from the gas. This way, no lubricants have to be used and the risk of gas contamination by drive failure can be eliminated. Drawing from [LeP11].

Since the endflanges have inlets as well as outlets, gas will be compressed on one side of the piston and at the same time expanded on the other side during movement of the piston. In order to enable this, flapper valves have to be used to force the gas flux direction.

The magnetically-coupled piston pump for the EXO-200 experiments fulfills all requirements in terms of purity and reliability for high purity noble gas applications. However, the cylindrical pump with a length of 400 mm and an inner diameter of 65 mm achieves flows of up to 16 slpm at a compression of 1 bar for xenon gas [LeP11], which is not sufficient for recent tonscale experiments. Furthermore, a stronger focus has to be placed on radon emanation at material selection. Radon albeit was not the dominant background, which limits the sensitivity of EXO-200, [Ost16], but the  $\gamma$  line of the isotope  $^{214}\text{Bi}$  (2448 keV [Alb15]), a daughter of  $^{222}\text{Rn}$ , is near the Q-value of the double beta decay (see chapter 1.2). According to that, radon emanation also plays an important role.

Therefore the design and construction of a new pump focuses on a high performance and absolutely cleanliness of all built-in components resulting in an extremely low radon emanation. In the following chapter, this Muenster piston pump and aspects in terms of essential redesign of some parts will be presented.



### 3. The Muenster magnetically-coupled piston pump

In order to fulfil the requirements of present-day tonscale high purity noble gas experiments, a magnetically-coupled piston pump with bigger dimensions and an enhanced magnetic gradient based on alternating polarity for achieving a higher performance was developed.

This chapter will introduce the composition and functionality of our pump. After a presentation of the general layout, several key components will be shown in detail. An upgrade of the magnetic ring is presented followed by the design of the flapper valves, the piston gaskets, a cooling system and the electric cylinder drive. In the end of this chapter, a thermodynamic model of the operation will be discussed.

#### 3.1. General layout

The construction of the pump has been described in [Buß13]. In contrast to the EXO pump, our pump was vertically installed into a framework of Canya to prevent a one-sided abrasion (fig. 3.1).

The cylindrical and non-magnetic stainless-steel pump body with a volume of 4.5l has a length of 520 mm and an inner diameter of 127 mm. The hermetically sealed, laser-welded piston with a length of 155 mm and a diameter of 125 mm contains three cylindrical neodymium magnets with alternating polarity. Thus the magnetization along the cylinder axis is N-S, S-N, N-S.

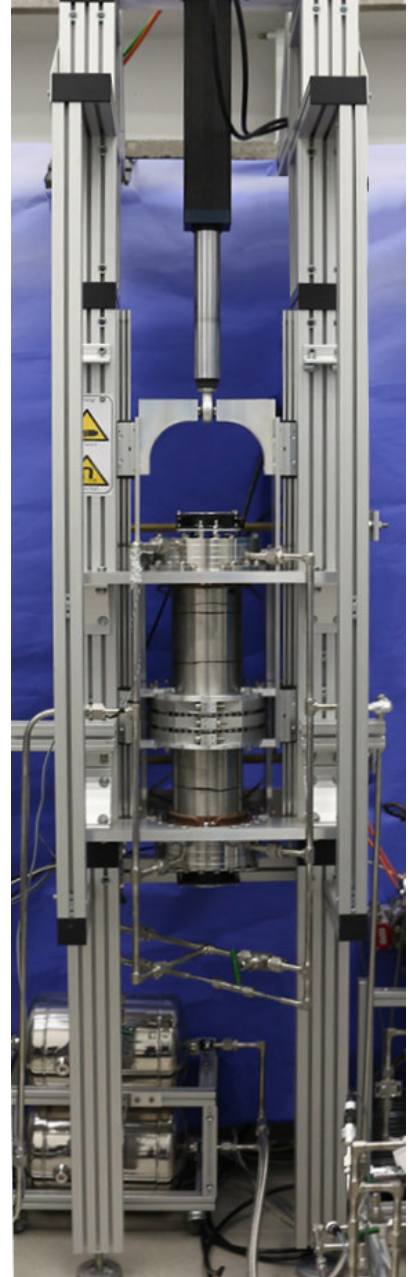
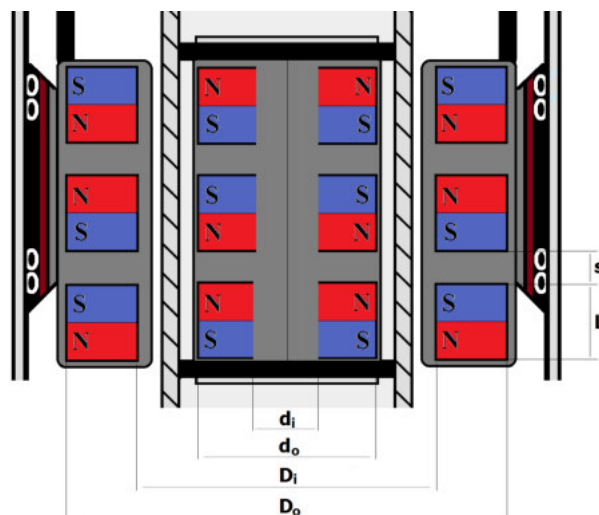


Figure 3.1.: The Muenster pump

This special magnet configuration shown in figure 3.2 forms a closed flux loop around each piston magnet and therefore results in a vast magnetic coupling strength between piston and external ring.



The magnetic field  $B$  within the pump can be simulated by a finite element method with COMSOL Multiphysics [Com]. A vertical displacement of the piston or the external ring respectively leads to a different magnetic field  $B$ , which can be used to calculate the



corresponding restoring force  $\vec{F}$  Here,  $\vec{F}$  can be calculated via

$$\vec{F} = \int_V \vec{\nabla}(\vec{M} \cdot \vec{B}) dV, \quad (3.1)$$

with the magnetic volume  $V$ , the magnetization  $\vec{M}$  and a radialsymmetric magnetic field strength  $\vec{B}$ .

The COMSOL simulations illustrated in figure 3.3) show the restoring forces versus displacement of the piston for different magnet configurations:

- **The EXO-200 configuration** (one magnetic pair) in dash-dotted green: A coupling based on a cylinder piston magnet with N-S orientation in longitudinal direction and an external ring with opposite orientation (S-N) with the following dimensions:

$$L = 51 \text{ mm}$$

$$d_i = 0$$

$$d_o = 25.4 \text{ mm}$$

$$D_i = 45 \text{ mm}$$

$$D_o = 76 \text{ mm}$$

$$B_i = 1.48 \text{ T (magnetic field strength of the inner magnets)}$$

$$B_o = 1.32 \text{ T (magnetic field strength of the outer ring magnets)}$$

- **One pair with increased mass** in dotted red: A coupling based on one magnetic pair but with increased mass and such that realistic designs based on commercial available components are matched:

$$L = 60 \text{ mm}$$

$$d_i = 80 \text{ mm}$$

$$d_o = 120 \text{ mm}$$

$$D_i = 137 \text{ mm}$$

$$D_o = 147 \text{ mm}$$

$$B_i = 1.32 \text{ T}$$

$$B_o = 1.38 \text{ T}$$

- **Three pairs with same orientation** in dashed black: The configuration with the increased mass in red was divided into three equal segments and spaced by  $s$ :

$$L = 3 \cdot 20 \text{ mm} = 60 \text{ mm}$$

$$d_i = 80 \text{ mm}$$

$$d_o = 120 \text{ mm}$$

$$D_i = 137 \text{ mm}$$

$$D_o = 147 \text{ mm}$$

$$B_i = 1.32 \text{ T}$$

$$B_o = 1.38 \text{ T}$$

$$s = 10 \text{ mm}$$

- **The new configuration presented in figure 3.2** in blue: The coupling based on three magnetic cross-coupled rings such that the same poles are pointed longitudinally together for adjacent magnets with a space  $s$  in between:

$$L, d_i, d_o, D_i, D_o, B_i, B_o \text{ and } s, \text{ similar to configuration above.}$$

Figure 3.3 shows the piston of each configuration is in equilibrium when centered within its related external ring magnet, which corresponds to zero displacement. However, a displacement creates a restoring force between concentric magnet pairs:

The EXO-200 magnet configuration (green) features a symmetric behaviour of the restoring force around the displacement of the half magnet height (25.5 mm) with a maximum force of 490 N. This fits to simulations with the MAXWELL software shown in [LeP11]. At a piston displacements higher 51 mm, which corresponds to a complete decouple of the piston from the external ring, a negative restoring force is created due to repulsive forces by opposite polarity of piston and external ring magnets.

In comparison, the simulation of the increased mass configuration (red) contains with a maximum restoring force of 790 N a stronger coupling strength, which is expected due to the larger magnetic mass.

The divided magnet into three segments which are spaced by  $s = 10 \text{ mm}$  (black) features a negligible gain in coupling force. However, several equilibrium points can be observed which results from the three concentric pairs allowing a displacement of only one pair with respect to each of them.

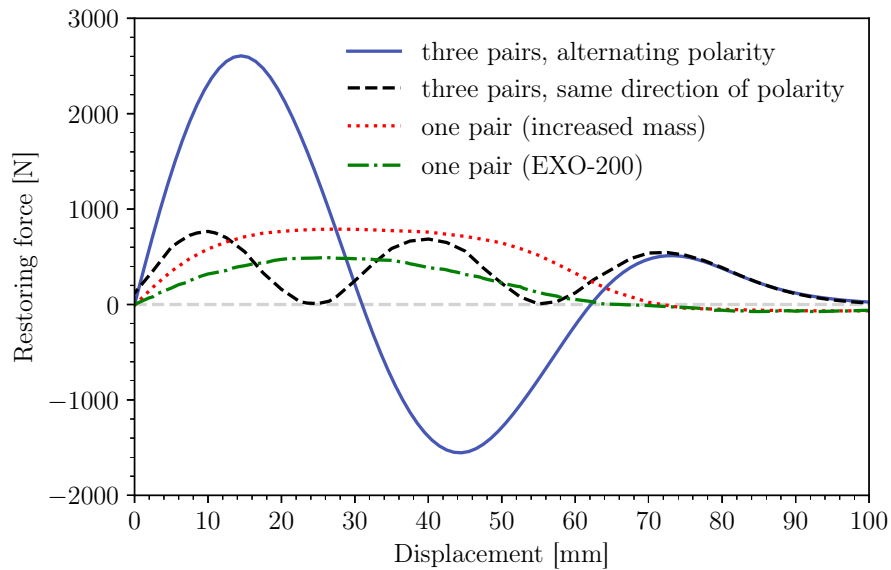


Figure 3.3.: Magnetic field simulation with COMSOL Multiphysics. Restoring force of the piston coupling versus displacement of the piston for several configurations. The EXO-200 pump magnetic configuration is illustrated in dash-dotted green. Another configuration based on one magnetic pair but with increased magnetic mass is shown. Dividing this single magnetic pair into three equal segments with a space of  $L$  in between results in the dashed black line. The new configuration based on alternating orientation of the three magnetic pairs is visualized in blue. The new method increases the maximum restoring force by a factor 3.3 compared to the EXO-200 configuration to 2600 N.

The simulation of the new configuration with alternating longitudinal orientation of the magnets (blue) yields in an additional boost up to a maximum restoring force of 2600 N, which is an increase of a factor 3.3 compared to the EXO-200 configuration.

Therefore, the new configuration creates a distinct higher coupling strength between piston and external ring. Due to reasons of costs and delivery time the external ring was built of  $10\text{ mm} \times 10\text{ mm} \times 20\text{ mm}$  cylindrical oriented bar magnets instead of the simulated ring magnet, which results in a maximum coupling strength of 2480 N between piston and external ring measured in [Buß13].

In order to achieve even higher coupling forces an upgrade of the external ring has been done, which is presented in the following.

### 3.2. Increasing force by upgrading of the external magnetic ring

As mentioned, the prototype of the external ring consists of three magnetic rings. Each ring is made of 40 cylindrical oriented  $10\text{ mm} \times 10\text{ mm} \times 20\text{ mm}$  bar magnets. This way, a maximum coupling strength of 2480 N has been achieved [Buß13]. To reach a stronger coupling with least-effort, an upgrade of the external ring was with  $20\text{ mm} \times 10\text{ mm} \times 20\text{ mm}$  bar magnets. Thus, the laser-welded piston can be used without any changes.

A new COMSOL simulation was performed to calculate potential improvements with the upgraded configuration. Figure 3.4 illustrates the comparison of the expected restoring forces for given displacements for the prototype and the new external ring and shows the restoring force versus displacement for both configurations. At this simulations the bar magnets were considered instead of ring magnets for the external ring.

As explained in the last section, the characteristic restoring force for the prototype ring (blue) as a function of the displacement decreases with less magnetic pairs contributing to the coupling force. The upgraded ring (red) shows similar behaviour, but with a higher effective restoring force.

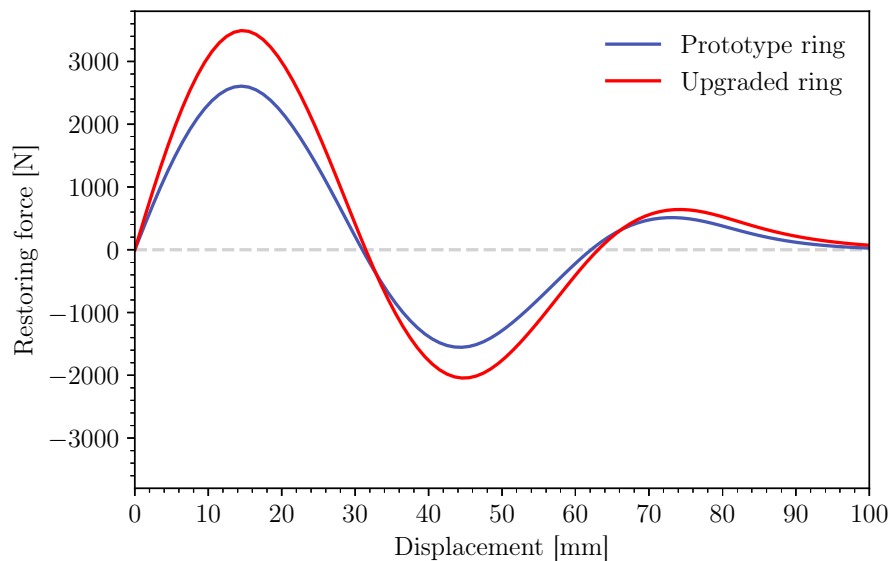


Figure 3.4.: Magnetic field simulation with COMSOL Multiphysics: Restoring force of the coupling versus displacement of the piston for the prototype ring and the upgraded ring.

Due to the fact that the simulation of the prototype with a maximum coupling strength of 2483 N nicely fits the physically measured coupling strength (2480 N), the development of a new outer ring with  $20\text{ mm} \times 10\text{ mm} \times 20\text{ mm}$  bar magnets can be expected to increase the coupling strength by about 40 % to 3483 N.

Therefore, the new external ring has been built such that the final configuration of the pump features the following dimensions:

$$L = 3 \cdot 20\text{ mm} = 60\text{ mm}$$

$$d_i = 80\text{ mm}$$

$$d_o = 120\text{ mm}$$

$$D_i = 137\text{ mm} \quad (40 \cdot (20\text{ mm} \times 10\text{ mm} \times 20\text{ mm}) \text{ bar magnets per ring})$$

$$D_o = 157\text{ mm}$$

$$B_i = 1.32\text{ T}$$

$$B_o = 1.38\text{ T}$$

$$s = 10\text{ mm}$$

The construction has been done in a similar way as in [Buß13]. As mentioned before, the external ring contains three magnetic rings, two with S-N and one with N-S magnetic orientation. Each of these rings itself is composed of two half rings, which requires 20 bar magnets inside with the same magnetic orientation. A careful installation is necessary due to the high magnetic forces. At first, only every second magnet was pushed into the framework. The magnets are held in place by individual washes and M6 screws presented in figure 3.5.

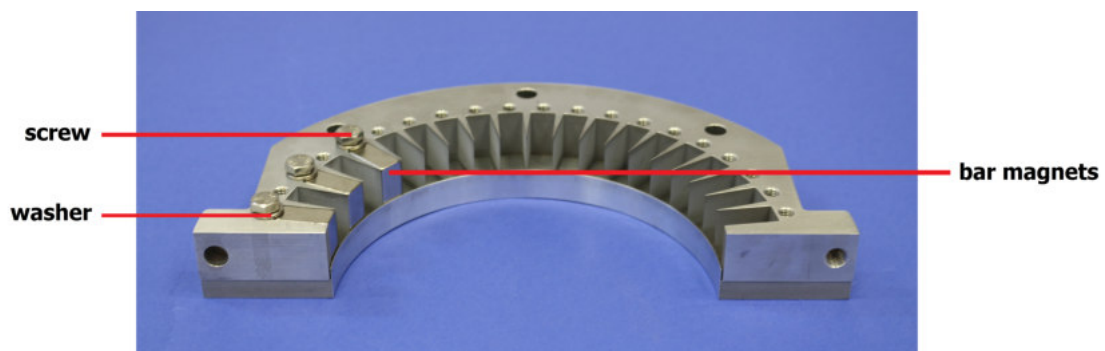


Figure 3.5.: One half ring of the new external ring. Only every second bar magnet was pressed into the framework at the beginning of installation due to the high magnetic forces.

Then, the remaining holes are filled with even more care, since attraction forces quadratically increase with the distance analogous to Coulombs law. This procedure has to be repeated to get three times two half rings with caution for the right polarization. Afterwards, one half of the external ring can be built by pushing three of the half rings together with the help of two guide rods such as in figure 3.6.

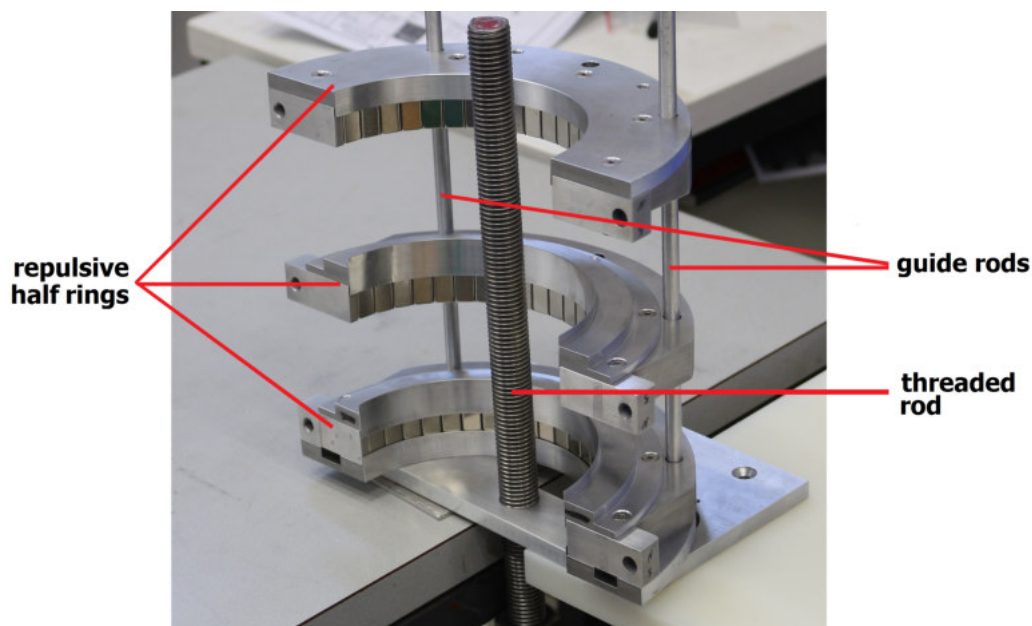


Figure 3.6.: The magnetic repulsion of the three half rings with alternating polarity illustrates the strong forces.

Same poles on adjacent half rings result in a strong magnetic repulsion, which pushes the rings apart. The repulsive half rings are then pushed together by a M20 threaded rod with tighten screw and an iron sheet (fig. 3.7). The plastic foil is used to reduce sticking friction.

After substitution of the guide rods by M8 threaded rods, which constrain the half rings together, the M20 threaded rod can be removed. The whole procedure has to be repeated for the second half ring. Finally, the two big half rings can be connected surrounding the pump body.

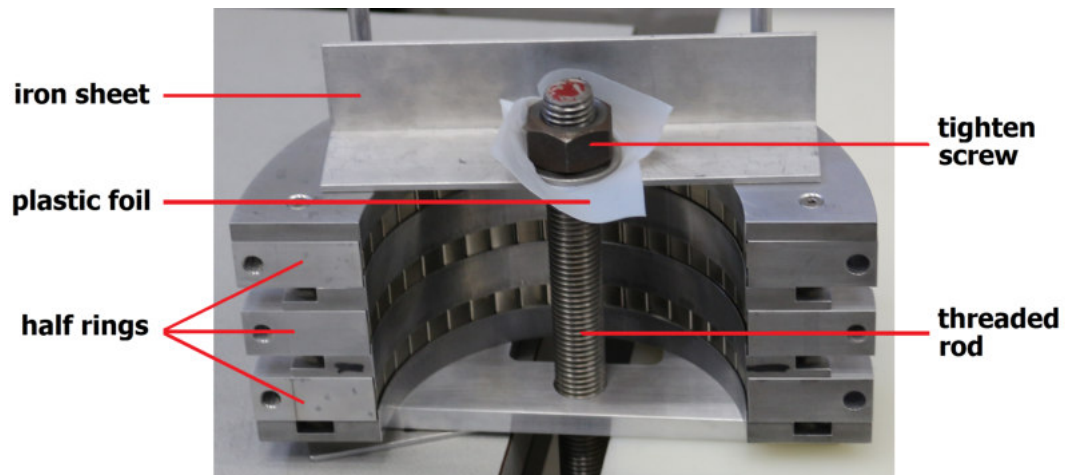


Figure 3.7.: Only with use of a M20 threaded rod with nut the rings can be brought together. Afterwards the long guiding rods will be substituted by M8 threaded rods with nuts.

Figure 3.8 shows the two external rings, the prototype with the small  $10\text{ mm} \times 10\text{ mm} \times 20\text{ mm}$  bar magnets (top) and the new external ring with the bigger  $20\text{ mm} \times 10\text{ mm} \times 20\text{ mm}$  bar magnets (bottom). Afterwards, the prototype has been removed and the new ring has been attached to the rail carriage. In order to couple in the piston to the external ring, the external ring has been fixed and the piston has been slowly moved downwards by a gearing mechanism presented in 3.9.

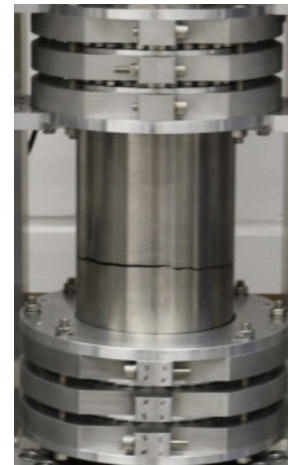


Figure 3.8.: Prototype external ring (top) and the new external ring (bottom).

The external ring is fixed by Kanya frames to avoid moving up and down. The top flanges of the pump are removed and a threaded rod connects the piston to a gear. Now the piston can be moved up or down with a drill machine via the gear, which absorbs the alternate attraction and repulsion forces occurring by the special magnet configuration.



Figure 3.9.: Construction to couple-in or decouple the piston from the external magnetic ring: The external ring is fixed by Kanya frames, and the piston can be moved via a threaded rod and a gear by a drill machine.

This construction can also be used to measure the coupling forces physically with a load cell. The load cell registers weights by smallest changes of resistance via strain gauges. For this purpose, the load cell gives voltages, positive for stretching and negative for compression. At first, the cell has been calibrated by different weights, which leads to a calibration factor of

$$C_{\pm} = (0.0175 \pm 0.0021) \frac{\text{mV}}{\text{kg}}. \quad (3.2)$$

The force  $F$  affected on the load cell by repulsion as well as attraction can be calculated by the measured voltage  $V$  of the load cell with

$$F = V \cdot \frac{g}{C_{\pm}}.$$

The gravitational constant  $g$  is  $9.81 \text{ N/kg}$ .

Thus, the implementation of the load cell between gear and piston enables the opportunity to measure the restoring forces during displacement of the piston. The voltages  $V$  of the cell have been measured at approximately constant, but unknown, revolutions per minute of the drill machine, such that the displacement is assumed to be linearly in time.

Figure 3.10 illustrates the corresponding restoring force depending on the time of the displacement.



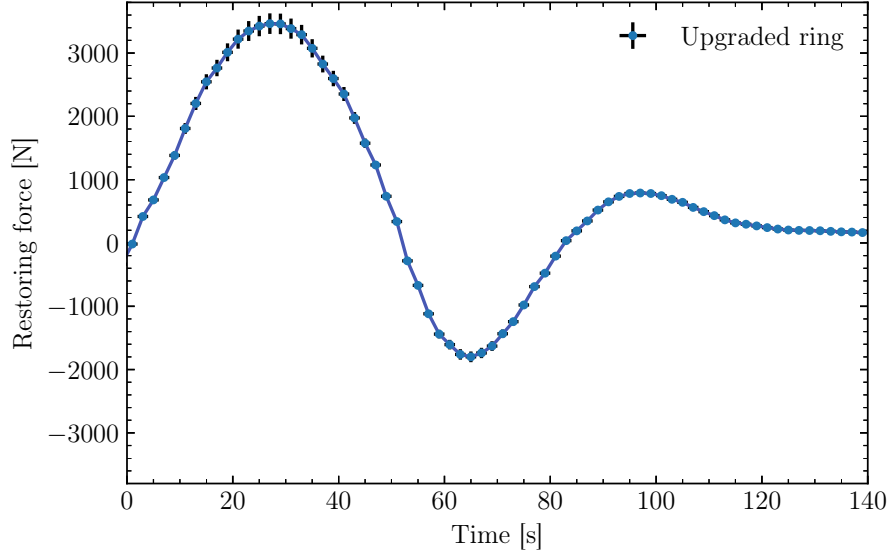


Figure 3.10.: Restoring force per time of the piston displacement measured by a load cell.

The x-error bars result from the time deviation of data recording, however the y-error bars are calculated by

$$\Delta F = \sqrt{\left(\frac{g}{C_{\pm}} \cdot \Delta V\right)^2 + \left(V \cdot \frac{g}{-C_{\pm}^2} \cdot \Delta C_{\pm}\right)^2},$$

with  $\Delta V = 0.005 \text{ mV}$  created by the multimeter.

Since the measurement looks similar to the simulation, the assumption of constant revolutions per minute of the drill machine can be verified. However, the physically measured restoring force doesn't go back to zero due to the own weight of the piston. Furthermore, the own weight makes the major contribution to decoupling occurring primarily during the up movement. The maximum coupling force has been physically measured to  $(3468 \pm 28) \text{ N}$ , which is in agreement with the simulation.

A coupling force can be translated into maximum pressure on the cross section of the piston before it starts to move out of equilibrium, such as

$$\Delta P_{piston_{max}} = F/A_{piston} \quad (3.3)$$

Therefore, a coupling strength  $F$  of  $(3468 \pm 28) \text{ N}$  corresponds by to a pressure difference  $\Delta P_{piston_{max}}$  of  $(2.74 \pm 0.03) \text{ bar}$  between above and beneath the piston without consideration of friction.

Where the error is calculated by the error propagation with  $\Delta r = 0.25$  mm, since the outer diameter of the gaskets should be between 126.5 mm and 127 mm, which will be seen later. Consequently, the pressure difference beneath and above the piston  $\Delta P_{piston}$  should not exceed  $P_{piston_{max}}$ , otherwise the piston will be decoupled from the external ring.

So as to compress gas, the external ring and thus the coupled piston can be moved up and down on rails by a drive. However to provide a compression and thus positive gas displacement at all, the gas flow has to be forced to a certain direction. This is done by valves.

The so-called flapper valves allow by their special design a unidirectional flux. Therefore, each single stroke leads to compression on one side, and at the same time expansion on the other side. The next section will focus on the flapper valves.

### 3.3. Flapper valves

In order to achieve a one-directional flux of the pump, submillimeter-thin stainless steel plates are installed to the Conflat flanges (fig.3.11) to prescribe the gas flow direction for suction and discharges.

This kind of plates is called reed valves and are automatically controlled by the pressure differences between both sides of the plate. A distinct pressure difference, with the pressure on the opening side as the lower pressure, is required to open the valve. As shown in [Buß16] the flapper valves only open due to inertia almost at the point of highest compression. The opening results in pressure equalization. Only when the pressure on the opening side is lowered below the equalization pressure such that the inertia is exceeded, the valve closes again.

Our reed valves are provided by a rigid stainless steel blocker for a maximum opening to avoid deformations at opening. Additionally, the screws of the flappers and their blockers are secured by safety wires. On the other hand, as presented in more detail in [Buß16], a grid prevents a soak-in of the flappers.

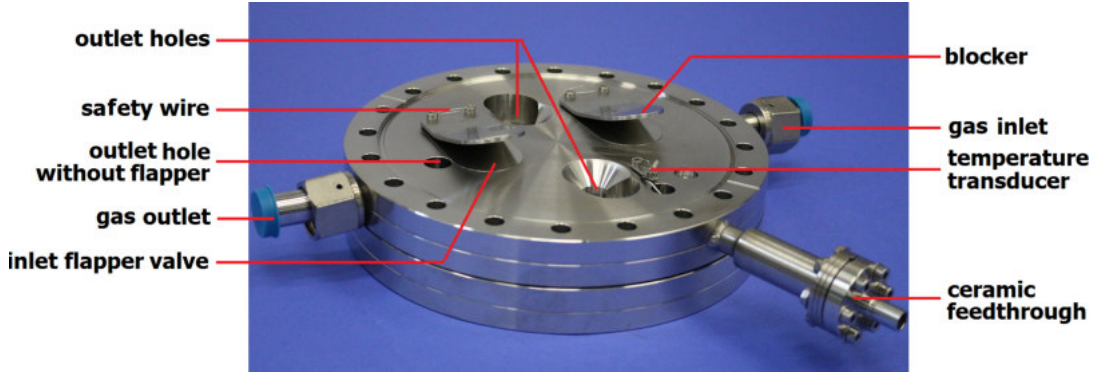


Figure 3.11.: Conflat flanges of the top of the pump body. The upper flange in the picture contains a gas inlet (top/right) connected to two flapper valves. A gas outlet line (left) enclosed from recirculation circuit without flapper is installed to measure the pressure inside the pump and a ceramic feedthrough for a temperature transducer (bottom/right) is used.

Certainly, the opening also depends on the thickness of the flappers. Thicker flappers reduce the maximum flow rate by less and later opening and causes over-pressure, however thinner flappers oscillate at high pressure differences of both sides of the valve and can deform. Therefore, the investigation of the optimal thickness is of crucial importance.

The oscillations at high pressure differences occur similar to the flaps of an oboe, where such pressure controlled gas flow valves provide the sound generation.

The motion of such valve oscillations can be described by the superposition of its normal modes of vibration. As an illustration, figure 3.12 shows the first four normal modes of such flapper valve vibration.

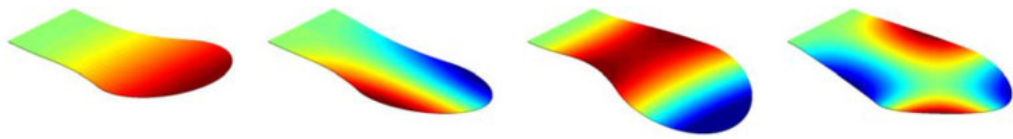


Figure 3.12.: Illustration of typical normal modes for the vibration of flapper valves [Gon17].

Each normal mode  $i$  features an individual frequency  $\omega_i$  and mode shape  $\phi_i(x, y)$  in  $z$ -direction, such that the displacement pattern can be described by

$$d_z(x, y, t) = \sum_{i=1}^{\infty} q_i(t) \phi_i(x, y), \quad (3.4)$$

where  $q_i(t)$  is the generalized coordinate. Using the kinetic energy of the vibration

$$T = \frac{1}{2} \int_0^l \rho A(x) \dot{d}_z^2 dx, \quad (3.5)$$

with the length of the valve  $l$ , the density of the valve material  $\rho$  and the cross-sectional area  $A(x)$  of the valve, the governing equation of motion for each vibration mode of the valve is

$$\ddot{q}_i + 2\zeta\omega_i\dot{q}_i + \omega_i^2 q_i = f(t), \quad (3.6)$$

where  $\zeta$  is the damping coefficient and  $f(t)$  is the generalized force, which can be calculated by the work of external load. A detailed view is given in [She02]. This linear theory is only sufficient for small oscillations compared to the valve thickness. For large vibrational amplitudes a nonlinear term has to be added.

In our case, the motion of the stainless steel flappers leads to a loud noise outside the pump. In addition, more increase of the pressure difference between both sides of the flapper valve results in continuous oscillations, which reduces the performance due to constant opening of the flappers. Furthermore, oscillations over a long time might create ruptures of the flappers.

Therefore, different thicknesses of the plates have been tested with the ambition to find either a compromise between oscillating and non-opening flappers, or flappers, which are thin enough, such that they are pressed towards the steel blockers at a maximum opening with the result that the swinging is prevented. However, flappers with a thickness below 0.05 mm were ruled out due to permanent deformations after pump operation [Buß16].

The tested thicknesses within this thesis are summarized in table 3.1. The related behaviour refers to the maximum possible performance without decoupling of the piston at several speeds of the drive with several amounts of xenon gas inside the system. Except for the 0.5 mm valves all flapper valves behave similar at several configurations of amount of xenon gas, speed of the drive and specific inlet pressure.

Table 3.1.: Tested flapper valve thicknesses.

Thickness [mm]	Behaviour
0.05	oscillating
0.2	oscillating
0.3	oscillating
0.5	config-dependent
0.7	no enough opening

As shown in table 3.1, the thin plates up to a thickness of 0.3 mm result in oscillations. Further increase of the drive speed, which leads to higher compressions, results in a continuous oscillation and thus a decrease of the performance.

Flapper valves of 0.7 mm thickness cannot provide any compression. Combined with a gas flow noise, it seems reasonable to assume that the 0.7 mm flappers open not enough, such that the gas is pressed alongside the piston.

The 0.5 mm flapper valves also show vibrations. Nonetheless, different measurements show that the oscillation of the valves with this thickness depends on the specific configuration of inlet pressure, amount of gas in the system and flow in contrast to the other thicknesses. Therefore, further qualitative investigations of the 0.5 mm valves are required.

All in all, the flapper valves allow the uni-directional flow and allow compression, albeit no optimal thickness has been found. In the following all performance measurements in chapter 4 have been done with the 0.2 mm flapper valves, since the other thicknesses were at that time under construction. For safety reasons, long-term measurements have been done below maximum performance at a level of compression without vibrations.

To provide compression at all, the piston has to be sealed. Thus, piston gaskets of an advanced polymer are used. Due to the fact that special requirements in terms of for example heat resistance and purity are essential, the next section will zoom in on the investigation of piston gaskets.

### 3.4. Piston gaskets

The non-metallic piston gaskets are not only important for sealing between above and below the piston to achieve compression, but also to prevent a steel-to-steel contact of the piston and the cylinder wall. Additionally, it keeps the piston in a central position. For this purpose, a large contact surface is required. However, a large contact surface potentially results in more friction leading to more wear as well as a stronger evolution of heat. Therefore, a sophisticated design combined with a suitable material with special properties is required. In the following, the old piston gasket design compared to a new design is presented following by several tested materials with a zoom in on their specific characteristics.

## Design

A piston gasket is a ring at the endcaps of the piston, with a bigger radius than the piston to provide sealing between piston and cylinder wall. Figure 3.13 shows the old gasket design.

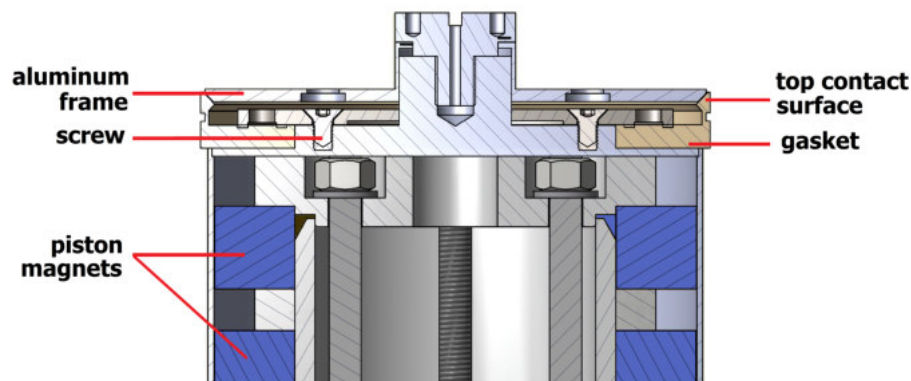


Figure 3.13.: CAD drawing of the piston. The gaskets contain two contact surfaces. Drawing by C.Huhmann.

The CAD drawing presents a cross section of the top of the piston, such that one and a half piston magnet rings can be seen. An aluminum frame at the endcap of the laser-welded piston is used to fix the piston gaskets. The special design contains two contact surfaces with the cylinder wall per gasket, which results in a high sealing and thus low leakage along the piston.

However, pressures towards the endcaps of the piston will press the top contact surface of the piston gasket away towards the cylinder wall of the pump body. This results in a better sealing, but can also provide a fixation of the piston, which could lead to a decoupling of the piston. The design additionally features a complex machining process due to the small and precise top contact surface. Moreover, the design contains a high dead volume on the endcaps of the piston by the way of mounting. A detailed view of the design is given in [Buß16].

Therefore, a redesign of the gaskets has been developed presented in figure 3.14, which avoid movement of the top contact surface and thus prevent potential fixations. Furthermore, the machining has been simplified and the dead volume has been reduced.

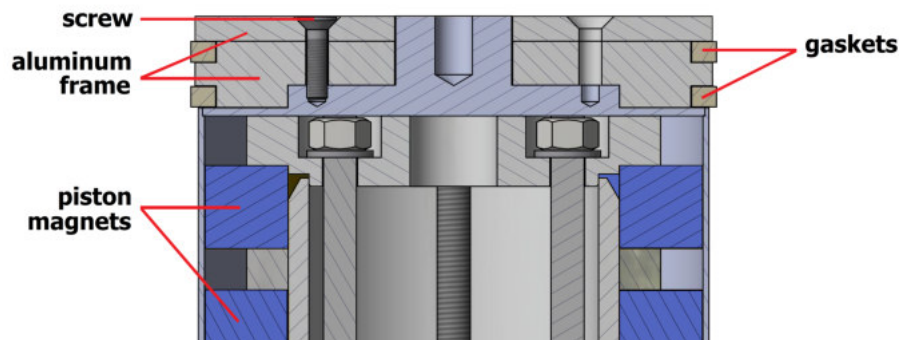


Figure 3.14.: CAD drawing of the piston. Beside the new gasket design in the form of two rings, the dead volume has been reduced by a larger aluminum frame. Drawing by C.Huhmann.

The design has been changed into two individual and simple gasket rings. The double-sealing by two contact surface was remained, but the sealing is not pressure dependent anymore, such that potential fixations can be excluded. The simplification of the design results in a decrease of the expenditure in manufacturing for the workshop. Additionally, most of the dead volume has been filled with a larger aluminum frame.

In order to provide compression, the piston gaskets with a height and depth of 5 mm contain an outer diameter between 126.5 mm and 127 mm. Accordingly, bigger gaskets are convenient for pumping lighter noble gases, since the leakage along the piston increases with lighter gases. However, more sealed gaskets result both in a higher compression as well as in more friction and heat. Therefore, a reasonable compromise has to be found depending on the atomic mass and density of the displaced gas.

## Material

Piston gaskets demand for special material properties. Next to good wear and abrasion resistances, the piston material has to feature good sliding friction properties and heat resistance due to enormous friction forces over long-term. Especially for low background experiments with high purity noble gases, the absence of oil-based lubrication as well a low radioactive outgassing has to be guaranteed.

The old gaskets are made of Ultra-High Molecular Weight Polyethylen (UHMWPE). The UHMWPE features good properties in terms of wear and abrasion resistance compared to most advanced polymers due to the high density and the parallel orientation of the linear PE fibers. The radioactive emanation is negligible. Its coefficient of linear thermal expansion of  $200 \times 10^{-6} \text{ 1/K}$  is higher than usual [PTI11]. Moreover, only temperatures of about  $42^\circ\text{C}$  are needed for heat distortions of the material [PoK18]. Since the unstable character of the early pump presented in [Buß16], which leads to decoupling of the piston, occurred most likely by gasket expansion, a few materials have been tested summarized in the following. Table 3.2 shows the piston gasket material candidates

- Ultra high molecular weight polyethylen (UHMWPE)  $\left[ \begin{array}{c} \text{H} \quad \text{H} \\ | \quad | \\ \text{---C---C---} \\ | \quad | \\ \text{H} \quad \text{H} \end{array} \right]_n$
- Polyethylenetherketone (PEEK)  $\left[ \text{---} \langle \text{benzene} \rangle \text{---O---} \langle \text{benzene} \rangle \text{---O---} \langle \text{benzene} \rangle \text{---C(=O)---} \right]_n$
- Polyamidimid (Torlon)  $\left[ \begin{array}{c} \text{O} \\ || \\ \text{N} \end{array} \text{---} \langle \text{benzene} \rangle \text{---} \begin{array}{c} \text{O} \\ || \\ \text{N} \end{array} \text{---} \langle \text{benzene} \rangle \text{---O---} \langle \text{benzene} \rangle \right]_n$
- Polyimidimid (Vespel)  $\left[ \begin{array}{c} \text{O} \\ || \\ \text{N} \end{array} \text{---} \langle \text{benzene} \rangle \text{---} \begin{array}{c} \text{O} \\ || \\ \text{N} \end{array} \text{---} \langle \text{benzene} \rangle \text{---O---} \langle \text{benzene} \rangle \right]_n$

Table 3.2.: Piston gasket materials with relevant material properties. The data has been taken from several data sheets [PTI11, PoK18].

	Coefficient of linear thermal expansion [ $10^{-6} \text{ 1/K}$ ]	Heat distortion temperature [ $^\circ\text{C}$ ]	Dynamic sliding friction coefficient	Wear rate [ $\mu\text{m/km}$ ]	Radon screened
UHMWPE	200	42	0.15-0.3	8	yes
PEEK	55	152	0.3-0.5	28	yes
TORLON	40	280	0.35-0.6	5	yes
VESPEL	55	360	0.3-0.4	7	not tested

The color codes of table 3.2 is as following: Red indicates a value which is out of the range for a suitable gasket material based on our experiences. Orange shows a doubtful and green a positive property.



First of all, a polyetheretherketone (PEEK) has been tested. PEEK is an organic thermoplastic polymer with an amorphous/semicrystalline structure and a density of about  $1.3 \text{ g/cm}^3$  [PoK18]. It is characterized by a large heat resistance in the form of a coefficient of linear thermal expansion of  $55 \cdot 10^{-6} \text{ 1/K}$  and a heat distortion temperature of  $152^\circ\text{C}$ . These properties prevent deformation and expansion of the gaskets by heat evolution. Furthermore, PEEK is radon screened and is already used in low background experiments [Apr17c].

After 43 hours of operation with PEEK piston gaskets, the pump has been opened. A high abrasion in terms of a lot of small PEEK particles have been accumulated within the whole pump as visualized in figure 3.15.

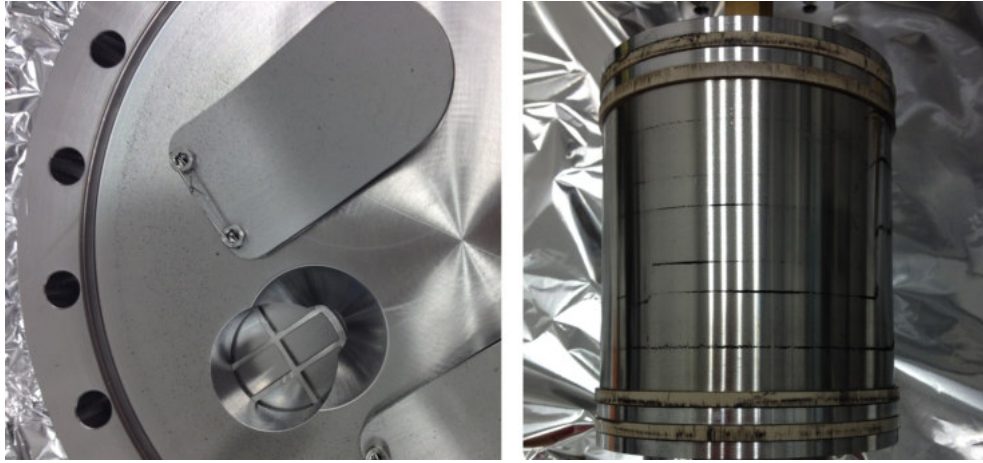


Figure 3.15.: After 43 hours operation with piston gaskets of PEEK. *Left*: Top flange of the pump. A high abrasion can be seen by small PEEK particles. *Right*: magnetic piston with the PEEK gaskets on both endcaps. The electrostatic PEEK particles are oriented alongside the inner magnetic rings of the piston.

The wear rate of  $28 \mu\text{m/km}$  seems to be too high. Therefore, it was marked red in table 3.2 This assumption can be investigated by microscopic pictures of the surface before and after operation with this gaskets.

Figure 3.16 shows that the unused PEEK gaskets (left) have a amorphous surface. The peek piston gaskets used for 50-60 hours (right) show many parallel cracks on the surface with large spots of material accumulation. Therefore, it was confirmed that PEEK features a too high abrasion as a piston gasket material.

Second, piston gaskets of the polyamidimid with the trademark Torlon by Solvay Industries [Sol17] has been tested. Torlon has a cross-linked/amorphous structure with a density of about  $1.4 \text{ g/cm}^3$  [PoK18]. Due to their many aromatic components within the polymer chain, it is one of the most stable polymers based on hydrocarbon.

This advanced polymer distinguished itself by excellent heat and abrasion resistance. Moreover, Torlon is commonly used in low background experiments due to its high purity combined with unique characteristics.

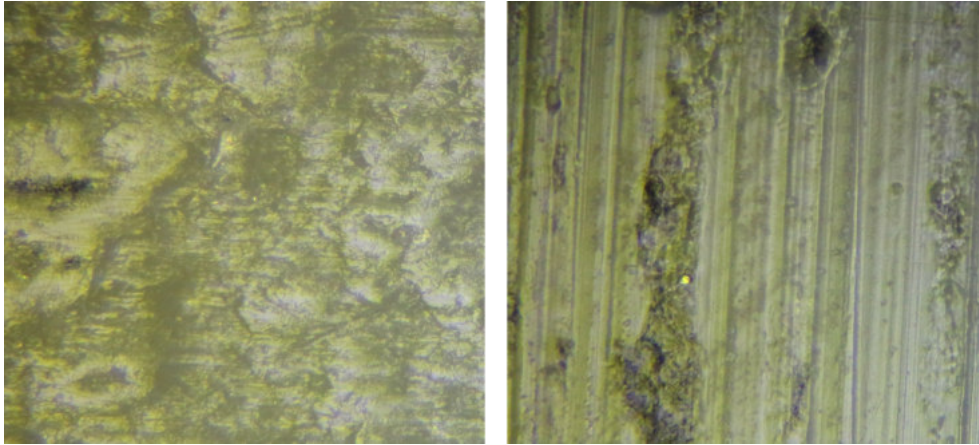


Figure 3.16.: *Left*: The surface of the unused gasket seems to be rough and craggy. *Right*: The PEEK gasket used for 50-60 hours shows deep notches from top to bottom. All together, the surface looks less rough and craggy than the unused one, but partially with large material accumulations.

But to feature the wear rate of table 3.2, the raw Torlon has to be cured by baking with high temperature in advance, which decreases the wear factor. The length of the cure cycle depends on the dimensions of the parts. Figure 3.17 illustrates the post-cure cycle for parts with small thicknesses in the range of millimeters such as our piston gaskets.

The temperature has to be increased stepwise over three days up to 260 °C (dotted). Afterwards the temperature has to be held at 260 °C for the whole cycle. The rapid decrease of the wear factor is shown starting from day 5 (blue line). Additionally, the wear rate of table 3.2 for Torlon of 5  $\mu\text{m}/\text{km}$ , which is reached after 9.5 days, is marked (red line).

We stopped the curing after 11 days. According to figure 3.17 the wear has been improved by a factor of more than ten.

However, the operation of the pump with the post-cured gaskets failed and the pump had to be stopped after a few strokes. The gaskets rubbed with a loud noise towards the cylinder wall. A possible reason for such behaviour could be the higher dynamic sliding friction coefficient of Torlon of 0.35 – 0.6 compared to other materials.

Nonetheless, another pair of Torlon gaskets, but without curing, was prepared to verify the assumption that the sliding friction is too high. Finally, the raw Torlon gaskets show

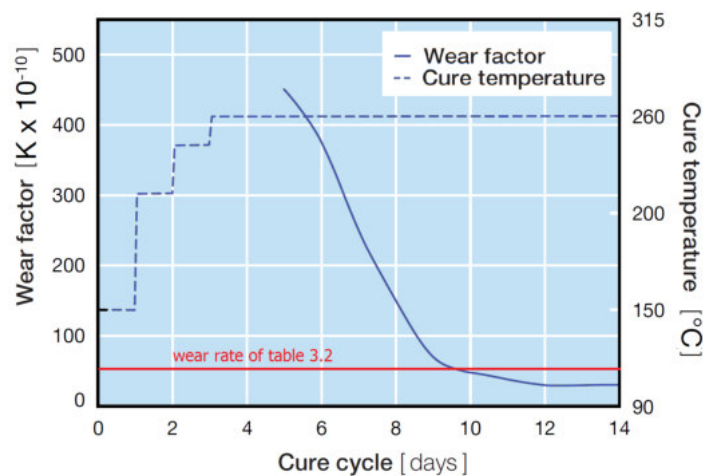


Figure 3.17.: Post-cure process for Torlon parts which is required to improve the wear resistance [Sol14]. The temperature is increased over a few days to 260 °C to reduce the wear factor  $k$  by a factor of more than ten.

a similar behaviour but only after a few hours of operation.

A microscopic analysis of the surface combined with the chemical structure of a polyamidimid might clarify this behaviour. Figure 3.18 presents the raw Torlon piston gaskets before operation (left) and after operation (right).

The piston gaskets before operation show an amorphous surface with spots of high reflection. The microscopic analysis after operation shows horizontal notches, normal to the running direction of the piston. Moreover, material accumulations can be seen at some points.

Figure 3.19 illustrates the post-cured Torlon gaskets before operation (left) and after operation (right). The gaskets before operation feature a flatter surface than the unbaked gaskets and without high reflecting spots. Therefore, the most likely impurity accumulations on the surface have been baked out. However, the gaskets after a few minutes of operation show a mesh structure. This structure is clearly more visible in contrast to that of the raw gasket, since the loud noise resulting from the strong rubbing towards the cylinder wall directly has happened and became stronger and stronger. Compared to the raw gaskets no actual material accumulations can be seen furthermore.

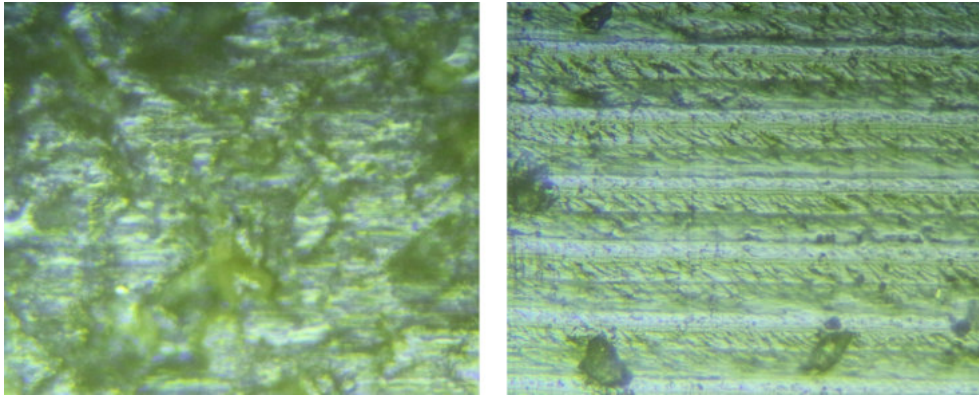


Figure 3.18.: *Left*: The unused piston gasket surface of raw Torlon seems to be rather rough and structureless similar to PEEK. Conspicuously, the surface shows high reflecting spots. *Right*: After a few hours of operation with the raw Torlon piston gaskets, notches orthogonal to the running direction of the gaskets within the cylinder of the pump can be seen on the surface. Furthermore, an approach of a mesh structure is shown by slight vertical strips and few accumulations of gasket material are present.

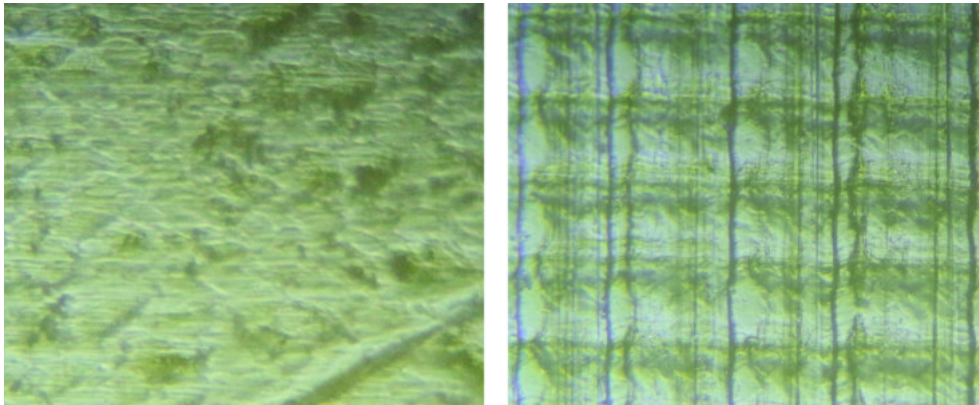


Figure 3.19.: *Left*: The surface of the post-cured, unused piston gaskets seems to be distinct flatter than the surface of raw Torlon (fig. 3.18). Additionally, the high reflecting spots cannot be seen anymore. *Right*: After less than one hour of operation, the surface of the post-cured gaskets shows a mesh structure.

All in all, the noise is assumed to originate from a strong rubbing of the gasket with the cylinder wall. This assumption is confirmed with the microscopic pictures. In the case of the raw Torlon, the noise appears only after a few hours, while for the post-cured Torlon the noise is directly generated at each stroke.

Torlon possesses many impurities on the surface, which can desorb by baking. This fits to the data sheets in terms of mixture absorption and can explain the behaviour as a piston gasket material: The raw Torlon can be used for a few hours, since Torlon features high mixture absorption.

Data sheets of the several materials show the following values for saturation in water [PoK18]:

Table 3.3.: Mixture absorption of several gasket materials

Material	Saturation in water [%]
UHMWPE	<0.1
PEEK	0.45
Torlon	4.4

Table 3.3 indicates that the mixture absorption of UHMWPE is low with a saturation in water of < 0.1%. However, Torlon features with 4.4% almost a factor ten higher saturation in water than PEEK.

It can be concluded, that Torlon features with 0.35 – 0.6 a sliding friction coefficient that is too high, however the water within the raw Torlon is working as a lubricant. After hours of operation, water is outgassing due to the heat evolution and removed by friction. Consequently, the noise evolution starts to appear after a few hours.

Finally, neither raw nor post-cured Torlon can be used as gasket material.

Another promising piston gasket material can be the advanced polymer Vespel by Dupont, which has fantastic heat resistance properties, a good wear rate and a lower dynamic sliding friction than Torlon as well as PEEK. Vespel has not yet been screened for radon emanation. Therefore, it was not further tested in the scope of this thesis. However, it would be an interesting alternative for the future.

After these extensive investigations, UHMWPE remains the favored material. In order to compensate its expansion at higher temperatures, a cooling system was developed. The following section presents our three-component cooling system.

### 3.5. Cooling system

After 90 minutes of operation, the piston decoupled due to an instant fixation of the piston by gasket expansion during continuous movement of the outer magnetic ring [Buß16]. Therefore, a cooling system has been developed, which manages the unstable heat evolution.



The heat evolution is composed of two factors, friction heat and compression heat: The friction heat depends on the speed of the up- and down-movement and the contact surface between piston and cylinder wall. The compression heat is produced by the compression of the process gas and can be approximated by an adiabatic change of state of the gas without consideration of heat losses with the environment.

A cooling of the complete pump body by submerging it into a cooling medium such as water is complicated due to the continuous movement of the external ring. Therefore, a three component cooling system has been developed. A copper heat exchanger is flooded with cooling water to precool the gas before entering the pump (fig. 3.20). This way, the compressed gas within the pump possesses an initial temperature of about 15 °C.

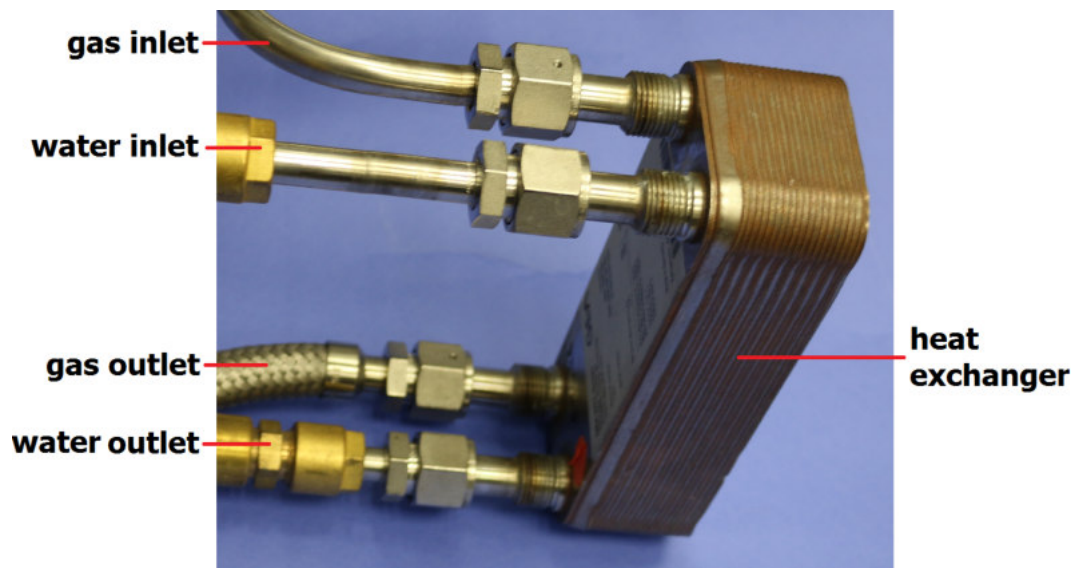


Figure 3.20.: Copper heat exchanger to precool the noble gas at the inlet of the pump. The heat exchanger is flushed with cooling water such that the inlet gas is cooled down to about 15 °C.

Additionally, fans with 2450 rpm and a power of 14 W on both endcaps cool down the flanges. The key components to stabilize the heat evolution are two copper shells installed directly above the bottom flange as well as just beneath the top flange as illustrated in figure 3.21. These shells are flushed with cooling water to remove heat from the location of highest gas compression. as illustrated in figure the figure.

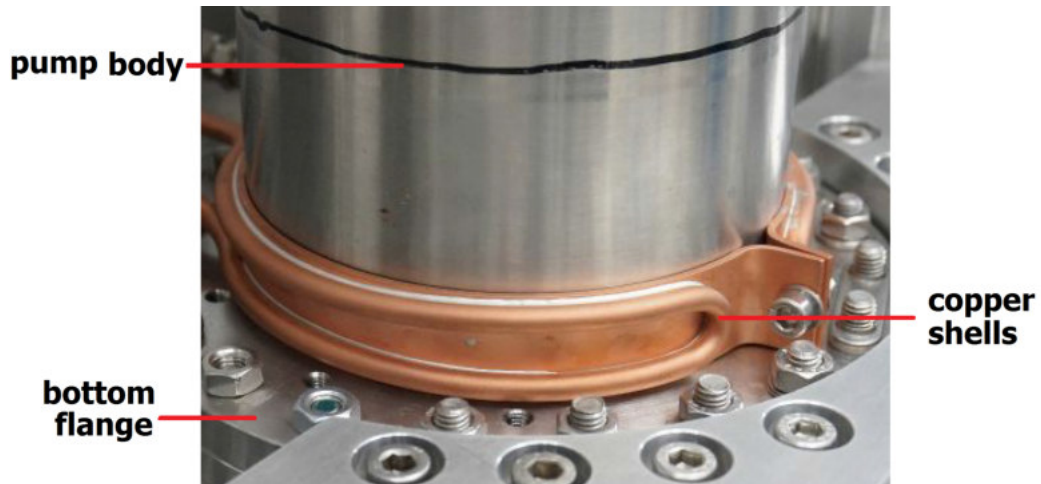


Figure 3.21.: Copper cooling shells flushed with cooling water.

Furthermore, the new linear drive motor requires cooling water as well for operation. Its functionality will be explained in the next section.

### 3.6. Linear drive

A gear motor connected to a crankshaft by a con-rod has been used to move the external ring on rails up and down. This is described in detail in [Buß16].

Due to high wearing at the con-rod and thus much maintenance work we exchanged the motor by a linear drive consisting of an electric cylinder (SEW, CMS) (fig. 3.22) combined with a frequency converter (SEW, MDX 61B).

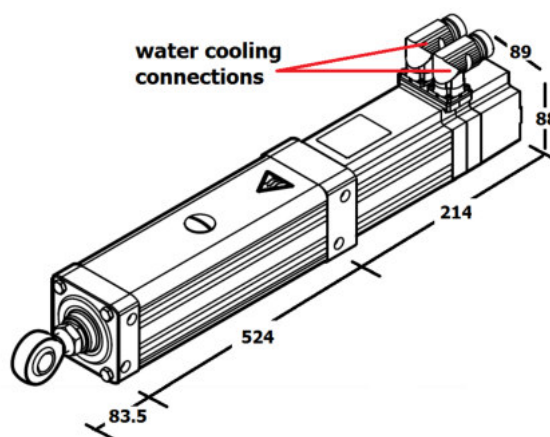


Figure 3.22.: Electric cylinder CMS63 with dimensions in millimeter for the 400 mm stroke length version [SEW09].

The linear connection between electric cylinder and external ring facilitates the justification of the ring on the rails. Thus, abrasion of the rails has been lowered. The cylinder contains a maximum lifting power of 10 kN and a maximum stroke length of 400 mm, which is sufficient for our pump. The rpm range goes from  $-6000$  rpm to  $+6000$  rpm with a nominal current of 9.5 A.

Additionally, the electric cylinder is equipped with connections for water cooling and allows a maximum water flow of 4 l/min which can increase the thermal capacity of the drive by up to 25 % [SEW09].

SEW provides the controlling by their engineering-software MOVITOOLS [SEW18], which allows easy implementing, controlling, diagnostics and communication of the converter and electric cylinder (fig. 3.23).

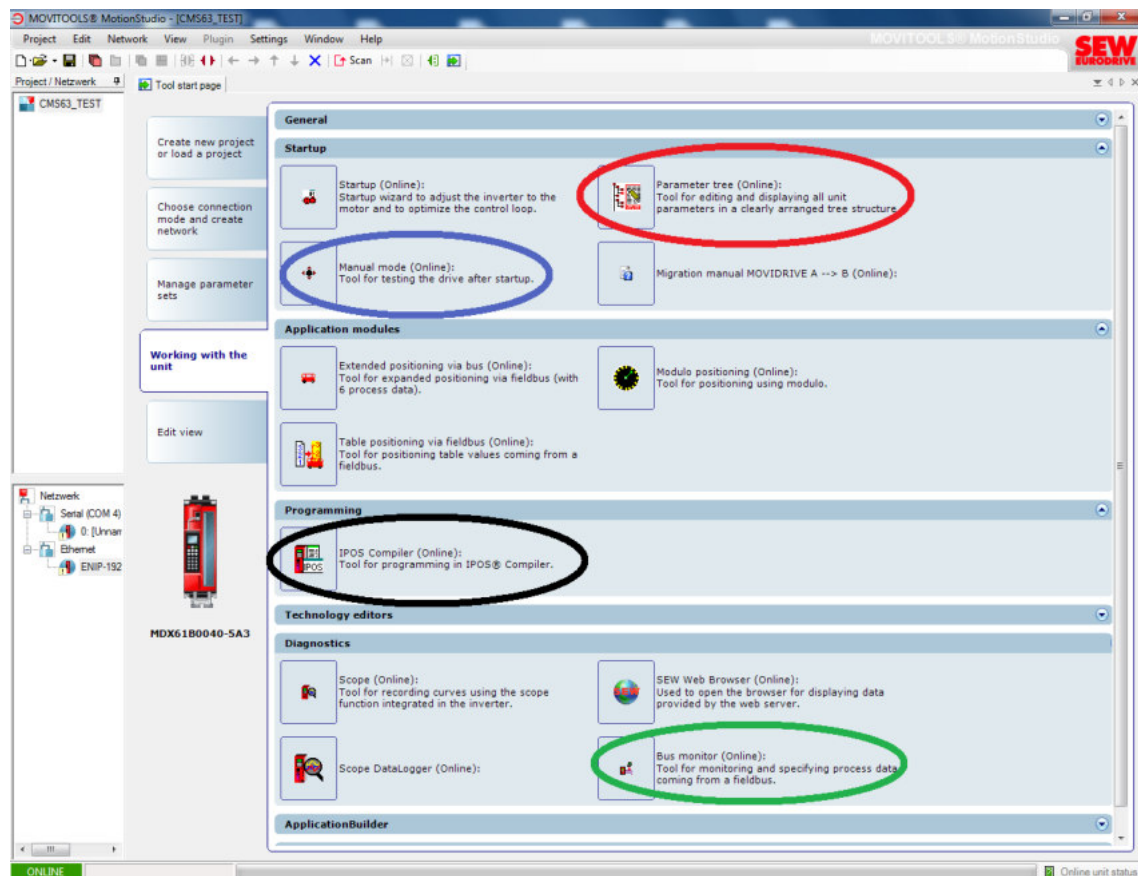


Figure 3.23.: SEW MOVITOOLS - Implementing, controlling, diagnostics and the communication of the converter and electric cylinder is allowed by this SEW software.



After startup, a full access of all parameters via the *Parameter tree* (red) is enabled. Furthermore, the *Manual mode* (blue) gives the opportunity to drive manually up or down with a predefined speed and to calibrate the drive position. This is of crucial importance for an automation of the movement.

In order to automate the movement, the *IPOS Compiler* (black) has to be used. The positioning and sequence control IPOS of MOVITOOLS enables the possibility of a user program combined with a point-to-point positioning. With the help of the manual [SEW18], a simple user program for an up and down movement of the electric cylinder has been created via *IPOS Compiler* and can be found in the appendix (A).

A user program, which is shown in the appendix, is composed of a header and a head function. The header (fig. A.2) consists of attaching header data frames for access to system functions and the declaration of used variables. The head function itself contains functions for safety reasons, the initialization of parameters (fig. A.3) and the main structure for the movement (fig. A.4).

Additionally, a great advantage of this automation with the *IPOS-Compiler* is the opportunity to upload the user program to the frequency converter such that the operation is independent of the computer.

The frequency converter features several interfaces, so that CAN-based (Controller Area Network), EIA-485-based (Electronic Industries Alliance), commonly called RS-485, and Ethernet-based fieldbuses can be used to control the converter. In our case, a Modbus connection has been utilized, since an implementation of the control to our LabVIEW-based slow control [Nat18] via a real-time embedded microcontroller is possible. Additionally, since Modbus connections are also used for the slow control of XENON1T, an implementation is simply feasible.

The Modbus protocol is based on the Master-/Slave architecture. For the communication, a TCP<sup>5</sup> connection between a client, the master, and the server called slave is required. Usually the reserved TCP-port 502 is used. The master controls and monitors the whole data transfer.

In order to control the slave (in this case the frequency converter) via LabVIEW interface, Modbus network packets have to be sent from the master (the microcontroller) to the converter. Both packets for monitoring of parameters as well as for controlling parameters are possible. In the following, the structure of these packets will be explained.

Each network packet is composed of a header block and a function code data block (table 3.4).

---

<sup>5</sup>Transmission Control Protocol

Table 3.4.: Modbus protocol structure [Mod06]. Each packet consists of a header and function code data.

Header						Function Code Data		
Transaction Identifier		Protocol Identifier		Length		Unit ID	Function Code	Data
0	1	2	3	4	5	6	7	8...

The header block consists of six bytes, two bytes for the *Transaction Identifier*, two bytes for the *Protocol Identifier* and another two bytes for the *Length*:

- The *Transaction Identifier* identifies associated transactions for the master, such that each request contains a *Transaction Identifier* value, which is copied by the slave to the related response. Usually, a value of 0x00 is allocated.
- The identification of the specific protocol at multiplexing is essential and therefore is provided by the *Protocol Identifier*. For a Modbus connection a value of 0x00 has to be set.
- The *Length* describes the number of bytes following the *Length* bytes. The first byte is called high byte and is set to 0x00. The second byte is referred to as low byte and requires the value 0x0d since the used protocols here feature a length of 10 bytes (0-18). This will be explained later on in more detail.

The header is standard and is identically in each request or response. The process data and parameter exchange of the frequency converter is done by the function code data, which consists of the *Unit-ID*, the specific *Function Code* and the *Data*:

- The *Unit-ID* describes a Subadress. SEW devices use this only for parameter access with the value 0x00.
- The access to the parameter channel is given by *Function Code* (FC). The FC for *read holding registers* FC3 with the value 0x03 as one example allows the user to read data. The code FC16 (value: 0x10) describes the *write multiple registers* and is used to send data. Like that, all essential parameters of the converter can be readout or set to have a maximum control and monitoring of the drive.
- The *Data* block depends on the FC. It is the same for FC3 and FC16. This characteristic data block is explained in the following.

The *Data* block for FC3 and FC16 (table 3.5) is composed of ten bytes including the *Reference Number*, the *Write Word Count*, *Write Byte Count* and the *Process Data*:

Table 3.5.: Data frame structure of the Modbus protocol, which describes the *process data* [Mod06].

Data										
Reference Number		Write Word Count		Write Byte Count	Process Data					
8	9	10	11	12	13	14	15	16	17	18

- The *Reference Number* describes a register number for transferred process data and is composed of two bytes. Since the number of transferred *Process Data* per packet is three, the values for the *Reference Number* are 0x00 and 0x04.
- Bytes 10 and 11, *Write Word Count*, need the number of *Process Data*, therefore 0x00 and 0x03.
- Byte 12, *Write Byte Count* requires the number of bytes for the *Process Data*. Each *Process Data* needs two bytes. Therefore, for three *Process Data* parameters six bytes are needed (value: 0x06).
- The last six bytes are for the *Process Data*. The three *Process Data* parameters can be chosen in the *Parameter tree* of MOVITOOLS beforehand. For the control of the drive, most interesting parameters within the FC16 are the status word, which shows the status of the drive (access, stop and several errors), and the maximum speed. For monitoring using FC3 the actual current and the position of the cylinder can be selected. In such case, only two monitoring parameters can be readout, since the position readout already requires two *Process Data* parameters.

In order to send a complete Modbus data packet for example to start or stop the pump, the related values of the *Process Data* status word has to be found.

At first, Modbus telegrams were recorded during manual up and down movement of the drive with the *Manual mode* (blue) of the SEW software. However, the values could not be identified due to lots of noise within the data packets. Nevertheless, the values have been caught by use of the *Bus monitor* of MOVITOOLS (green), which displays the binary code of these *Process Data* parameters listed in table 3.6.

Table 3.6.: Hexadecimal values for the status word in the modbus data packet.

Status	Value
rapid stop	00x0
controller inhibit	00x1
access	00x6

The values for controlling the speed are just the speed itself in 1/10 revolutions per minute (rpm).

As an example, a complete Modbus data packet which can be sent for reading the default parameters of the drive looks like

00000d0304036000000.

The Modbus data packets have been implemented in the LabVIEW-based slow control and a simple controlling interface has been created visualized in figure 3.24.

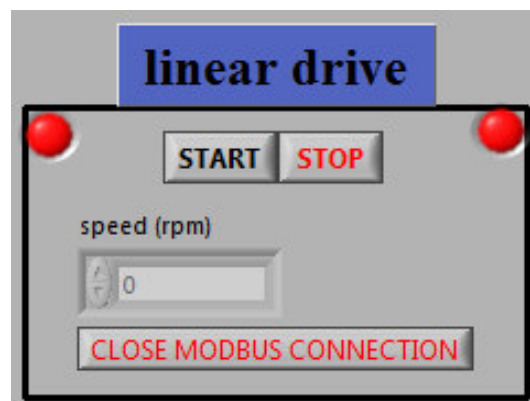


Figure 3.24.: Linear drive control via LabVIEW running on a real-time microcontroller.

Sending as well as receiving of the Modbus protocols is managed via the real-time microcontroller. Consequently, Modbus packets containing the function code FC3 are continuously transferred to the converter to monitor the actual current and the position. The obtained data is saved in data files.

When changing the speed or pushing the stop button on the control panel, the protocol is switched to a Modbus packet containing the function code FC16 that allows controlling of the converter.

After the control sequence finished, the monitoring protocol is re-initialized and data is acquired and saved again.

Like that, the new drive has been successfully implemented to the system. When a user program is uploaded with the *IPOS-compiler* to the frequency converter and an access via compiler is given once, the full control can be done via LabVIEW. Additionally, this Modbus-based monitoring and controlling system can be completely transferred to the GE-based slow control of XENON1T.

The linear movement of the drive results in cyclic gas displacement. The characterization of a thermodynamic model for the compression and expansion of the gas is investigated in the following.

### 3.7. Thermodynamic model

The pump is a compression machine and can be characterized by a thermodynamic cycle with different changes of condition. Assuming an ideal gas and an ideal machine without heat loss to the environment, an adiabatic compression with backward expansion occurs at each single stroke. The operating volume contains inlet as well as outlet, which are self-controlled via flapper valves. The flapper valves presented in detail in section 3.3 open and close at distinct pressure differences of both sides. In the ideal case, exhaust and suction phases at volume change result in a constant pressure. Therefore, between adiabatic compression and adiabatic expansion isobaric volume changes occur (since gas is lost to the circulation system at this point, it is only isobaric-like, but will be called isobaric in the following). Since the valves cannot be assumed being ideal, without inertia and without infinite closing and opening time, opening and closing transition regions are present between adiabatic and isobaric changes of state. As résumé, the resulting thermodynamic cycle for an ideal gas without consideration of heat transfer or leakages to the environment can be explained by the pv diagram in figure 3.25.

The figure shows the pv diagram with regard to the piston movement of the pump. Since the pump features at each endcap outlets as well as inlets, two thermodynamic cycles are running at the same time. In the following, the focus is on the red cycle and thus on the volume left from the piston in this sketch.

The cycle contains eight virtual points (vp) between the several changes of state, valve opening regions and parts of pressure equalization:

- 1 → 2 adiabatic compression:

The maximum gas volume inside the cylinder can be defined as  $V_1$ . Movement of the piston from this point to the left will adiabatically compress the gas up to the pressure  $p_{out}$  at vp 2.

- 2 → 3 outlet valve opening

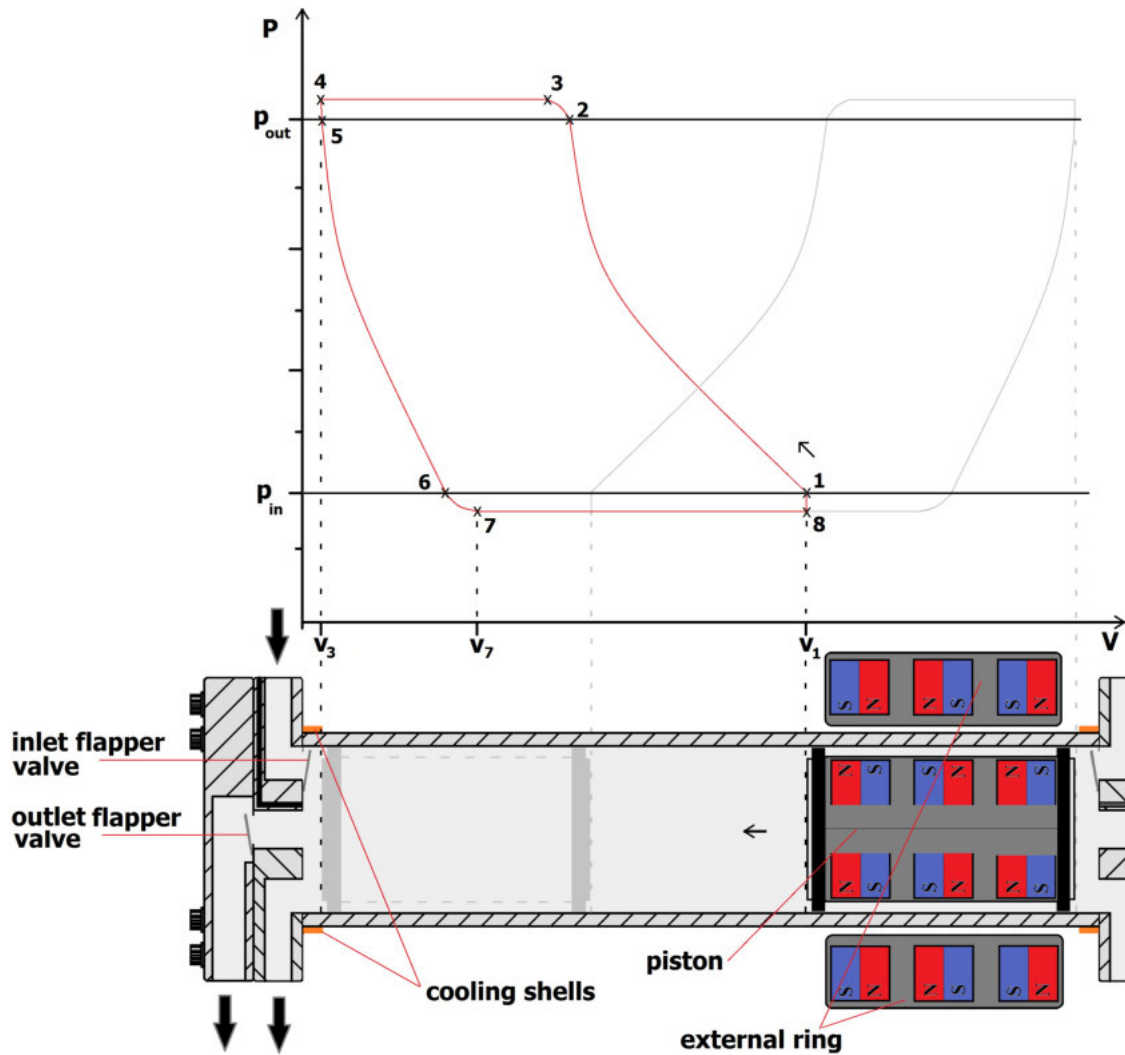


Figure 3.25.: Schematic of the expected pV-diagram the pump and illustration of the related piston movement. The red cycle of the pV-diagram presents the thermodynamic behaviour relating to the volume left from the piston. Accordingly, the light grey cycle is based on the volume right from the piston.

Reaching of  $p_{out}$  results in opening of the outlet flapper valve. Further volume decrease creates further pressure increase due to not instantaneous opening of the valve. At complete opening of the valve,  $v_{p3}$ , as much gas can flow out such that the pressure stays constant.

- $3 \rightarrow 4$  isobaric compression

Discharge combined with further volume decrease results in an isobaric compression up to the dead volume  $V_3$ , which is the smallest available volume due to the cooling shells

and space needed for the flapper valves with its blockers (vp 4).

- 4 → 5 pressure equalization

At the vertex ( $V_3$ ), no more compression results in pressure equalization, since gas can further exhaust up to a pressure  $p_{out}$ . Nonetheless, the inertia of the flappers avoids closing of the valves at vp 5.

- 5 → 6 adiabatic expansion

Afterwards, the movement changes its direction, the outlet valve closes and the piston moves back to the right. An adiabatic expansion follows up to reaching  $p_{in}$  (vp 6).

- 6 → 7 inlet valve opening

Reaching of  $p_{in}$  leads to opening of the inlet flappers. Similar to the process at compression, the finite opening time of the flapper valve leads to further expansion before enough gas can flow in keeping the pressure constant. Therefore, the pressure falls below  $p_{in}$ .

- 7 → 8 isobaric expansion

At the point of maximum valve opening, as much gas can flow in such that the pressure stays constant and the adiabatic expansion follows up to reaching the maximum operation volume  $V_1$ .

- 8 → 1 pressure equalization

As soon as the vertex right from the piston is reached, a pressure equalization occurs such that the pressure increases to  $p_{in}$ . However, the inlet flapper valve will not close due to its inertia.

The movement changes its direction and the cycle can start again.

Next, calculations based on the model for the thermodynamic cycle will be presented. Each change of state requires energy conservation, which is declared in the first law of thermodynamics:

$$\Delta U = \Delta W + \Delta Q. \quad (3.7)$$

A change of the internal energy  $\Delta U$  of a system is the sum of work  $\Delta W$  and added heat  $\Delta Q$ . Work can be defined as a volume change  $dV$  at a pressure  $p$ :

$$\Delta W = -pdV. \quad (3.8)$$

A change in the amount of heat  $Q$  is defined by

$$\Delta Q = mc\Delta T, \quad (3.9)$$

with the mass  $m$  and the specific heat capacity  $c$ . The internal energy is

$$U = N \frac{f}{2} k_B T. \quad (3.10)$$

Where,  $N$  is the number of particles,  $k_B$  the Boltzmann constant and  $T$  the temperature in Kelvin. For monoatomic gases like noble gases, only translation degrees of freedom exist such that the number of effective degrees of freedom is  $f = 3$ .

According to that, heating results in a change of the internal energy such that

$$\Delta U = N \frac{f}{2} k_B \Delta T. \quad (3.11)$$

Both, equation 3.8 and 3.11 can be used to calculate changes of state for the virtual points 1-4.

An adiabatic change of state occurs without heat transfer to the environment ( $\Delta Q = 0$ ). Therefore, equation 3.7 reduces to

$$\Delta U = \Delta W, \quad (3.12)$$

$$N \frac{f}{2} k_B \Delta T = -pdV. \quad (3.13)$$

After a few steps, this applies to the adiabatic equations:

$$TV^{\kappa-1} = \text{const.} \quad pV^{\kappa} = \text{const.} \quad (3.14)$$

The adiabatic equations can be useful to calculate for example the temperature after adiabatic change of state by

$$T_f = T_i \cdot \left( \frac{V_i}{V_f} \right)^{\kappa-1}, \quad (3.15)$$

where  $i$  is the index of the initial state and  $f$  is the index of the final state. With equations 3.11 and 3.12, the change of internal energy and thus work from adiabatic



compression ( $1 \rightarrow 2$ ) and adiabatic expansion ( $5 \rightarrow 6$ ) can be calculated by

$$\Delta U_{if} = \Delta W_{if} = \frac{3}{2} N k_B \cdot \Delta T_{if} \quad (3.16)$$

$$= \frac{3}{2} N k_B T_f \cdot \left(1 - \frac{T_i}{T_f}\right) \quad (3.17)$$

$$= \frac{3}{2} p_f V_f \cdot \left(1 - \frac{T_i}{T_f}\right). \quad (3.18)$$

The specific volume compressed at each single stroke will be theoretically calculated in the following. Due to a full external ring movement range from top to bottom of 305 mm with a piston inside of 155 mm height, the volume

$$V_0 = 180 \text{ mm} \cdot \pi(60 \text{ mm} + 3.5 \text{ mm})^2 = 2280 \text{ cm}^3$$

is compressed at each stroke to the dead volume

$$V_5 = 30 \text{ mm} \cdot \pi(60 \text{ mm} + 3.5 \text{ mm})^2 = 380 \text{ cm}^3.$$

The 3.5 mm added to the radius of the piston result from the piston gaskets. Thus at each single stroke a volume of

$$\Delta V_{13} = V_1 - V_3 = 1900 \text{ cm}^3 \quad (3.19)$$

is compressed. Combined with a typical frequency

$$\nu = 0.6 \text{ Hz} \quad (3.20)$$

of the movement for a double-stroke of our pump, the theoretic specific volume compression per time  $\Delta V_{theor.}$  can be calculated to be

$$\Delta V_{theor.} = \Delta V_{13} \cdot 2\nu = 0.1368 \text{ m}^3/\text{min}. \quad (3.21)$$

However it has to be considered, that this volume compression per time is not the real compression but a stroke volume per time, since only the adiabatic changes of state create real compressions and expansions.

This model can be used to characterize the pump, which is shown in the next chapter.



## 4. Performance and long-term stability

This chapter will primarily show the Muenster pump test station, which is essential for any measurements of the pump. Afterwards, the improved magnetic coupling by the ring upgrade will be presented by a pressure difference measurement. The second part will focus on the thermodynamic characterization by the measurement of the pV-diagram, which is required to interpret the followed heat evolution measurement. Then, a drive profile optimization with the new linear drive will be described for a higher performance. The performance measurements with argon and xenon at several inlet pressures is shown followed by a long-term measurement. In the end of this chapter, the results of a radon emanation measurement are presented proving that the new pump fulfills the low radioactivity requirements of current low background experiments such as XENON1T and EXO as well as future experiments like XENONnT and nEXO. In order to test the pump performance and its long-term capability, the Muenster pump test station (figure 4.1) has been used.

A gas bottle allows filling and recovering the system and a scroll forepump combined with a turbomolecular pump enables to evacuate the system. At evacuation of the system, all hand valves (HV) are open to allow a complete vacuum in the gas system. However, at normal operation of the pump, HV3 and HV4 as well as the bypasses HVb1 and HVb2 are closed.

Additionally, a mass flow controller (FCV, MKS, 1579A) calibrated for xenon can measure a xenon gas flow up to 200 slpm. A Gas Correction Factor (GCF) can be calculated to translate the output signal of the mass flow controller to a corresponding gas flow for a different gas  $x$ . The GFC uses nitrogen as baseline, since usually, mass flow controllers are calibrated with  $N_2$ . Accordingly, the GFC for a gas  $x$  depending on the molecular structure of the gases, the standard density  $\rho$  and the specific heat of the gas  $cp$  can be defined by:

$$GCF_x = \frac{\rho_{N_2} \cdot cp_{N_2} \cdot s}{\rho_x \cdot cp_x}, \quad (4.1)$$

with the molecular structure correction factor  $s = 1.03$  for monoatomic gases,  $s = 1$  for diatomic gases and  $s = 0.941$  for triatomic gases.

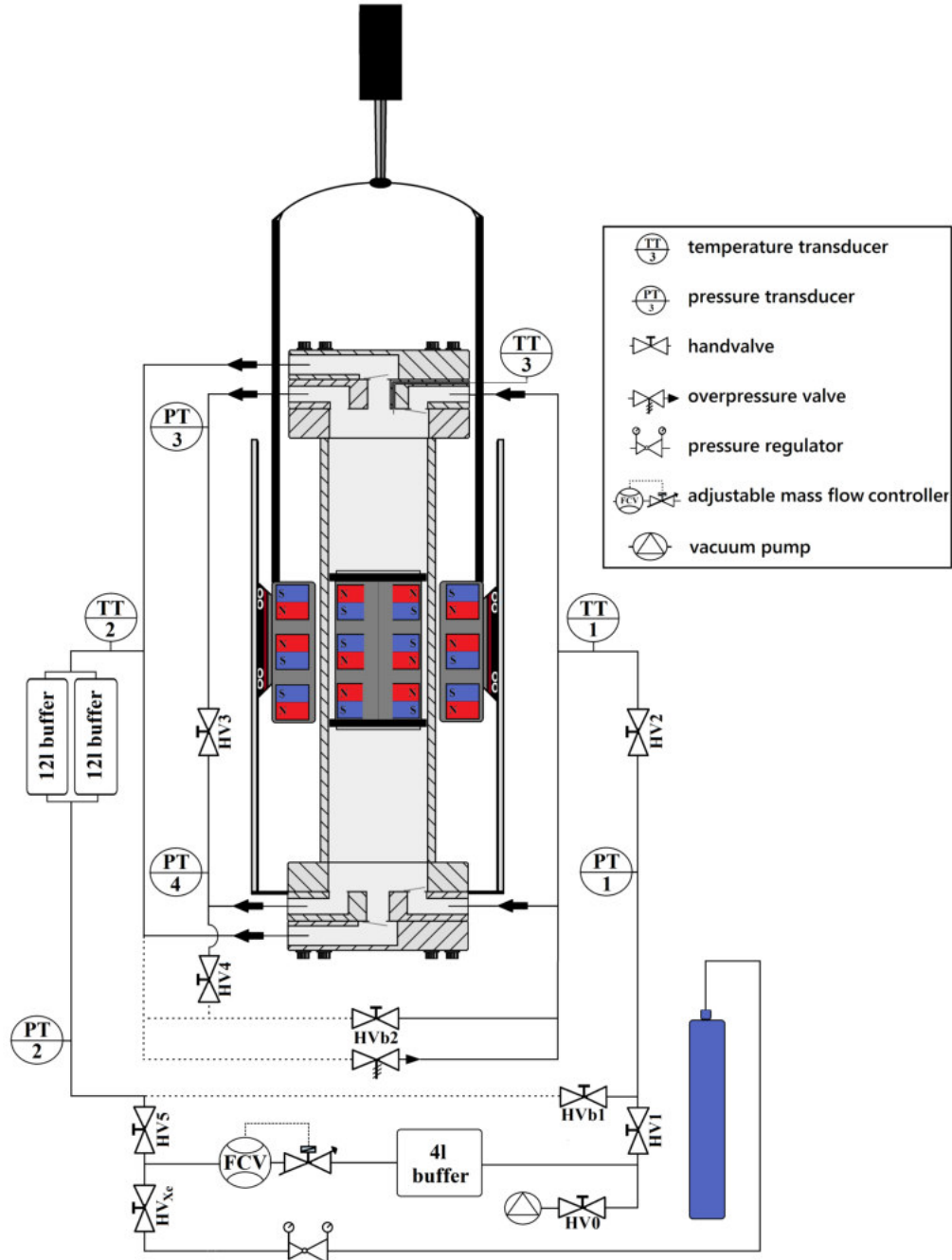


Figure 4.1.: Drawing of the magnetic configuration and the Muenster pump test station.

Formula 4.1 leads for xenon gas to a Gas Correction Factor of  $GFC_{Xe} = 1.32$  and for argon to  $GFC_{Ar} = 1.39$  [MKS]. In order to translate the gas flow of the 200slpm xenon mass flow controller to a gas flow of a different gas, the GFC of the flowing gas has to be divided by the GFC of the calibration gas. Therefore, a 200 slpm flow controller calibrated with xenon will correspond to 211 slpm of argon at full scale.

Two 12l and one 4l buffer volume can reduce flow oscillations due to the characteristic pumping behaviour combined with the small gas system.

Additionally, three temperature transducers (TT, Farnell, HEL-705) are installed to ensure a total monitoring of the heat evolution by friction as well as compression. TT1 measures the inlet temperature of the gas and TT2 the outlet temperature. Outlets and inlets in figure 4.1 are indicated by arrows, which represent the gas flow direction at the top and bottom flange of the pump. TT3 monitors the heat evolution inside the pump at the point of highest compression via a CF16 feedthrough shown in figure 3.11.

Four pressure transducers (PT, Swagelok, PTU) can measure both the compression factor of the pump and the pressure inside the pump body. The inner pressure difference can be utilized measuring and avoiding the point of decoupling of the inner piston from the outer ring.

The compression factor or differential pressure of the pump is defined by  $\Delta P_{pump} = P2 - P1$  and describes the pressure difference between the pressure behind the pump and the pressure before the pump.

The pressure inside the pump called piston pressure is specified by  $\Delta P_{piston} = P4 - P3$ . As mentioned, HV3 and HV4 are normally closed. Thus, the pressure difference between the pressure above the piston (P3) and below the piston (P4) corresponds to the force towards the piston cap area.

Therefore, the piston pressure  $\Delta P_{piston}$  is an essential parameter, since it indicates the limits of the pump performance and allows determining a critical pressure  $\Delta P_{critical}$ . As mentioned in the last chapter, the measured coupling force of  $(3468 \pm 28)$  N corresponds to a piston pressure of about  $(2.74 \pm 0.03)$  bar. But at this measurement, friction is negligible, due to the slow displacement of the piston and the atmospheric environment.

At normal operation of the pump, the friction has to be taken into account. Thus, the critical decoupling piston pressure has to be measured, which will be presented in the following section.

### 4.1. Highest coupling pressure

In order to measure the critical piston pressure  $\Delta P_{critical}$ , which is limited by the coupling of piston and external magnets and thus determines the performance of the pump, the hand valve HV5 of the Muenster pump test station has been closed stepwise during standard operation with xenon gas.

Figure 4.2 presents the measurement of the flow versus pressure difference. Both the differential pressure  $\Delta P_{pump}$  as well as the piston pressure  $\Delta P_{piston}$  are shown.

The more the hand valve is closed, the lower the flow and therefore the higher the pressure difference. At a critical piston pressure  $\Delta P_{critical}$  of  $(2.17 \pm 0.04)$  bar the piston decoupled with a loud noise.

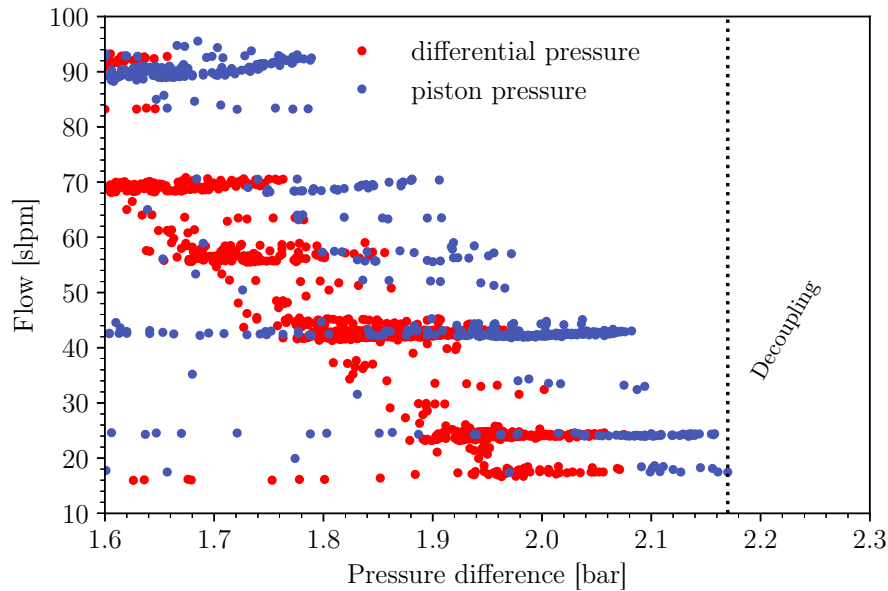


Figure 4.2.: Decoupling of the piston by closing a hand valve within the circulation circuit to increase the pressure difference up to a critical piston pressure  $\Delta P_{critical}$ .

Here, the gaskets are a decisive factor, since the magnitude of friction depends on the diameter and the sticking friction of the material. This measurement has been done with  $(126.80 \pm 0.05)$  mm diameter UHMWPE gaskets. Measurements with  $(126.95 \pm 0.05)$  mm diameter Torlon gaskets gave a decoupling piston pressure  $\Delta P_{critical}$  of  $(1.98 \pm 0.05)$  bar.

According to the measurement of the coupling force in section 3.2, the special configuration of the magnets results in no total decoupling of the piston. The piston will be caught again by the attraction of the other magnet rings. As shown in [Buß16] the displacement of one concentric ring pair results in an unstable equilibrium state. The displacement of two pairs produce a stable potential such that the piston is displaced by two magnetic rings at decoupling.

The piston can be coupled in again by slow moving of the external ring towards an endcap of the pump. Nonetheless, at normal operation, the critical piston pressure  $\Delta P_{critical}$  should not be exceeded to prevent any damages.

In the following, all measurements have been done with the  $(126.80 \pm 0.05)$  mm diameter UHMWPE gaskets and thus with a  $\Delta P_{critical}$  of  $(2.17 \pm 0.04)$  bar. For safety reasons only piston pressures  $\Delta P_{piston}$  below 2.1 bar should be used at normal operation.

As mentioned, the prototype of the pump still uses UHMWPE piston gaskets, which expanded after a few minutes and led to a fixation of the piston and thus a decoupling. Therefore, a thermodynamic characterization is of crucial importance to understand the heat evolution and will be presented in the following.

## 4.2. Thermodynamic characterization

A thermodynamic characterization of the pump may be essential for the understanding of the pump in terms of for example heat evolution as well as behaviour of the flapper valves.

As presented in section 3.7, the operation can be described by a thermodynamic cycle. With the use of the Muenster pump test station (fig. 4.1) a thermodynamic characterization can be done by the measurement of the pV-diagram. For this purpose, PT3 of the pump test station is used to measure the pressure at the top single stroke, and PT4 is used to measure the pressure of the bottom single stroke. The volume can be calculated via the position of the external ring and the radius of the pump body. Accordingly, figure 4.3 presents the pV-diagram of the pump.

The x-axis is related to the volume above the piston, where a volume of  $0 \text{ cm}^3$  is the top flange and thus the inner end of the pump body. The single stroke to the top is shown in blue and the single stroke related to volume below the piston is shown in grey. In the following, the focus is on the top stroke since both cycles seem to be similar.

In comparison to the theoretic expected pV-diagram (section 3.7), the expected isobaric-like changes of state seem to be not constant in pressure. This can be simply explained by the location of the pressure transducers. PT3 measures the pressure in a separated line connected to the top volume with a closed end shown in figure 4.1.

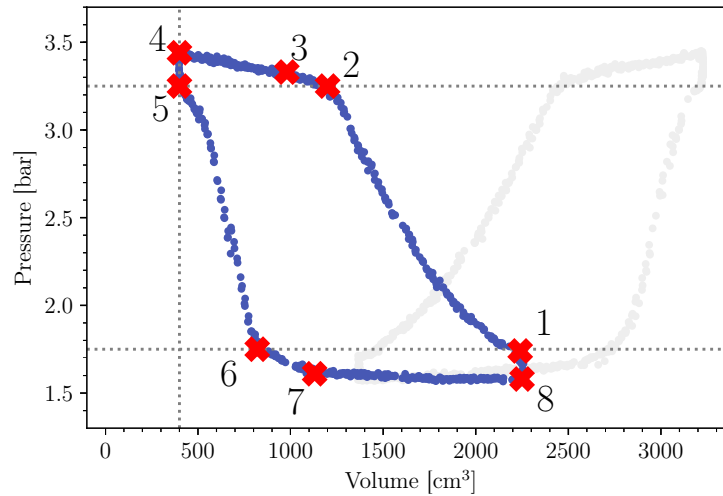


Figure 4.3.: Real pV-diagram of the pump. Both strokes are shown. The volume has to be considered relatively to the starting point at the top of the pump, where the dead volume ends. The virtual points between changes of state, valve opening regions and parts of pressure equalization are marked.

For example, further movement of the piston towards the endcap, will compress gas inside the line of PT3 next to discharge through the flappers. Thus, the measured pressure increases. When the compression stops with the end of the movement, pressure equalization up to the valve opening pressure occurs as expected.

Therefore, the eight virtual points such as in the theoretic pv diagram (fig. 3.25) have been added to the cycle. However, the complete opening of the the outlet flapper valves (vp3) can not be determined due to stetig pressure rise.

For calculations, the exceed of the opening and closing pressures  $p_{in}$  and  $p_{out}$  will be neglected in the following such that only vp 1,2,5 and 6 will be used.

Table 4.1 shows the state parameters for the points obtained from figure 4.3. The dead volume  $V_5$  is larger than calculated in section 3.7, since due to safety reasons the external ring will not move exactly up to the cooling shells. Only an estimation for each state variable is done in the following. Therefore, no errors have been considered.

Table 4.1.: State parameters of the pV-diagram.

Point	Volume $V_i$	Pressure $p_i$
1	2260 cm <sup>3</sup>	1.75 bar
2	1180 cm <sup>3</sup>	3.25 bar
5	400 cm <sup>3</sup>	3.25 bar
6	800 cm <sup>3</sup>	1.75 bar



The parameters of table 4.1 can now be used to calculate the work and heat for each change of state. At first we will calculate the adiabatic heat evolution, since the temperatures are required for the other parameters.

It is assumed that the produced heat increases at each cycle, since warm gas is flown out into the gas system. In the following, this iterative temperature rise will be calculated. Using equation 3.15 the temperature after adiabatic compression at the first single stroke is calculated to be

$$T_2 = T_1 \cdot \left( \frac{V_1}{V_2} \right)^{(\kappa-1)} \quad (4.2)$$

At point (2), the flapper valves open and heated gas is pressed out. The volume is decreased at constant pressure. Thus, we can assume that only the amount of heated gas is decreased without change of the temperature:

$$T_5 = T_2. \quad (4.3)$$

Nonetheless, the amount of gas, which flows out increases the temperature of the gas inside the gas lines. Assuming a total gas volume  $V_{circuit} = 28380 \text{ cm}^3$  of the buffer volumes (28l) and gas lines (length: 2 m, diameter: 1/2"), the temperature increase of the gas inside the circuit can be calculated by the mixing temperature  $T_m$  of the amount of heated gas with  $T_2$  and the amount of gas inside the lines with  $T_1$ :

$$T_m = \frac{p_1 V_{circuit} + p_2 (V_2 - V_5)}{\frac{p_1 V_{circuit}}{T_1} + \frac{p_2 (V_2 - V_5)}{T_2}} \quad (4.4)$$

In the following, an adiabatic expansion of the heated gas results in a volume increase combined with a temperature decrease. The temperature rise can again be calculated by using equation 3.15 to

$$T_6 = T_5 \cdot \left( \frac{V_5}{V_6} \right)^{(\kappa-1)} \quad (4.5)$$

Next, at point (6) the flapper valves open and new gas with the temperature  $T_{m1}$  flows inside the pump body. Here, we assume an infinite mixing time of the gas within the gas system. The following isobaric expansion again will only change the volume of the gas. Therefore, the temperature of the gas at the starting point (1) is a linear composition of the new gas with  $T_{m1}$  and the *old* gas of  $T_6$ . Thus, the temperature  $T'_1$  after one cycle

can be calculated by

$$T'_1 = \frac{p_1 V_6 + p_1 (V_1 - V_6)}{\frac{p_1 V_6}{T_6} + \frac{p_1 (V_1 - V_6)}{T_{m_1}}}. \quad (4.6)$$

Therefore, the thermodynamic model results in warming of the gas at each cycle by the iteration equation

$$T''_1 = \frac{V_1}{\frac{V_6}{T'_1 \cdot \left(\frac{V_1 \cdot V_5}{V_2 \cdot V_6}\right)^{(\kappa-1)}} + \frac{\left(\left(\frac{V_1}{V_2}\right)^\kappa \cdot p_1 V_2 V_{circuit} + p_2 V_1 (V_2 - V_5)\right) \left(\frac{V_2}{V_1}\right)^\kappa \cdot (V_1 - V_6)}{p_1 V_{circuit} + p_2 (V_2 - V_5) \cdot V_2 T'_1}} \quad (4.7)$$

without regarding of heat transfer with the environment and any losses.

After one cycle, the  $T'_1$  applies to

$$T'_1 = 298 \text{ K}, \quad (4.8)$$

where  $T_1 = 298 \text{ K}$  is used, which has been measured with the temperature transducer inside the pump (TT3). Thus, the adiabatic heat is compensated at each cycle and can be neglected.

Based on the calculated temperatures other state parameters such as the adiabatic work can be calculated. With equation 3.18 the work for the adiabatic compression applies to

$$\Delta W_{12} = \frac{3}{2} \cdot p_2 V_2 \left(1 - \frac{T_1}{T_2}\right) \quad (4.9)$$

$$= 203 \text{ J}. \quad (4.10)$$

and for the adiabatic expansion:

$$\Delta W_{56} = \frac{3}{2} \cdot p_6 V_6 \left(1 - \frac{T_5}{T_6}\right) \quad (4.11)$$

$$= -123 \text{ J}. \quad (4.12)$$

Next to the adiabatic component of the heat evolution, the temperature is increased by friction. The heat, which is produced between the contact surface of the piston gaskets and the steel body of the pump at operation, is based on the Peclet number  $L$  [Rae02]:

$$L = \frac{vb \cdot \rho c}{2\lambda}. \quad (4.13)$$

Where  $v$  is the relative speed of the contact surfaces,  $b$  the characteristic length of the

contact surface,  $\rho$  the density,  $c$  the heat capacity and  $\lambda$  the thermal conductivity.

The Peclet number is responsible for the produced temperature field (fig. 4.4). A Peclet number  $< 0.1$  indicates an axially symmetric heating source independent of the movement. A Peclet number  $L > 5$  however describes a process, where the created temperature field is influenced by the movement [Rae02]. Accordingly, a Peclet number  $0.1 \geq L \geq 5$  describes a mixture temperature field.

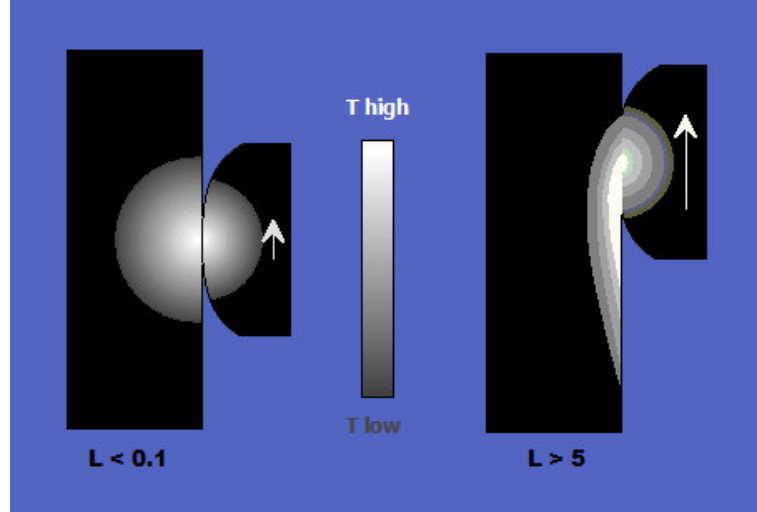


Figure 4.4.: Schematic of frictional heat evolution processes. A slow movement results in a low Peclet number: An axially symmetric temperature field is produced (left). A fast movement leads to a high Peclet number: The created temperature field is dominated by the movement (right). Sketch adapted from [Rae02].

A few assumptions are required to calculate the Peclet numbers for the gasket friction:

- the cycle frequency is between 0.5 Hz and 2 Hz, which results in  $0.15 \text{ m/s} \geq v \geq 0.6 \text{ m/s}$
- the contact surface is assumed to be between 10 % and 25 % of the gasket perimeter.  
Thus  $4 \text{ cm} > b > 10 \text{ cm}$
- UHMWPE:  $\rho = 930 \text{ kg/m}^3$ ,  $c = 1840 \frac{\text{J}}{\text{kg} \cdot \text{K}}$ ,  $\lambda = 0.42 \frac{\text{W}}{\text{K} \cdot \text{m}}$ , [Ker18]
- stainless-steel:  $\rho = 7700 \text{ kg/m}^3$ ,  $c = 460 \frac{\text{J}}{\text{kg} \cdot \text{K}}$ ,  $\lambda = 25 \frac{\text{W}}{\text{K} \cdot \text{m}}$ , [Deu18]

Thus, for stainless-steel as well for UHMWPE, a Peclet number

$$L > 5 \tag{4.14}$$

is calculated. According to [Rae02], the maximum temperature increase by friction to the pump body is given by

$$T_{max} = \frac{2\dot{Q}}{\lambda} \sqrt{\frac{2\lambda b}{\pi \nu \rho c}}. \quad (4.15)$$

The heat flux density  $\dot{Q}$  is related to the area and can be calculated by Fourier's law at each change of state of a cycle. However, only the heat flux density of the adiabatic compression is significant. Depending on the possible cycle frequencies and the chosen specific length  $b$  of the contact surface equation 4.15 applies to temperatures up to 136 °C for the pump body. However, the neglected heat transfer to the environment reduces the maximum heat evolution.

Nevertheless, a cooling system is required managing the friction heat, since as mentioned in the last chapter continuous temperatures higher 70 °C result in demagnetizations of the magnets. Additionally, a stable heat evolution is essential avoiding gasket expansion.

In the following, the measured heat evolution will be presented to prove the heat evolution model as well as to assess the cooling system.

### 4.3. Heat evolution measurement

A three component cooling system has been installed to the Muenster pump test station as presented in detail in 3.5, because the piston gasket expansion resulted in a decoupling of the piston in [Buß16].

Since the prototype magnetic pump has no temperature transducer inside the pump, the heat evolution of the outlet TT2 is used for comparison in the following. The heat evolution during operation with argon at an inlet pressure of  $(1.45 \pm 0.05)$  bar, a flow of  $(103 \pm 4)$  slpm and  $\Delta P_{pump}$  of  $(0.76 \pm 0.05)$  bar is shown in figure 4.5. The frequency was about  $\nu = 1$  Hz, which results with equation 4.15 in a maximum temperature of the pump body of 100 °C without consideration of heat dissipation.

The heat evolution without cooling system (blue) increases up to the point of decoupling, where the operation has been stopped.

In order to extrapolate the evolution, a simple exponential fit function has been found, yielding a convergence temperature of 59.52 °C. This maximum temperature is lower than the maximum expected 136 °C due to heat dissipation by heat transfer to the outside of the pump.

Due to the implementation of the cooling system, the heat within the pump has been drastically lowered and thus uncritical temperatures around 35 °C (red) have been achieved.

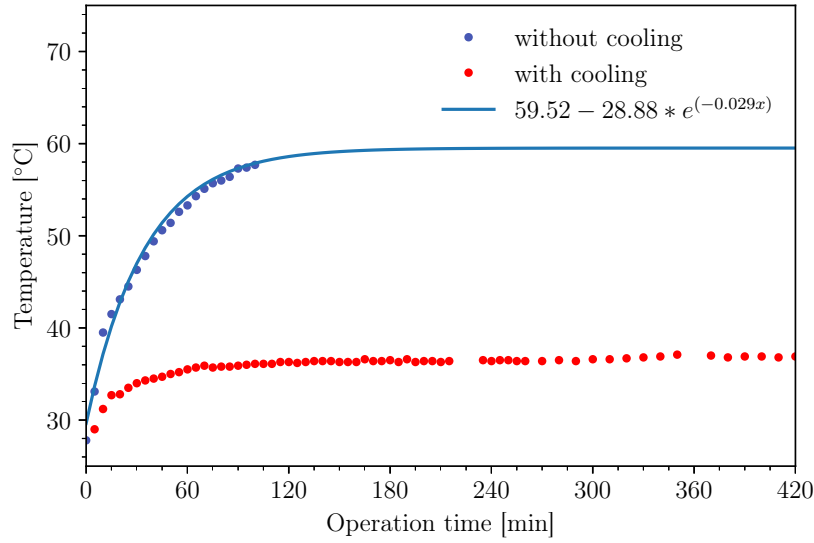


Figure 4.5.: Heat evolution at the outlet of the pump without cooling system (blue) and with cooling system (red) at operation with argon at an inlet pressure of  $(1.45 \pm 0.05)$  bar. A flow of  $(103 \pm 4)$  slpm and a  $\Delta P_{pump}$  of  $(0.76 \pm 0.05)$  bar have been obtained.

In the following, it is assumed that the temperature of the outlet of the pump is in equilibrium with the temperature of the pump body after a distinct operation time. Moreover, the assumption that the heat dissipation is approximately the same at the pump body and the outlet line is used.

The dimensions of the pump body (length: 520 mm, inner diameter: 127 mm, thickness: 4 mm) result in a stainless-steel mass 0.66 kg. According to equation 3.9 the cooling system removes at each cycle an amount of heat of 7444 J, where a specific capacity of 460 J/kgK was used.

At 100 % efficiency, a cooling water flux of four liters per minute are required achieving this, which seems to be realistic. Here the specific capacity of 4190 J/kgK for water [Ruf13] was used.

For a more qualitative investigation a flux meter for the cooling water has to be used

measuring directly the flow of cooling water and temperature transducers measuring the water temperature before and after the pump are required. Additionally, a measurement of a temperature transducer located at the pump body would make more sense.

Since the heat evolution has been managed, a drive profile optimization has been done to further increase the performance, which is described in the next section.

#### 4.4. Drive profile

The gear drive with con-rod and crankshaft was changed to an electrical linear cylinder with an own programming interface as explained in chapter 3.6. This allows for a custom made user program with the IPOS-Compiler. At first a simple user program (A) had to be written resulting in a similar linear movement of the external ring like the movement of the gear drive.

The two stroke pumping mechanism, leads to alternating compression and expansion. The linear drive profile creates a slow increase of the piston pressure  $\Delta P_{piston}$  over the whole path.

An ideal drive profile would hold the maximum operated  $\Delta P_{piston}$  at all time with an infinite small drive path for a sign change at each stroke. Therefore, distinct higher speeds at the beginning and infinite accelerations are required, to prevent a decrease of the piston pressure during expansion and compression of the volumes separated by the piston. Assuming an inlet with a cross section such that a maximum amount of gas can flow in the sign change would be in the middle of the drive path. However, the volume increase at expansion is steeper than inflow of gas. Therefore, the sign change occurs before the mid of the drive path.

Figure 4.6 shows the piston pressure evolution versus position of the external ring for the linear profile and an ideal profile.

At the linear profile (blue) the piston pressure instantaneously decreases at 0 mm and 305 mm, the points of change in direction of the external ring, corresponding to pressure equalization, which was explained in the pv diagram in chapter 3.25. The blue crosses illustrate the following opening of the inlet flapper valves and the blue points indicate the opening of the outlet valves. The whole drive path is required to build-up the piston pressure to the maximum.

The ideal drive profile (black) shows, the maximum piston pressure can be kept constant at expansion from 0 mm: An infinite run-up results in an instantaneous opening of the inlet flapper valve, such that the pressure can be held up to the sign change of the piston pressure, where the volume increase exceeds the gas inflow.

In order to approximate the ideal drive profile, the start-up speed as well as the accel-

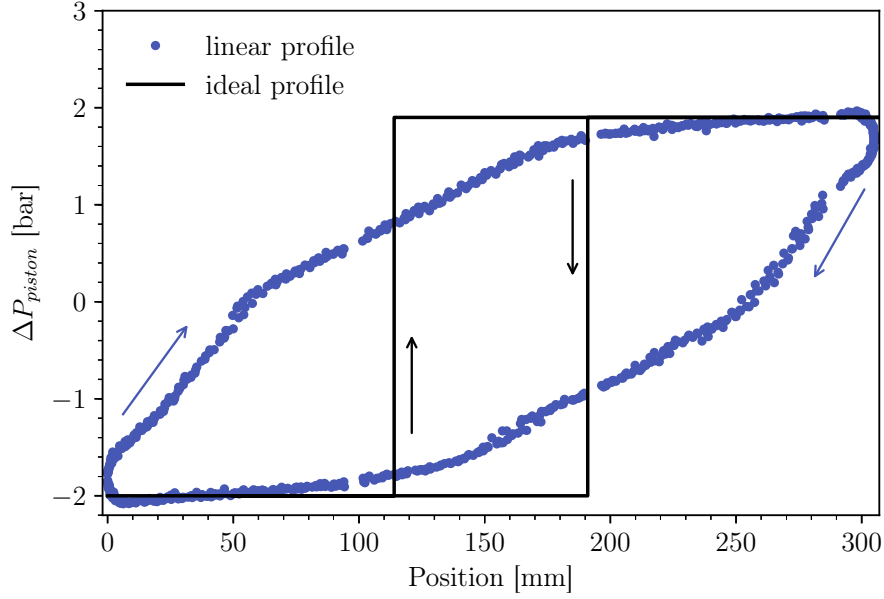


Figure 4.6.: Piston pressure versus position of the external ring referred to both endcaps at operation with xenon at an inlet pressure of  $P_{inlet} = (1.8 \pm 0.1)$  bar. The linear drive profile (blue) is not convenient for an efficient operation because almost the whole drive path is required to build up the piston pressure  $\Delta P_{piston}$  in contrast to an ideal profile (black).

eration to this maximum speed has to be increased. The higher speed and acceleration are, the stronger has to be the stopping to prevent an exceeding of the maximum desired piston pressure  $\Delta P_{piston}$ . In the end, a drive profile with multiple acceleration and deceleration processes has been created, which is presented in figure 4.7.

The speed of such optimized profile versus position of the piston is visualized in red. The linear profile from figure 4.6 is illustrated in blue. This optimized profile depends on the inlet pressure, the gas type and the maximum desired piston pressure  $\Delta P_{piston}$  of the operation. Thus, any variation requires an individual optimized profile.

The plotted piston pressure versus position of the external ring for the optimized profile (fig. 4.8) approximates the form of an ideal profile. The piston pressure slightly decreases at the endcaps. The wavelike fluctuations at the top and bottom evolve from interim slowing of the drive in order to compensate the fast run-up. This avoids the surpassing of the maximum piston pressure und thus decoupling. Finer steps in the profile should damp this oscillation of the piston pressure and would further improve the profile. The slowing after fast run-up at 100 mm conspicuously provides the fast sign change of the piston pressure.

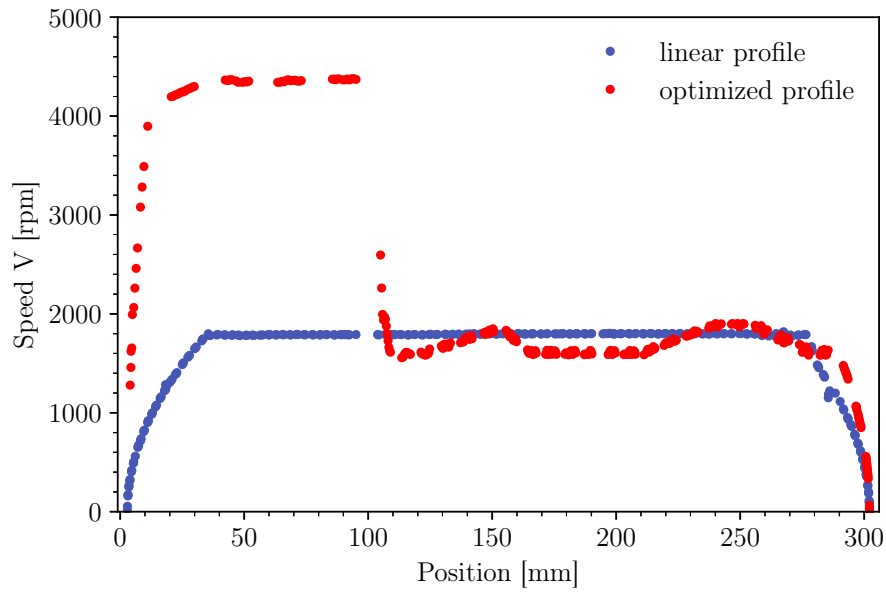


Figure 4.7.: Speed  $V$  of the electric cylinder versus position of the external ring is shown for the linear profile (blue) and for the optimized profile (red) for a single stroke from the top (0 mm) to the bottom (305 mm).

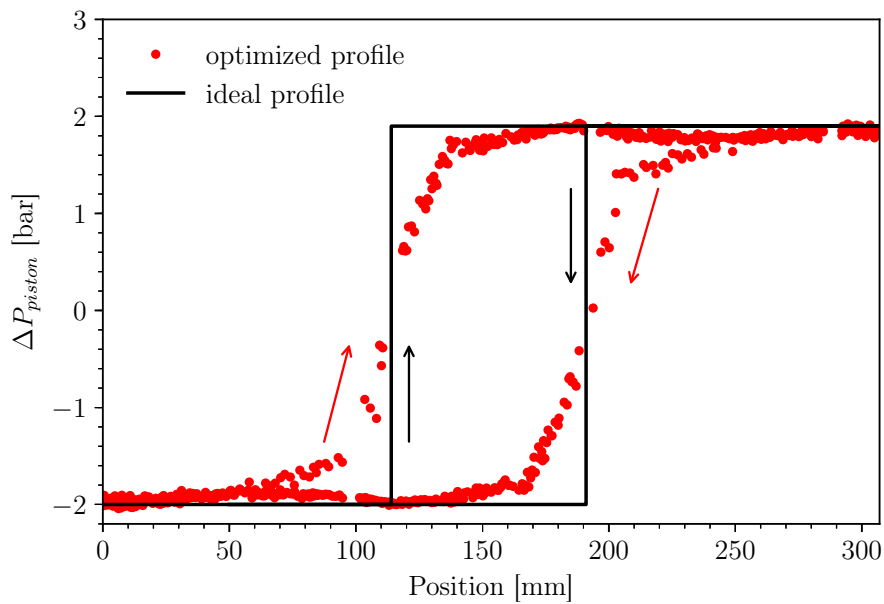


Figure 4.8.: Piston pressure versus position of the external ring for the optimized drive profile at operation with xenon at an inlet pressure of  $P_{inlet} = (1.8 \pm 0.1)$  bar.

The associated performances for the linear profile in contrast to the optimized profile is presented by the obtained flow versus the compression factor  $\Delta P_{pump}$  in figure 4.9.



Additionally, the mean combined with related error bars depending on the standard deviation is shown to indicate the improvement in the form of a smoother flux.

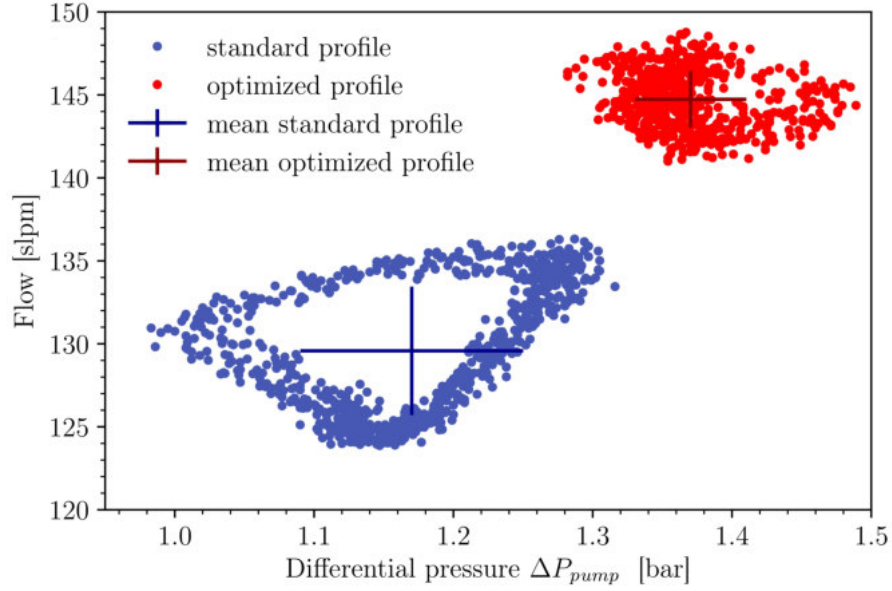


Figure 4.9.: Pump performance for different drive profiles. The optimized profile (red) achieved a flow of  $(144 \pm 2)$  slpm and a  $\Delta P_{pump}$  of  $(1.37 \pm 0.04)$  bar in contrast to the standard profile (blue) with a flow of  $(129 \pm 4)$  slpm and a  $\Delta P_{pump}$  of  $(1.17 \pm 0.08)$  bar.

Figure 4.9 shows that the performance in terms of mean flow and mean differential pressure  $\Delta P_{pump}$  as well as oscillation given by the standard deviation has been optimized. With the linear profile a flow of  $(129 \pm 4)$  slpm with a  $P_{pump}$  of  $(1.17 \pm 0.08)$  bar was reached. In comparison, the optimized profile achieved flows of  $(144 \pm 2)$  slpm and a  $\Delta P_{pump}$  of  $(1.37 \pm 0.04)$  bar.

The optimization of the drive profile results at this configuration of inlet pressure, gas and maximum desired piston pressure in flow improvements of 12 %. Moreover an increase of compression by 17 % at the same piston pressure inside the pump was achieved.

Both are connected with the cycle duration of a double-stroke. The optimized profile with its faster speeds and higher accelerations increases the pumping frequency from  $\nu_{standard} = 36$  double-strokes per minute to  $\nu_{optimized} = 42$  double-strokes per minute at the same maximum piston pressure inside the pump. Therefore, the real specific volume compression per minute  $\Delta V_{real}$  without consideration of losses has to be increased from

$$\Delta V_{standard} = \Delta V_{15} \cdot 2 \cdot \nu_{standard} = 1860 \text{ cm}^3 \cdot 2 \cdot 36/\text{min} = 0.1339 \frac{\text{m}^3}{\text{min}}$$

to

$$\Delta V_{\text{optimized}} = \Delta V_{15} \cdot 2 \cdot \nu_{\text{optimized}} = 1860 \text{ cm}^3 \cdot 2 \cdot 42/\text{min} = 0.1562 \frac{\text{m}^3}{\text{min}},$$

with  $\Delta V_{15}$  calculated via table 4.1. Therefore, the volume compression per minute has been increased by 17 %.

Furthermore, the oscillation of the performance parameters has been reduced by more than 50 %. As mentioned in chapter 1.2, a smooth flux is an essential property for a stable operation with dual-phase TPCs.

In the following, the optimization has been done for different inlet pressures of xenon and argon gas to investigate the potential operation range of the pump.

## 4.5. Performance

The performance was investigated for argon as well as xenon gas for different inlet pressures PT1. For a given inlet pressure, the maximum achievable flow was measured along with the resulting differential pressure  $\Delta P_{\text{pump}}$ . By closing the handvalve HV5 at the outlet stepwise, the resistance of the circulation circuit and thus the differential pressure can be artificially increased. Consequently, the flow is reduced. For each step the drive profile was optimized and the mean and standard deviation for the measured flows and pressures were calculated as presented in figure 4.9. The obtained performance for argon is shown in figure 4.1 for argon where the flow versus differential pressure is visualized. The points corresponding to the same inlet pressure have the same color code and an interpolation line between the data points was drawn.

The figure shows, at an inlet pressure of  $(0.5 \pm 0.1)$  bar (red) the focus on maximum flow results in a flow of 113 slpm with a  $\Delta P_{\text{pump}}$  of 0.75 bar and the focus on maximum  $\Delta P_{\text{pump}}$  leads to a flow of 38 slpm and a  $\Delta P_{\text{pump}}$  of 1.57 bar. The amount of gas in the system and thus the limited power of the drive was insufficient reaching the maximum piston pressure, such that no optimization of the drive profile was used.

At PT1 =  $(1.2 \pm 0.1)$  bar (grey) a maximum flow of 211 slpm was measured, which is the maximum measurable flow of the mass flow controller. Therefore, a maximum flow of 211 slpm was also achieved for higher inlet pressures. However, higher flows are expected without the flow controller limitation.

The maximum  $\Delta P_{\text{pump}}$  was measured at the highest PT1 of  $(2.6 \pm 0.1)$  bar (bright green). Here a  $\Delta P_{\text{pump}}$  of 1.85 bar with a flow of 103 slpm was obtained.

Finally, the amount of gas in the system which is indicated by the inlet pressure PT1 is responsible for the performance: a lower amount of gas results in a lower performance and a higher amount creates a higher performance, which is expected since it is a volume

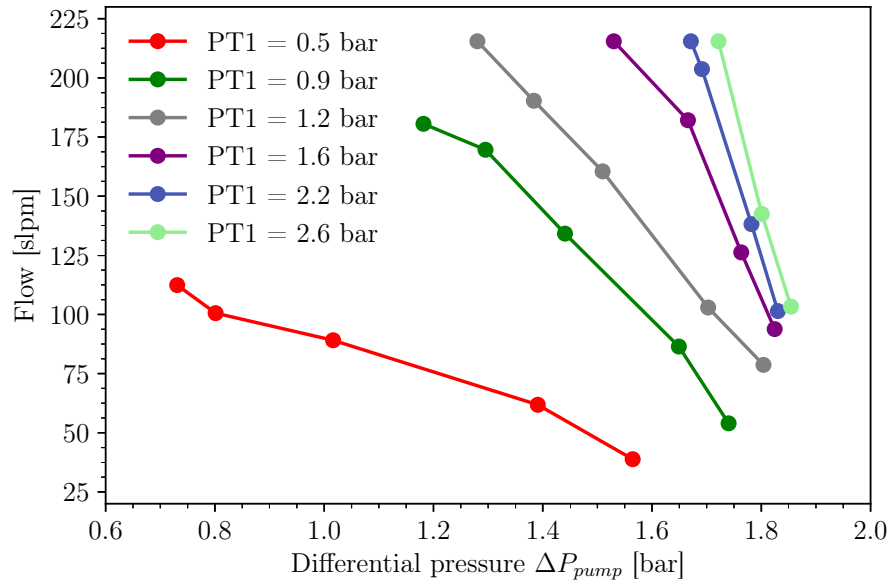


Figure 4.10.: Performance of different inlet pressures of the pump with argon gas.

pump. Additionally, an anti-correlation between flow and  $\Delta P_{pump}$  was observed: a high flow results in a low  $\Delta P_{pump}$  and vice versa. Therefore, emphasis can be placed on high flow as well as on high  $\Delta P_{pump}$  depending on the related application. The same performance tests were done with xenon gas as visualized in figure 4.11.

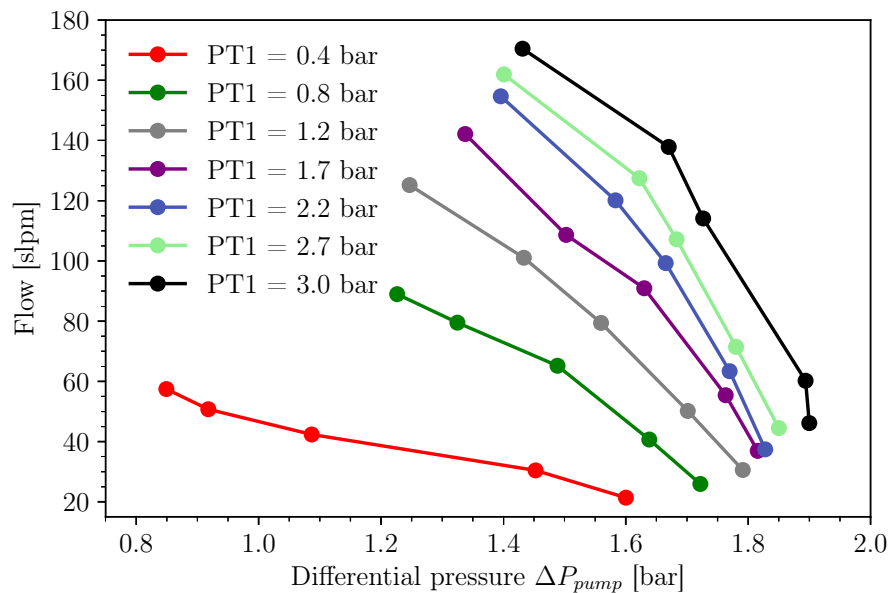


Figure 4.11.: Performance for different inlet pressures of the pump with argon.

At an PT1 of  $(0.4 \pm 0.1)$  bar (red), a maximum flow of 59 slpm combined with a  $\Delta P_{pump}$  of 0.85 slpm was achieved with the emphasis on high flow. In contrast to that, with the main focus on high  $\Delta P_{pump}$  a maximum flow of 23 slpm and  $\Delta P_{pump}$  of 1.60 bar was obtained.

An PT1 of  $(1.2 \pm 0.1)$  bar (grey) results in a maximum flow of 125 slpm and a maximum  $\Delta P_{pump}$  of 1.80 bar.

The maximum performance was reached at the highest inlet pressure PT1 of  $(3.0 \pm 0.1)$  bar (black). Here, a maximum flow of 171 slpm and a maximum  $\Delta P_{pump}$  of 1.90 bar was obtained.

A comparison of both gases shows, the lighter gas argon achieves higher flows. Consequently, even higher flows are expected for lighter gases than argon. Moreover, the maximum  $\Delta P_{pump}$  is approximately the same for both gases, since it is limited by the coupling strength of the piston. Therefore, similar compressions are expected with lighter gases at convenient sealing gaskets and without consideration of limitations by drive speed.

In conclusion, the performance of the pump with xenon gas is sufficient for the usage at the XENON1T experiment. The purification system of XENON1T features an PT1 of 1.4 bar. As illustrated in figure 4.11, the pump obtains at an PT1 of 1.4 bar flows of 100 slpm combined with  $\Delta P_{pump}$  of about 1.5 bar. Therefore the system can be an alternative pump for XENON1T. A possible implementation in the XENON purification system is discussed in chapter 5. With the view on future experiments such as XENONnT, a focus on high flow at the same inlet pressure PT1 results in flows of 135 slpm and  $\Delta P_{pump}$  of 1.3 bar.

Furthermore, most applications such as a TPC require a high performance longterm stability. Therefore, a steady high performance over long term of continuous operation is desired and is presented in the following section.

## 4.6. Long-term stability

In order to use the pump at current experiments introduced in section 1.2, an uninterrupted high performance long-term stability is of crucial importance. This can be indicated by stable performance parameters flow and  $\Delta P_{pump}$  combined with a stable heat evolution inside the pump over weeks.

Figure 4.12 illustrates this long-term stability over a period of 39 days with xenon gas at an inlet pressure of  $(1.5 \pm 0.1)$  bar.

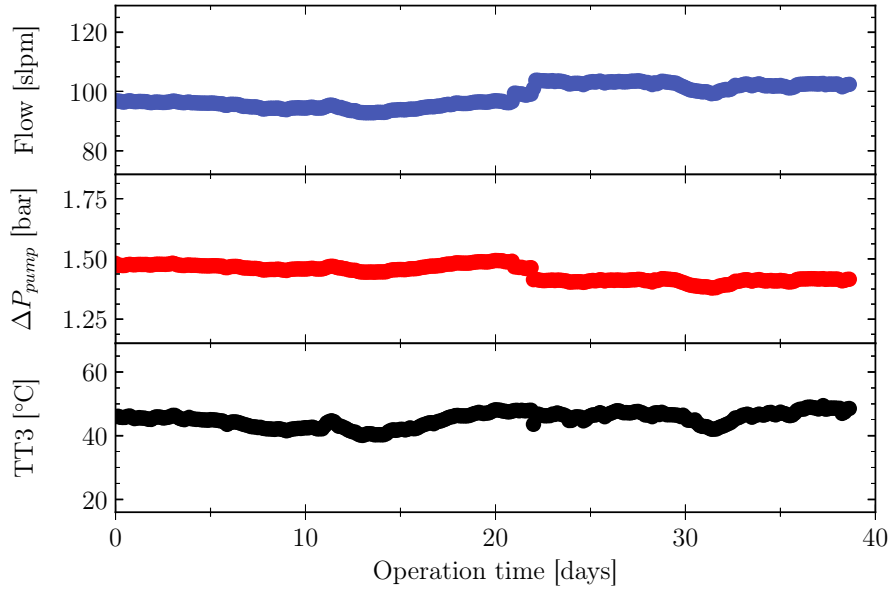


Figure 4.12.: Long-term stability with xenon gas at an inlet pressure of  $(1.5 \pm 0.1)$  bar. A stable operation of the pump with a flow of  $(97 \pm 3)$  slpm,  $\Delta P_{pump}$  of  $(1.47 \pm 0.03)$  bar and a temperature of  $(46 \pm 3)$  °C has been obtained.

A stable flow of  $(97 \pm 3)$  slpm (blue) combined with a  $\Delta P_{pump}$  of  $(1.47 \pm 0.03)$  bar (red) was achieved. After 22 days, the circulation resistance was changed by HV5, which results in an increase of the flow and thus a decrease of  $\Delta P_{pump}$ . The stable mean temperature of  $(46 \pm 3)$  °C is higher than expected. On one side, an acrylic glass housing for safety reasons was mounted, which reduces heat dissipation. On the other side, the fans on the top and bottom flange were removed for this operation to test its long-term effect on the heat evolution. Additionally, the influence of the higher but stable heat evolution on the abrasion of the gaskets can be investigated.

Alltogether, a stable operation was obtained. However, some wear on the rails was observed. Therefore, new rails of harder stainless-steel guides were ordered for future operations. Since this long-term operation is still running, the wear inside the pump was not analyzed.

If the wear, particularly of the gaskets, can be declared being negligible, the pump can be tested at the XENON1T experiment. For this purpose, the extreme purity of the pump thereby has to be ensured.

In order to guarantee the absolute cleanliness in terms of radio-purity of the built-in components for example for low background experiments like XENON1T, a radon emanation measurement has been done in cooperation with MPIK Heidelberg presented in the following.

## 4.7. Radon emanation

Intrinsic background within the xenon such as radon can be a constraining factor on the sensitivity of specified low-background applications.

Therefore, only ultra-clean components were used. In order to measure the total radon emanation originating from the complete pump, the Muenster pump test station was modified as depicted in figure 4.13.

The buffer volumes were removed in order to ensure measuring only the radon emanation of the pump. A setup with a transport trap from MPIK Heidelberg was mounted (fig. 4.14). A carrier gas such as helium is used to transport the radon to the trap. The trap is filled with activated carbon that allows to accumulate the radon by adsorption. Activated carbon features increased pores and thus a larger surface area compared to usual carbons. The key advantage is that the adsorption of the carrier gas, which is created by induced dipole-dipole and higher multipolar interactions, is low in contrast to the strong bonding of the radon on the carbon surface.

Therefore, after evacuating of the pump and then flushing with helium a few times, the pump was filled up to 2 bar with carrier gas helium. In order to measure the radon inside the pump, HV2 and HV<sub>He</sub> are closed. Furthermore, the whole gas system except the pump was evacuated. After circulation of the carrier gas via HVb2 in bypass for a few days with the pump, the radon can be extracted.

For this purpose, the adsorbent has been baked for one hour at 200°C for regeneration. Afterwards, the trap has been cooled with liquid nitrogen, since the adsorption capacity increases at lower temperatures by reason of a lower kinetic energy. After cooling for more than 30 minutes, the helium is pumped slowly with a flux of <100 mbar/min through the

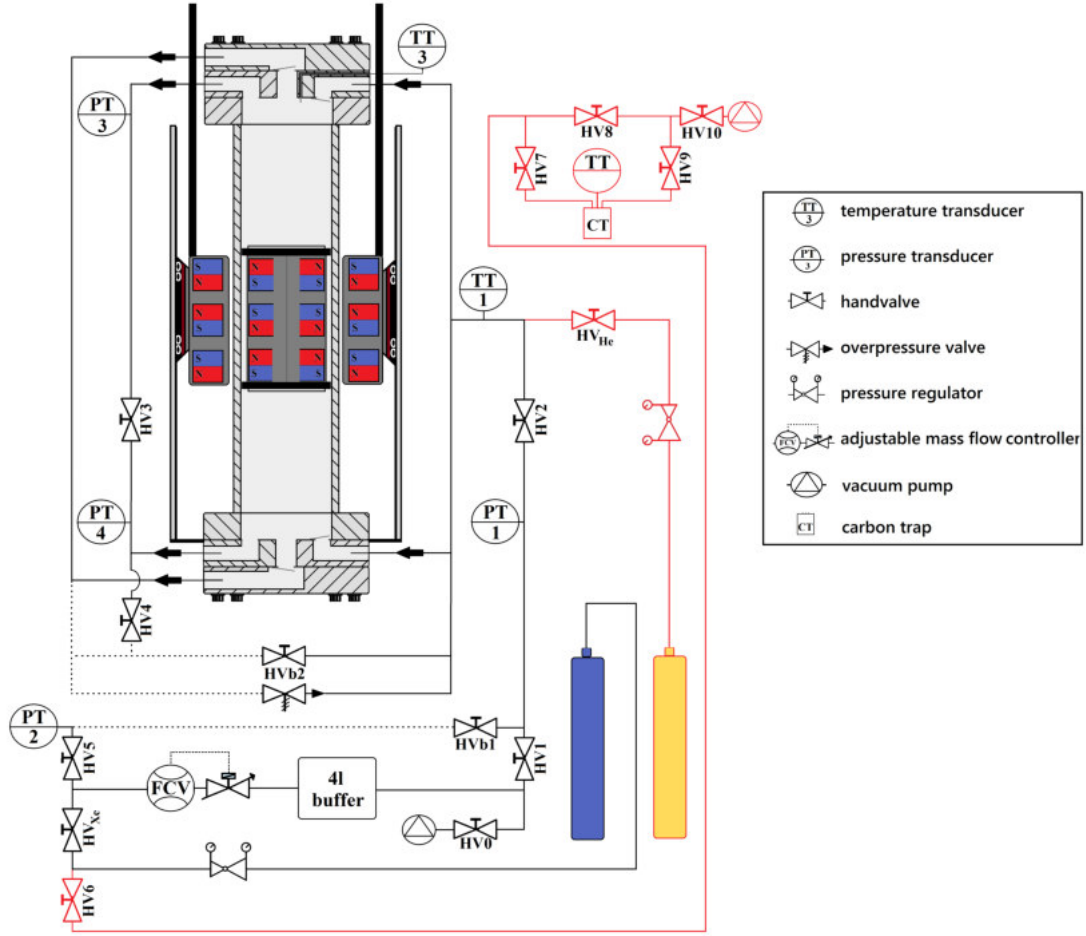


Figure 4.13.: Modified Muenster pump test station for the radon emanation test. The 12l buffer volumes have been removed and new lines (red) have been mounted for a helium bottle and the radon trap.

activated carbon via HV2, HVb1, HV5, HV<sub>Xe</sub>, HV6, HV7, HV9 and HV10. HV8 has to be closed.

Hence, the radon is adsorbed by the carbon. As soon as there is no flux anymore, the valves to the carbon trap have to be closed to ensure no radon accumulation in the cold trap from the vacuum pump and the setup can be removed from the gas system. If the pump can be evacuated up to 10 mbar, 99.5 % of the radon inside the pump has been trapped.

In order to prevent too large radon decay ( $^{222}\text{Rn}$ :  $T_{1/2} = 3.8 \text{ d}$ ), the transport trap has to be sent back to MPIK for the measurement of the radon emanation with counter tubes at the same day.

Two samples were extracted yielding a combined radon activity of  $(330 \pm 60) \mu\text{Bq}$ . The three QDrive pumps feature a radon emanation of 10.9 mBq as explained in section 2.4.

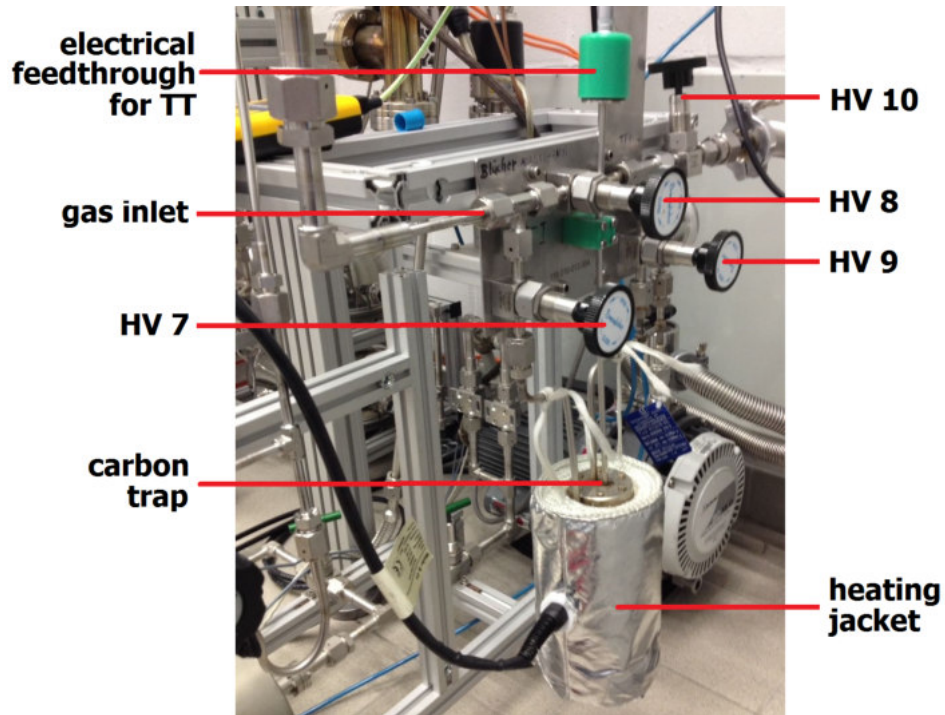


Figure 4.14.: Transport trap from MPIK Heidelberg for the radon measurement of our pump.

Thus, a substitution of all three QDrive pumps by this pump would reduce the total radon budget of XENON1T by 30 %.

The following section shows a possible realization of the integration at the XENON1T experiment.



## 5. Installation at XENON1T

The xenon purification system of the XENON1T experiment is presented in figure 5.1. The system contains a calibration box for radioactive sources and is then divided in two arms, each with QDrive pump presented in chapter 2.2, buffer volume and hot metal getter removing electronegative impurities.

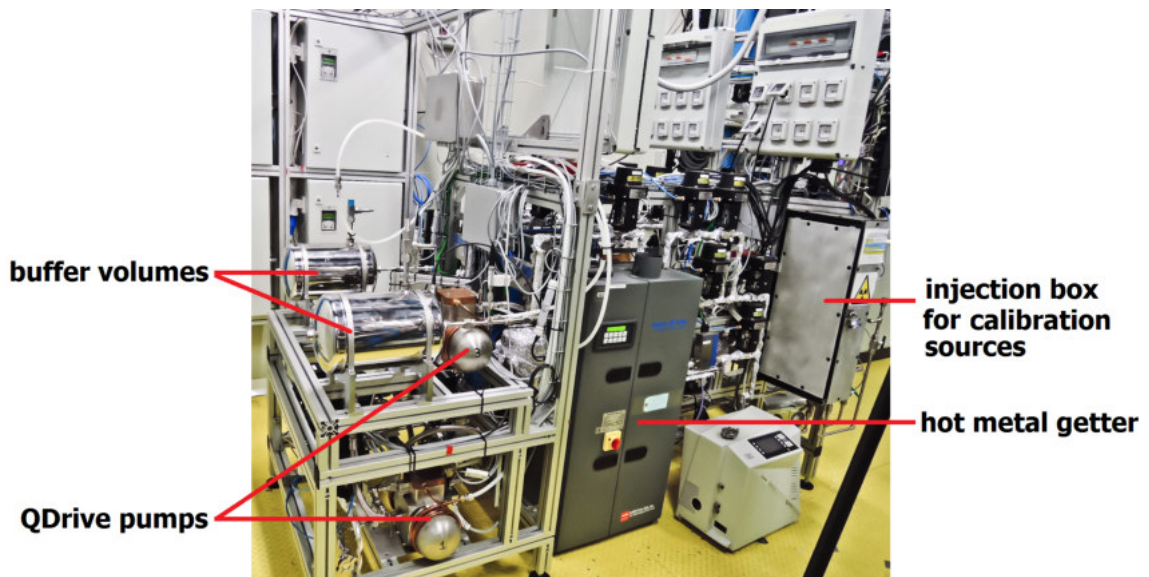


Figure 5.1.: Purification system of the XENON1T experiment [Apr18].

At an inlet pressure of 1.5 bar, a flow of around 50 slpm in total is achieved. One of the arms of the system contains two QDrive pumps in series reducing the stress on the pump. The second arm was also composed of two QDrive pumps. However, one of the pumps has been removed since it is broken. The additional stress on the single pump will be problematically in the foreseeable future.

Therefore, alternative pumps are of crucial importance. The new pump can be utilized for XENON1T. Several options are possible:

- keeping the new pump as spare for further QDrive failures
- installing the new pump as forepump to relieve the QDrives
- replacing of all three QDrive pumps by a few magnetically-coupled piston pumps

Figure 5.2 visualizes the piping and instrumentation diagram of the XENON1T purification system. The implementation as a forepump can be realized before the parallel system of the QDrives (green circle) to relieve all QDrives. Additionally, an implementation of several buffer volumes is essential, since the QDrive pumps require a steady flow at the gas inlet.

The implementation as a forepump could guarantee a reliable future operation of the QDrive pumps, since the load on each pump can be reduced, such that an operation at safer voltages and thus lower temperatures is possible.

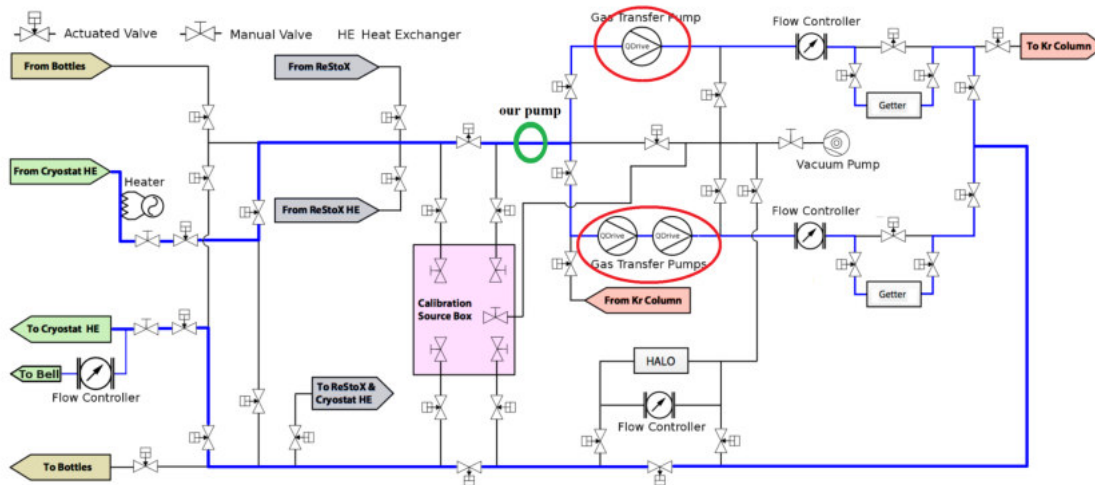


Figure 5.2.: Piping and instrumentation diagram (P&ID) of the XENON1T purification system [Apr17b].

At a first step, the integration as a forepump with the possibility to bypass all pumps makes sense. This way, the load on the remained QDrive pumps will be reduced and the sole operation of the pump can be tested. The implementation can be realized by a Kanya-framework above the QDrive pumps at the purification system (fig. 5.3), since the long foots of the pump can be removed easily.

In a second step, a complete exchange of the QDrives is feasible. Due to a planned upgrade of the purification system from 1/2" to 1" lines, the intrinsic resistance will be reduced. Therefore, one pump can achieve a performance similar to the three QDrive pumps but at higher flows, which increases the electron lifetime due to faster purification. However, higher flows decrease the inlet pressure and therefore, according to the measurements in section 4.5, decrease the performance of the pump.

With the view on future stages such as XENONnT, three magnetically-coupled piston pumps can be implemented: One pump can be mounted again before the parallel system of the QDrives (green circle) as a forepump. Two other pumps can substitute the QDrive pumps (red circles). As mentioned in the last chapter, the dominating background of the

experiment would be reduced by about 30 %.

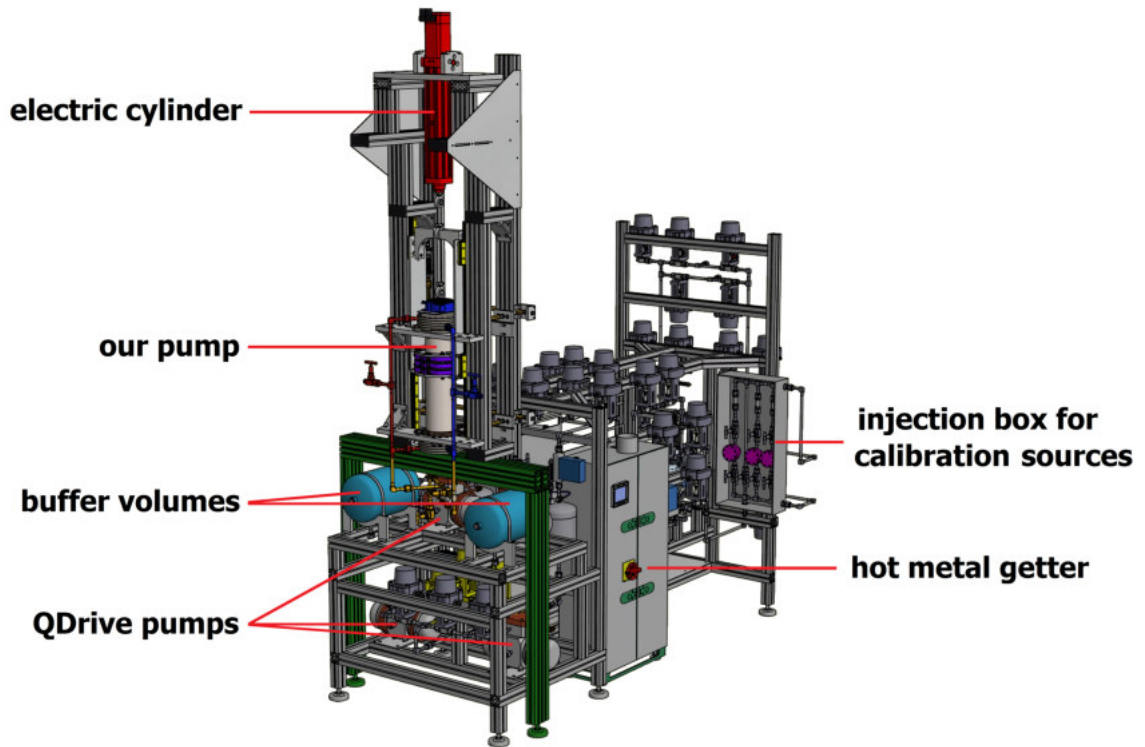


Figure 5.3.: Realization of the integration of our pump to the purification system of the XENON1T experiment. Drawing by C. Huhmann.

In terms of flow control, the implementation to the controlling interface General Electric (GE) seems to be feasible, since as explained in section 3.6 an IPOS-program can be simply uploaded to the frequency converter and the Modbus data packets can be implemented into the GE-software, to start and stop the pump or regulate the speed.



## 6. Conclusion

Experiments with detection targets based on noble gases are a promising technology for a large field of application. Each noble gas hereby has its own amenity.

The unique properties of noble gas targets such as the ionization as well as scintillation process as a response of radiation induced recoils within a convenient detector like a time projection chamber can be used to three-dimensionally reconstruct the position of each event. Furthermore, the sort of the particle scattered with the target material can be determined by the characteristic signals, which will be detected. This way, background discrimination can be achieved. To increase the cross-sectional area and lower the weight of boundary effects of the detector, the detectors become larger. Thus the propagation of light and charges has to be improved to reach required energy resolutions and thresholds. Furthermore, radioactive backgrounds have to be minimized for reaching desired high sensitivities. Next to intrinsic radioactive isotopes of the target material such as  $^{39}\text{Ar}$  and  $^{85}\text{Kr}$ , the radioactive emanation like  $^{222}\text{Rn}$  from detector components play a key role. These aspects increase the demand for purification of the noble gas targets, which usually contain impurities of ppm concentration. The gas displacement through such purification system is provided by pumps also ensuring absolute gas containment and ultra-clean and radio-pure components. With the view on future ton scale and low background experiments, new pumps are required, which feature never achieved specifications such as ultra-cleanliness of built-in components, absolute gas containment and an ultra-high radio-purity combined with a high performance of gas flow as well as gas compression.

Therefore, a magnetically-coupled piston pump for such ultra-clean noble gas applications has been developed. The key feature of this pump is an enhanced magnetic gradient by a special magnet configuration of the piston and the external ring. Distinct higher magnetic field strength has been achieved compared to simpler magnet configuration with same dimensions.

Additionally, a recent upgrade of the external ring magnets from  $10\text{ mm} \times 10\text{ mm} \times 20\text{ mm}$  bar magnets to  $\text{SI}20 \times 10 \times 20\text{ mm}$  results in an increase of the coupling strength by about 40 % to  $(3486 \pm 28)\text{ N}$ . The high coupling strength allows compressing and displacing gas with the pump.

The particular design of the double-stroke pump features a working volume on both sides of the piston. This requires a forcing of the gas flow direction for a positive gas

displacement, which can be realized by flapper valves. An investigation of several flapper valves have not been finalized, however the foundation for further measurements has been laid.

Moreover, suitable piston gaskets are of crucial importance to seal the piston and thus provide a compression as well as to prevent a steel-to-steel contact and force the piston in a central position. The development of a new gasket design reduces the dead volume of the working volume by a larger aluminum frame, which increases the performance. Additionally, the new design will not increase the friction pressure dependent such as the old design, which probably allowed fixation of the piston in [Buß16].

Furthermore, the piston gasket material has to feature next to usual piston gasket requirements such as heat and wear resistance, special requirements due to the demand on absolute cleanliness and radio-purity. The investigation of several advanced polymers could exclude the usage of Torlon and PEEK as piston gasket material. The further usage of UHMWPE requires managing of the heat evolution to reduce gasket expansions such as in [Buß16].

Therefore, a three component cooling system has been developed, which controls the temperature evolution dominated by friction shown in calculations of a thermodynamic model of the operation cycle.

Furthermore, the drive via crankshaft has been exchanged by an electric cylinder drive, which allows the communication with the widely-spread fieldbus Modbus. The drive additionally enables monitoring of several important parameters such as drive position, current, speed etc. and a variation of the drive profile. As presented, the linear drive profile is not suitable for a high performance and results in high oscillations of flow and gas compression. However an optimized profile can improve the performance by up to 17 % and reduces the oscillations by more than 50 %.

This optimization results in a maximum performance with argon gas of 211 slpm limited by the flow controller at a differential pressure  $\Delta P_{pump}$  of 1.72 bar. Artificially increasing the circulation resistance, a maximum  $\Delta P_{pump}$  of 1.85 bar combined with a flow of 103 slpm have been achieved. Both have been reached at the maximum possible inlet pressure of 2.6 bar due to limitation of the pressure regulator of the argon bottle.

With xenon gas, a maximum performance of 171 slpm combined with a  $\Delta P_{pump}$  of 1.43 bar is possible. The increase of the resistance results in a maximum  $\Delta P_{pump}$  of 1.9 bar at a flow of 48 slpm. Both measurements have been done again at the highest possible inlet pressure, here 3.0 bar limited by the pressure regulator of the xenon bottle. Therefore, the performance with xenon gas is sufficient for the usage at the XENON1T experiment

Furthermore, a long-term stability of an uninterrupted operation is of crucial impor-

tance to ensure reliability of such pump before using at an ultra-clean noble gas application. A long-term measurement with xenon gas over 39 days presents a stable performance. With a flow of  $(97 \pm 3)$  slpm and a  $\Delta P_{pump}$  of  $(1.47 \pm 0.03)$  bar, a stable heat evolution of  $(46 \pm 3)$  °C at an inlet pressure of  $(1.5 \pm 0.1)$  bar has been reached.

The magnetically-coupled piston pump therefore guarantees the essential reliability. However, for the usage in a high-purity low background noble gas experiment such as XENON1T, a high radio-purity has to be assured. Thus, in cooperation with the MPIK Heidelberg a  $^{222}\text{Rn}$  emanation of  $(330 \pm 60)$   $\mu\text{Bq}$  has been measured, which is about a factor of ten better than currently used pumps in XENON1T.

Due to a failure of one pump at XENON1T, the integration of our pump to the purification system is still planned for the next month.





## 7. Outlook

Besides, the usage for gas displacement at the purification of noble gases, the pump can also be a great convenience as a compressor for cryogenic systems to save cooling power.

As mentioned before, the radon background is of crucial importance at low background experiments with rare expected events. Particularly, higher sensitivities request for lower background rates. Therefore, radon distillation columns, which reduce the radon percentage emanated from detector components into the target material and thus the radioactive background in noble gases, are a promising technology. The construction of such radon column for the XENONnT experiment is planned in Muenster.

Those noble gas distillation columns (fig.7.1) based on the McCabe-Thiele method make use of the difference in boiling points of the different noble gases. The principle separation method described in chapter 1.1 works since radon is less volatile than xenon. Thus, the radon can be trapped in a liquid xenon reservoir. Whereas, the pure xenon is enriched in the gaseous phase above and can be extracted. This way, a sophisticated system can reduce the radon percentage by a reduction factor  $R > 100$ .

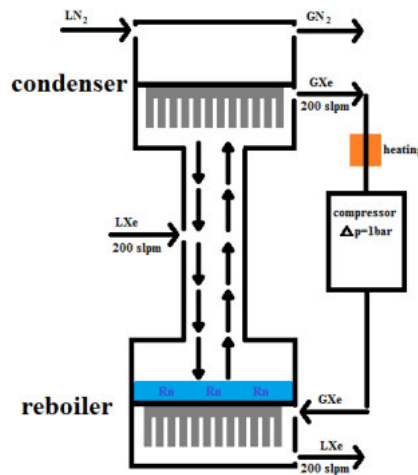


Figure 7.1.: Schematic of a radon distillation column based on McCabe-Thiele with implementation of a radon-free compressor to save cooling power.

For this purpose, two heat exchanger are required. One at the top, the condenser, to liquefy the less volatile radon enriched xenon with nitrogen. And one at the bottom, the

reboiler, which stores the liquid radon enriched xenon. This way, the cooling power of the liquid in the reboiler can be further devoted. Since XENONnT uses a liquid xenon recirculation to achieve high fluxes, the column has to be designed with liquid xenon inlet as well as outlet. Therefore, the pure xenon extracted in the gaseous phase has to be liquefied again. This can be done by making use of the cooling power of the reboiler liquid. Nevertheless, a temperature or pressure gradient between liquid at the top of the reboiler and gaseous xenon at the bottom of the reboiler is essential. Therefore, a heating section as well as a gas compressor can provide this.

The magnetically-coupled pump fulfills all required properties in terms of cleanliness and radio-purity, however a smaller pump is sufficient enough to achieve compressions up to one bar. The thereby created space can be used to operate a four-stroke pump, which would further reduce oscillations of flow and compression.

This can be realized by two identical pumps switched parallel. The double-stroke period has to be  $\frac{\pi}{2}$  shifted to reduce the oscillations to a maximum. Different configurations are possible such as a three magnetic ring pump as the pump presented in this thesis or for example a five ring pump, which features thereby a higher magnetic gradient but increases the length of the pump by about 60 cm for the same compression volume. Furthermore, a compromise has to be found between saving space by smaller radius and achieving a large volume compression per time  $\Delta V \cdot \nu$ :

A smaller radius reduces not only the compressed volume  $\Delta V$  per single-stroke (ss), but also the coupling strength. Nevertheless, a lower coupling strength  $F$  does not necessarily corresponds to a lower maximum pressure  $\Delta P_{piston_{max}}$  towards the piston with the radius  $r$  due to

$$F = \Delta P_{piston_{max}} \cdot A_{piston} = \Delta P_{piston_{max}} \cdot \pi r^2. \quad (7.1)$$

On the other hand  $\Delta P_{piston_{max}}$  limits at same conditions the frequency  $\nu$  of strokes per minute.

However, much higher piston pressures require more care of implementation of high pressure components.

The following table gives an overview of different configurations.

Table 7.1.: Several pump configurations for a new magnetic pump

rings	radius [mm]	coupling strength [N]	$\Delta V$ [cm <sup>3</sup> /ss]	$\Delta P_{piston_{max}}$ [bar]
5	60	6967	1900	5.5
5	50	5545	1400	6.2
5	40	4110	900	6.9
5	30	1881	500	5.3
3	60	3484	1900	2.7
3	50	2952	1400	3.3
3	40	2325	900	3.9
3	30	1408	500	4.0

Where the coupling strength has been simulated by Comsol Multiphysics similar as in chapter 3.2 and the compressed volume without any losses has been calculated analog to 3.19.

The following figure shows the resulting coupling strength versus the piston radius of table 7.1 compared for the different number of rings.

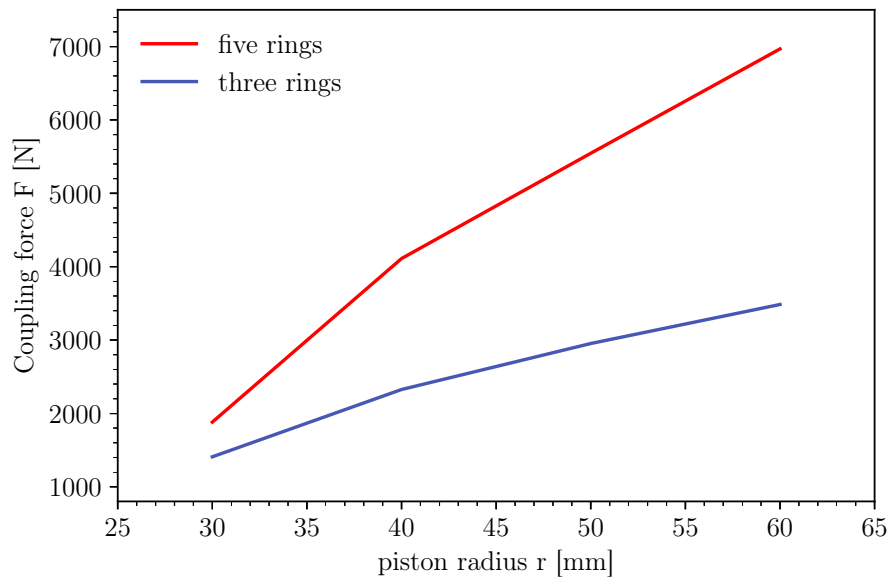


Figure 7.2.: Coupling forces versus radius of the piston for three magnet rings (blue) and five magnet rings (red).

Both, for three magnetic rings as well as for five magnetic rings, the increase of coupling force with the radius is not linear, since the effect of absent magnets for framework shown in figure 3.5 increases with lower radius. This effect can also be seen at the maximum piston pressure  $\Delta P_{piston_{max}}$  presented in figure 7.3

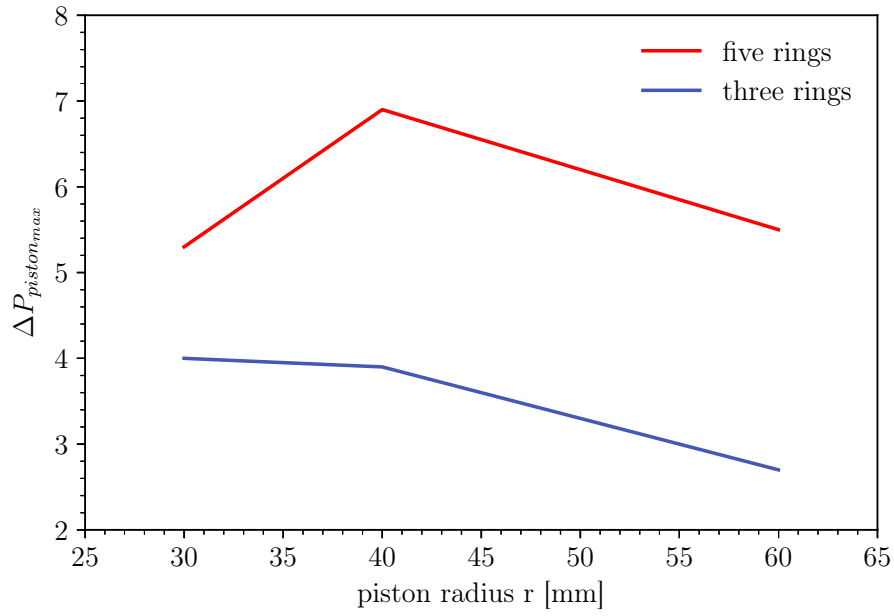
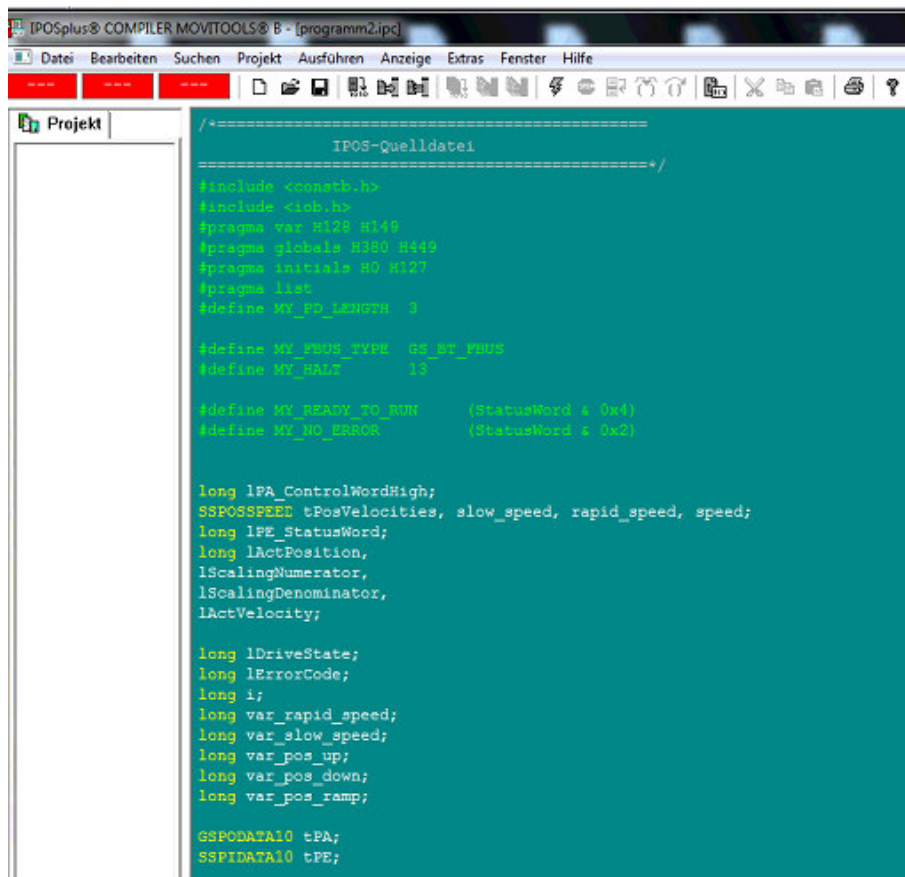


Figure 7.3.: Maximum piston pressure  $\Delta P_{piston_{max}}$  versus radius of the piston for three magnet rings (blue) and five magnet rings (red).

Therefore, using the same external ring design a future pump should not have a piston radius lower than 40 mm.





```

/*=====
IPOS-Quelldatei
=====*/

#include <constb.h>
#include <iob.h>
#pragma var M138 M139
#pragma globale M100 M149
#pragma initials NO M127
#pragma list
#define MY_PD_LENGTH 3
#define MY_PMON_TYPE GE_MY_PMON
#define MY_NALT 13
#define MY_READY_TO_RUN (StatusWord & 0x4)
#define MY_NO_ERROR (StatusWord & 0x2)

long lPA_ControlWordHigh;
SSPOSSPEEE tPosVelocities, slow_speed, rapid_speed, speed;
long lPE_StatusWord;
long lActPosition,
lScalingNumerator,
lScalingDenominator,
lActVelocity;

long lDriveState;
long lErrorCode;
long i;
long var_rapid_speed;
long var_slow_speed;
long var_pos_up;
long var_pos_down;
long var_pos_ramp;

GSPODATA10 tPA;
SSPIDATA10 tPE;

```

Figure A.2.: *IPOS-Compiler-Quelldatei* header: declaration of all variables.

The header consists of attaching header data frames by `#include <constb.h>` and `#include <iob.h>` for access to system functions and the declaration of used variables.

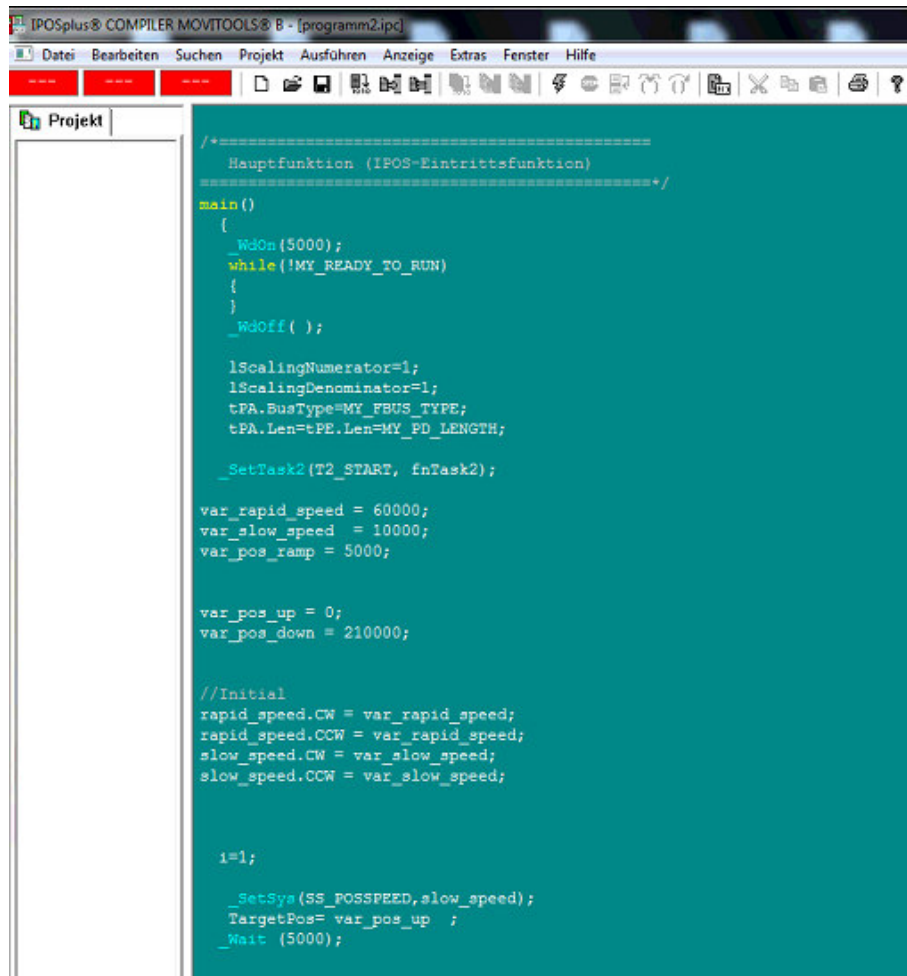


Figure A.3.: IPOS-Compiler - Headfunction: WdOn, Task2, initial, go to start position

The watchdog-counter (WdOn/WdOff) is only for safety reasons. The firmware has 5000 ms for booting. If it has not been booted correctly during this watchdog time, there will be an error.

The `_SetTask2` will call the task2 function (fig. A.5), which debugs the code and shows potential errors. Afterwards, the initialization of the beforehand defined variables such as speeds and positions is following.

The 'go to start position' is done by `_SetSys` function, which transfers the variable, here the `slow_speed`, to an internal system value. The electric cylinder drives up and waits for 5000ms as soon as the cylinder is at the predefined position `var_pos_up` which is position 0 increments.

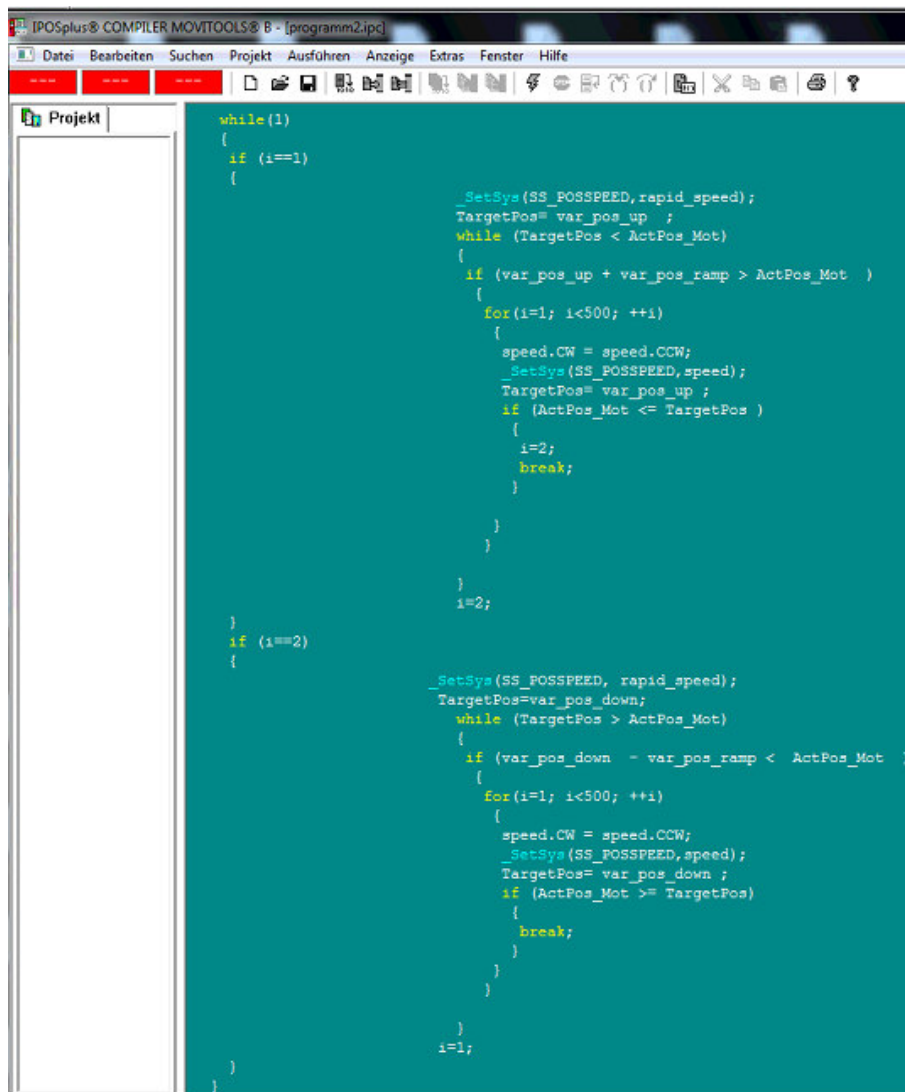


Figure A.4.: IPOS-Compiler - Headfunction: while structure.

The main while structure is continuously executed, while the converter has the enabling signal. Inside, there are two if-cases, if  $i=1$  and if  $i=2$ . The  $i=1$  case is the down-movement of the cylinder, however the  $i=2$  creates the up-moving. Both if-cases have a similar structure. Therefore only the down-movement will be explained in detail:

The predefined speed and target position are transferred. The cylinder will start moving. As long as the target position (here 210000 increments) is greater than the actual position of the cylinder, it will move down. Within this movement, a self-made ramp is executed by the inner if-case and a for-loop. As soon as the target position is reached, there is a break and  $i$  is set to 2.



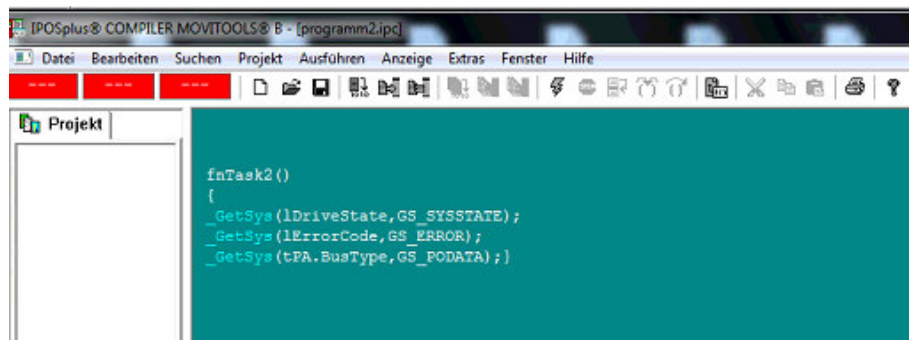


Figure A.5.: IPOS-Compiler - Headfunction: Task2



## **B. Bibliography**

- [Aki17] D. Akimov, et al., 'Purification of Liquid Xenon with the Spark Discharge Technique for Use in Two-Phase Emission Detectors', 2017.  
<https://link.springer.com/article/10.1134%2FS002044121705013X>
- [Alb15] J. Albert, 'Investigation of radioactivity-induced backgrounds in EXO-200', 2015.  
<https://arxiv.org/pdf/1503.06241.pdf>
- [Apr06] E. Aprile, et al., "Noble gas detectors", Wiley VHC, 2006.
- [Apr08] E. Aprile, et al., "Compton Imaging of MeV Gamma-Rays with the Liquid Xenon Gamma-Ray Imaging Telescope (LXeGRIT)", 2008.  
<https://arxiv.org/pdf/0805.0290.pdf>
- [Apr16] E. Aprile, et al., "Physics reach of the XENON1T dark matter experiment", 2016.  
<https://arxiv.org/pdf/1512.07501.pdf>
- [Apr17a] E. Aprile, et al., "First Dark Matter Search Results from the XENON1T Experiment", 2017.  
<https://arxiv.org/abs/1705.06655>
- [Apr17b] E. Aprile, et al., "The XENON1T Dark Matter Experiment", 2017.  
<https://arxiv.org/pdf/1708.07051.pdf>
- [Apr17c] E. Aprile, et al., "Material radioassay and selection for the XENON1T dark matter experiment", 2017.  
<https://arxiv.org/pdf/1705.01828.pdf>
- [Apr18] E. Aprile, "The XENON Dark Matter Search: Status and Prospects", UCLA Dark Matter Conference, 2018.
- [Aug12] M. Auger, et al. "The EXO-200 detector, part I: Detector design and construction", 2012.  
<https://arxiv.org/pdf/1202.2192.pdf>

- [Avi07] F. Avignone, et al., 'Double Beta Decay, Majorana Neutrinos, and Neutrino Mass', 2007.  
<https://arxiv.org/abs/0708.1033>
- [Bak76] G. Bakale, et al., 'Effect of an electric field on electron attachment to SF<sub>6</sub>, N<sub>2</sub>O, and O<sub>2</sub> in liquid argon and xenon', J. Phys. Chem., 23 (1976)
- [Bal05] C. Baldini, et al., 'Absorption of scintillation light in a 100l liquid xenon  $\gamma$ -ray detector and expected detector performance', 2005.  
<https://www.sciencedirect.com/science/article/pii/S0168900205008259?via%3Dihub>
- [Bar93] A. S. Barbarash and V. N. Stekhanov, "Purification and purity control system for  $2\beta$ -decay experiment with liquid Ar ionization chamber", 1993.  
<https://www.nevis.columbia.edu/~ju/Paper/Paper-detector/science18.pdf>
- [Bar12] P. S. Barbeau, et al., "Search for Neutrinoless Double-Beta Decay in  $^{136}\text{Xe}$  with EXO-200", 2012.  
<https://arxiv.org/abs/1205.5608>
- [Bec02] K. Becker, "Basic principles and applications of atmospheric-pressure discharge plasmas", SASP, 2002.  
[http://www.iaea.org/inis/collection/NCLCollectionStore/\\_Public/33/060/33060701.pdf#page=126](http://www.iaea.org/inis/collection/NCLCollectionStore/_Public/33/060/33060701.pdf#page=126)
- [Bol03] A. Bolozdynya, "high pressure helium-3 scintillation position-sensitive detector of thermal neutrons", 2003.  
<https://www.nevis.columbia.edu/~ju/Paper/Alexei/NobleGases/HeScint02.pdf>
- [Bre93] G. Bressi, et al., "Ultra high level liquid argon purification using electron emission from a tip array", 1993.  
<http://www.sciencedirect.com/science/article/pii/016890029391435P>
- [Bre17] S. Breur, "Radon signals in XENON1T", presentation, XeSAT 2017, accessed on 03/2018.  
[https://indico.cern.ch/event/573069/sessions/230077/attachments/1440290/2217054/170404\\_Xesat\\_Radon\\_signals\\_in\\_XENON1T\\_presentation\\_FINAL.pdf](https://indico.cern.ch/event/573069/sessions/230077/attachments/1440290/2217054/170404_Xesat_Radon_signals_in_XENON1T_presentation_FINAL.pdf)

- [Buß13] A. Buß, "Design and test to construct a magnetically driven piston pump for high-purity xenon experiments", 2013.
- [Buß16] A. Buß, "Characterization of the Münster dual phase xenon TPC and of a newly developed magnetically driven piston pump", 2016.
- [Cha12] R. Chandra, "Fast neutron detection with pressurized  $^4\text{He}$  scintillation detectors", 2012.  
<http://iopscience.iop.org/article/10.1088/1748-0221/7/03/C03035/pdf>
- [Che97] V. Chepel, et al., "Performance study of liquid xenon detector for PET", 1997.  
<https://www.sciencedirect.com/science/article/pii/S0168900297001964>
- [Che03] A. Cherubini and A. Bifone, 'Hyperized xenon in biology', Progress in nuclear magnetic resonance spectroscopy, Vol.42, 2003.  
<https://www.sciencedirect.com/science/article/pii/S0079656502000523>
- [Che13] V. Chepel and H. Araújo, 'Liquid noble gas detectors for low energy particle physics', 2013.  
<https://arxiv.org/pdf/1207.2292.pdf>
- [Coa03] K. J. Coakley, et al. "Supernova Observation Via Neutrino-Nucleus Elastic Scattering in the CLEAN Detector", 2003.  
<https://arxiv.org/abs/astro-ph/0302071>
- [Com] Comsol Inc., Comsol Multiphysics.  
<https://www.comsol.com/>
- [CRC03] David R. Lide., "CRC - Handbook of Chemistry and Physics", 84th edition, 2003.
- [Czi91] H. Czichos, 'Hütte - Die Grundlagen der Ingenieurwissenschaften', 29th edition, 1991.
- [Deu18] Deutsche Edelstahlwerke, 'Nichtrostender ferritischer Stahl', accessed on 02/18.  
[https://www.dew-stahl.com/fileadmin/files/dew-stahl.com/documents/Publikationen/Werkstoffdatenblaetter/RSH/1.4016\\_de.pdf](https://www.dew-stahl.com/fileadmin/files/dew-stahl.com/documents/Publikationen/Werkstoffdatenblaetter/RSH/1.4016_de.pdf)
- [Doc08] B. Dockter, 'Rektifikation (Verfahrenstechnik)', 2008.
- [Esp01] W. Espe, et al., 'Getter Materials', accessed on 01/2018.  
<http://www.thevalvepage.com/valvetek/getter/getter.htm>

- [Fro15] M. Frodin, et al., "Sealed operation, and circulation and purification of gas in the HARPO TPC", 2015.  
<https://arxiv.org/pdf/1312.4503.pdf>
- [Geo15] W. Georgi et al., "Einführung in LabVIEW", Hanser Fachbuch's 6th ed., 2015.
- [Gon17] I. González, et al., 'A fluid-structure interaction solver for the fluid flow through reed type valves', IOP Conf. Ser.: Mater. Sci. Eng. 232 012032, 2017.
- [Gra10] W. R. Grace & Co.-Comm., 'SYLOBEAD - Adsorbents for Process Applications', 2010.
- [Iwa12] T. Iwamoto, "Liquid Xenon Gamma-Ray Calorimeter for the MEG Experiment", 2012.  
<http://www.sciencedirect.com/science/article/pii/S1875389212017105?via%3Dihub#!>
- [Ker18] Kern GmbH, "PE-UHMW", 2012.  
[https://www.kern.de/de/technisches-datenblatt/polyethylen-pe-uhmw?n=1401\\_1](https://www.kern.de/de/technisches-datenblatt/polyethylen-pe-uhmw?n=1401_1)
- [Key18] Keywordlister, 'Ethylene Critical Point', accessed on 01/2018.  
[https://www.google.de/search?q=phase+diagram+krypton&source=lnms&tbm=isch&sa=X&ved=0ahUKEwjknJeImP3YAhUPY1AKHTAhA8IQ\\_AUICigB&biw=1366&bih=633#imgrc=BMvJzcQ\\_efJxyM:](https://www.google.de/search?q=phase+diagram+krypton&source=lnms&tbm=isch&sa=X&ved=0ahUKEwjknJeImP3YAhUPY1AKHTAhA8IQ_AUICigB&biw=1366&bih=633#imgrc=BMvJzcQ_efJxyM:)
- [LeP11] LePort, F. et al., "Magnetically-driven piston pump for ultra-clean applications", 2011.  
<https://arxiv.org/abs/1104.5041>
- [Lew08] E. Lewars, "Modeling Marvels: Computational Anticipation of Novel Molecules", Springer, ISBN 978-1-4020-6972-7, 2008.
- [Lie01] K. H. Lieser, "Nuclear and radiochemistry - Fundamentals and Applications", 3rd ed., Wiley VHC, 2001.
- [Lin17a] Linde-group, "Cryogenic air separation - History and technical progress", accessed on 12/2017.  
[https://www.linde-engineering.com/internet.global.lindeengineering.global/en/images/AS.B1EN%201113%20-%20%26AA\\_History\\_.layout19\\_4353.pdf](https://www.linde-engineering.com/internet.global.lindeengineering.global/en/images/AS.B1EN%201113%20-%20%26AA_History_.layout19_4353.pdf)

- [Lin17b] Linde-group, products, accessed on 12/2017.  
[https://www.linde-engineering.com/internet.global.lindeengineering.global/en/images/AS.B1EN%201113%20-%20%26AA\\_History\\_.layout19\\_4353.pdf](https://www.linde-engineering.com/internet.global.lindeengineering.global/en/images/AS.B1EN%201113%20-%20%26AA_History_.layout19_4353.pdf)
- [Mar96] W. Martin and W. Wiese, 'Atomic, Molecular, & Optical Physics Handbook', American Institute of Physics, 1996.
- [Mei08] D.-M. Mei, et al., "A Model of Nuclear Recoil Scintillation Efficiency in Noble Liquids", 2008.  
<https://arxiv.org/pdf/0712.2470.pdf>
- [Mes17] Messer Group, "Gas Purification - For the highest level of purity at point-of-use", accessed on 12/2017.  
<https://www.messergroup.com/documents/20195/57502/Gas+purification>
- [MKS] MKS 1579A, manual
- [Mod06] Modbus Organization, Inc., MODBUS Messaging on TCP/IP Implementation Guide V1.0b, 2006.  
[http://www.modbus.org/docs/Modbus\\_Messaging\\_Implementation\\_Guide\\_V1\\_0b.pdf](http://www.modbus.org/docs/Modbus_Messaging_Implementation_Guide_V1_0b.pdf)
- [Mor09] A. Moraux, et al. "The upgrade of the control system for the CERN/NA62 liquid krypton detector", 2009.  
<http://inspirehep.net/record/809784/files/001%20ICEC%2022%20-%20483.pdf?version=1>
- [Nat18] National Instruments Corporation, LabVIEW System Design Software, 2018.  
<http://www.ni.com/labview/>
- [Neu15] A. Neumeier, 'Optical Properties of Liquid Noble Gas Scintillators', Dissertation, TUM, 2015.  
<https://mediatum.ub.tum.de/doc/1256450/1256450.pdf>
- [Niv15] J. Nivaldo, 'Chemistry - Structure and Properties', 1st edition, 2015.
- [Ost16] I. Ostrovskiy and K O'Sullivan, 'Search for neutrinoless double beta decay', 2016.  
<https://arxiv.org/pdf/1605.00631.pdf>
- [Pay17] R. T. Payne, "The purification of inert gases to high purity", R. D. Mathis Company, accessed on 12/2017.

- [https://www.rdmathis.com/PDF/  
Purification-of-Inert-Gases-To-High-Purity-watermark.pdf](https://www.rdmathis.com/PDF/Purification-of-Inert-Gases-To-High-Purity-watermark.pdf)
- [Pok93] S. G. Pokachalov, et al., "Spark discharge method of liquid rare-gas purification", 1993.  
<http://www.sciencedirect.com/science/article/pii/016890029391435P>
- [PoK18] Polytron Kunststofftechnik, several product data sheets, 2018, accessed on 01/2018.  
<http://www.polytron-gmbh.de>
- [PTI11] Poly-Tech Industrial Inc., several product data sheets, 2011, accessed on 01/2018.  
<http://www.polytechindustrial.com/products>
- [Rie15] K. Rielage, et al. "Update on the MiniCLEAN Dark Matter Experiment", 2015.  
[https://www.sciencedirect.com/science/article/pii/S1875389214006373?  
via%3Dihub](https://www.sciencedirect.com/science/article/pii/S1875389214006373?via%3Dihub)
- [Rae02] H. Raedt, 'Berechnung der Temperaturerhöhung durch Reibung ', RTWH Aachen, 2002.  
[http://darwin.bth.rwth-aachen.de/opus/volltexte/2002/341/pdf/html/  
node56.html](http://darwin.bth.rwth-aachen.de/opus/volltexte/2002/341/pdf/html/node56.html)
- [Ros16] S. Rosendahl, 'Gas purification of the XENON dark matter search', Dissertation, 2016.
- [Ruf13] P. Rufe, 'Fundamentals of manufacturing', 3rd ed., 2013.
- [Sch15] H. Schön, 'Handbook of Purified Gases', Springer-Verlag, 2015.
- [SEW04] SEW Eurodrive, "IPOSplus - Positioning and Sequence Control", 2004, accessed on 10/2017.  
<https://download.sew-eurodrive.com/download/pdf/11320419.pdf>
- [SEW09] SEW Eurodrive, "Operation Instructions - Servo Technology, CMS50/63/71 Electric Cylinder", 2009, accessed on 12/2017.  
<https://download.sew-eurodrive.com/download/pdf/16621212.pdf>
- [SEW18] SEW-Eurodrive, MOVITOOLS MotionStudio engineering software 2018, accessed on 01/2018.  
[https:  
//www.sew-eurodrive.de/products/operation\\_and\\_startup/software/  
engineering\\_software\\_movitools/engineering\\_software\\_movitools.html](https://www.sew-eurodrive.de/products/operation_and_startup/software/engineering_software_movitools/engineering_software_movitools.html)



- [SEW18] SEW-Eurodrive, IPOSplus - positioning and sequence control 2009, accessed on 01/2018.  
<https://download.sew-eurodrive.com/download/pdf/11645415.pdf>
- [She02] H. Sheu and Y. Hu, 'Nonlinear Vibration Analysis of Reed Valves', 2002.
- [Sma12] L. Smart and E. Moore., 'Solid State Chemistry: An Introduction', 4th edition, 2012.
- [Sol14] Solvay, Torlon Design Guide, 2014 accessed on 11/2017.  
[https://www.professionalplastics.com/professionalplastics/content/downloads/Solvay\\_Torlon\\_Design\\_Guide.pdf](https://www.professionalplastics.com/professionalplastics/content/downloads/Solvay_Torlon_Design_Guide.pdf)
- [Sol17] Solvay, products/Torlon 2017, accessed on 12/2017.  
<https://www.solvay.com/en/markets-and-products/featured-products/torlon.html>
- [Tou75] D. Toung, 'Phase diagrams of the elements', Lawrence Livermore Laboratory, University of Columbia 1975.  
[http://www.iaea.org/inis/collection/NCLCollectionStore/\\_Public/07/255/7255152.pdf](http://www.iaea.org/inis/collection/NCLCollectionStore/_Public/07/255/7255152.pdf)
- [Wil16] D. R. Williams, "Earth Fact Sheet" NASA, 2016.  
<https://nssdc.gsfc.nasa.gov/planetary/factsheet/earthfact.html>
- [XEN18] <http://www.xenon1t.org/>
- [Xin08] X. Yajing, "Electronic recoil measurement by ionization in LXe for  $3\gamma$  imaging", 2017.  
[https://indico.cern.ch/event/573069/sessions/230076/attachments/1440288/2217052/Direct\\_Electronic\\_Recoil\\_Measurement\\_Xing.pdf](https://indico.cern.ch/event/573069/sessions/230076/attachments/1440288/2217052/Direct_Electronic_Recoil_Measurement_Xing.pdf)



---

## Danksagung

An dieser Stelle möchte ich mich mal bei allen bedanken, die mich durch diese Zeit meines Lebens geleitet haben.

Zu aller erst einmal bedanke ich mich herzlichst bei Prof. C. Weinheimer, der mir die Möglichkeit gab mich an so einem spannenden Projekt weiterzuentwickeln. Das entgegengebrachte Vertrauen sowie die vorantreibenden Tipps zum richtigen Zeitpunkt halfen mir sehr.

Desweiteren gilt mein Dank Prof. A. Khoukaz für die Bereitschaft die Zweitkorrektur der Arbeit zu übernehmen.

Ein ganz besonderer Dank geht an Michael für die riesen Unterstützung von Anfang an. Ob bei Arbeiten im Labor, beim Schreiben des Papers oder beim zusammenschreiben der Arbeit. Du hast mir immer wenn ich Hilfe brauchte selbstlos zur Seite gestanden. Großen Dank.

Auch Axel möchte ich für seine super Vorarbeit zur Pumpe danken und dafür, dass er mir bei jeglichen Fragen zur Pumpe zu Verfügung stand.

Zudem möchte ich mich bei der gesamten Gruppe bedanken. Vor allem Alex, Christian, Lutz und Miguel, die für eine entspannte Atmosphäre im Büro sorgten.

Weiterhin bedanke ich mich bei unserem Ingenieur Christian. Von der Bachelorzeit an, durch die SHK-Zeit bis hin zum Master konnte man immer auf deine Hilfe im Labor zählen. Ich habe sehr viel von dir gelernt.

Auch unseren Werkstätten möchte ich danken. Die Feinmechanische Werkstatt, denen ich mit ständig neuen Flappern und Gaskets keine Ruhe gelassen habe. Und der Elektronik Werkstatt, allen voran Roland, der mir vor allem mit dem neuen Umrichter eine super Hilfe war. Aber auch besonders Wladimir möchte ich danken, da er bei Fragen und Problemen immer geholfen hat.

Der Schaf-Crew möchte ich an dieser Stelle auch meinen Dank aussprechen. Die super Atmosphäre im Team hat mich den ein oder anderen Abend ablenken und verschlafen lassen, um mich daraufhin mit mehr Konzentration wieder auf das Studium zu fokussieren.

Abschließend möchte ich noch besonders Anna dafür danken, dass sie sich "mit den ganzen Zahlen und Formeln und Chemikalien" auseinander gesetzt hat und mein Englisch aus dem Grundschulniveau herauspoliert hat.

Zuletzt gebührt der größte Dank dir Karla. Ohne dich wäre das alles nicht möglich gewesen. Du hältst mich auch in schwierigsten Phasen aus, stehst hinter mir und bist immer für mich da.

---

